CONSERVATIVE AND DISSIPATIVE FORCE MEASUREMENT TO ENGINEER STEALTH DRUG DELIVERY PARTICLES

by
Julia Caroline Swavola

A dissertation submitted to the Johns Hopkins University in conformity with the requirements for the degree of Doctor of Philosophy

Johns Hopkins University
Baltimore, MD
September 2014

ABSTRACT

Measurement of Conservative and Dissipative Forces to Engineer Stealth Pulmonary Drug Delivery Particles
September 2014

Julia Caroline Swavola, B.S., James Madison University

Academic Advisor: Dr. Michael A. Bevan

Conservative and dissipative forces between drug delivery particles and mucus play a pivotal role in effective pulmonary drug delivery. Improved understanding of forces between DDPs and mucus is essential to engineering particles that efficiently penetrate the tenacious mucosal barrier. In this dissertation, specific thermodynamic and hydrodynamic interactions between differently coated DDPs and mucus were directly measured, creating a platform for engineering virus-mimicking stealth particles capable of efficient pulmonary drug delivery.

Total Internal Reflection Microscopy combined with Bayesian inference analysis was used to directly measure specific and nonspecific interactions between DDP polymer brush coatings and mucin polymer brushes on the energetic *kT*-scale. Considering that viruses with coexisting positive and negative charges in their outer coating rapidly penetrate the pulmonary mucosal barrier, particles were physiadsorbed with polymer brushes that mimicked these viral coatings. PEO copolymer physiadsorbed to DDPs formed an uncharged, chemically inert and sterically stabilizing polymer coating. Polyelectrolytes in mono- or multi-layers and bovine serum albumin formed charged drug delivery particle coatings. Novel analytical theory was developed to characterize the conformation of the layers and define the steric interactions between polymer brushes. Methodical analysis of interactions between symmetric and asymmetric brush layers facilited identification of nonspecific and specific interactions and relative interaction strength. Protein layers with small size-scale charge separation were determined to have the greatest potential as mucoso-penetrating drug delivery particles.

TIRM experiments identified physiadsorbed PEO copolymer and BSA as having significant potential as mucoso-penetrating drug delivery particles. Confocal fluorescence microscopy was then used to measure diffusion through mucus of DDPs baring these coatings. Gradient diffusion, long time self diffusion, and diffusion into a mucus suspension were studied for each of these particle coatings in order to differentiate between specific and nonspecific hydrodynamic interactions. A constant pressure microfluidic system injecting solutions into a Y-junction microfluidic device combined with a novel analytical technique facilitated diffusion characterization with unprecedented accuracy and precision. Experimental data was fit to data generated *via* Comsol computational platform and to theoretical solutions with exceptional correlation. DDPs physiadsorbed with polyethylene glycol diffused rapidly through mucin suspensions. ConA and BSA protein bound to mucins *via* electrostatic and hydrophobic interactions, respectively. These results provide new insight into hydrodynamic interactions as they affect diffusion of virus-mimicking drug delivery particles through mucus. This dissertation combines thermodynamic and hydrodynamic measurements to develope a detailed understanding of forces dictating mucosal penetration of pulmonary drug delivery particles.

Committee: Prof. Michael A. Bevan (Academic Advisor)
Prof. Joelle Frechette (Chemical and Biomolecular Engineering)
Prof. Honggang Cui (Chemical and Biomolecular Engineering)
Prof. Robert Leheny (Physics and Astronomy)
Prof. Margarita Herrera (Material Science and Engineering)

ACKNOWLEDGEMENTS

I would like to thank my family for supporting me throughout my education. My parents have always encouraged me and driven me to excel. Their support and encouragement have been invaluable. My father is my constant cheerleader, my biggest fan and always available with a joke or a fun activity when I take life too seriously. My mother has always encouraged me and kept me focused on my goals. I was able to succeed in graduate school through her encouragement and words of wisdom. I am so fortunate to have these two strong personalities to guide and shape me. My older brother, Michael, motivates and challenges me. His success along with his warmth and excitement for life has inspired throughout my childhood and adult life. My younger sister, Charlotte, is my confidant and my dearest friend, best co-worker, and roommate. Her warm and caring heart keeps me emotionally centered and carries me through tough times. My best friend, Katie, is the sixth member of my amazing family. Katie is a constant source of support, strength and encouragement. Since childhood, Katie has seen more in me than I saw in myself. Her life is never too tough to help me through hard times or to help me enjoy wonderful times. I'd also like to thank my cat for eating dinner any time between 5PM and 3AM. I know she only poops on the floor and claws everything I own because she wants attention.

I would like to share my appreciation for the most amazing group of friends giving their constant support. My friends are positive and never begrudge my lack of free time or my cancelling plans to spend late nights in the lab. I am grateful for the people who I have met in my program. My INBT Cohort has given me great encouragement in

my research and in navigating graduate student life. My labmates have made my work entertaining. The rest of my friends have been an invaluable source of positivity.

Finally, I would like to thank my advisor, Dr. Bevan, for being a wonderful mentor and teacher throughout my PhD. He allowed me freedom to follow my passions in research. I learned to be organized and methodical in my approach to research that will provide me the necessary skills to becoming a successful high-impact researcher. Dr. Bevan puts enormous effort into educating his students, leading me to mentor younger students. I am very grateful for my experience in the Bevan lab.

for my family

TABLE OF CONTENTS

PAGE

LIST OF TABLES

LIST OF FIGURES

1. INTRODUCTION

1.1 Significance and Objective

1.1.1 Significance

Mucus is widely studied as a model polymer, gel, porous media, and as the primary barrier against pulmonary drug delivery. Bodily mucus secretions protect the intestinal, respiratory, and reproductive tracts.[2,3] As the primary obstacle against pulmonary infection, the physicochemical properties of mucus have evolved to trap a wide range of contaminants and infectious agents and rapidly clear them from the lungs, making effective pulmonary drug delivery vectors exceedingly difficult to engineer.[2-6] Identification of rapidly penetrating mucosal drug delivery particles (DDPs) through diffusion measurements and the study of mucosal physiochemical properties are the focus of much research.[7-13] Current techniques generally yield low statistics or are unable to resolve specific interactions between drug delivery particles and mucus. Fundamental theoretical models of physical, chemical, and hydrodynamic interactions between drug delivery particles and mucins have yet to be elucidated.

According to NIH, non-neoplastic lung diseases caused an estimated 235,000 deaths in 2010; chronic lower respiratory disorders are the third leading cause of disease-related death in the US.[14] Aside from their importance as a source of infection and pathology, the lungs are well-suited as a target organ for systemic drug delivery due to their extensive vascularization. Mucus-penetrating DDPs could help treat pulmonary and non-pulmonary disorders. Measuring interactions between DDP coatings and mucus creates a directed approach for engineering DDPs that can efficiently and rapidly penetrate the mucosal barrier and avoid being shed.

Some sources report that diffusion through the mucus gel is affected by nonspecific hydrodynamic interactions effected by the size of the diffusing species,[3,9,10,15] and the density of the effective macromolecular cross-links of the mucin network[3,16,17]. Other sources suggest that while diffusion depends on the efficiency with which the diffusing species can diffuse through pores within the mucus layer,[3,8,18] rate of diffusion is primarily determined by specific particle-mucus interactions.[11-13,19,20] An effective DDP will optimize both size and biomolecular interactions.

Particle-mucus interactions have been widely accepted as a limiting parameter for partitioning into and diffusion through mucus.[11-13,19,20] Some proteins, such as BSA and IgG, along with some protein-coated viruses, such as HPV and Norwalk, have been observed to rapidly penetrate mucus. However, other proteins, such as IgM and IgA, and viruses encapsulated in a phospholipid layer, such as Herpes and HIV, cannot penetrate the mucosal layer. Wide variation exists in the literature in reported rates of diffusion for mucopenetrating biomacromolecules, especially for BSA.[3,8-10] While techniques such as particle tracking and fluorescence diffusion have been used to identify mucus-penetrating biomacromolecules, they have high variability and cannot describe the mechanisms behind penetration. Furthermore, a simple technique for measuring specific and nonspecific intermolecular and hydrodynamic interactions between diffusing colloids does not yet exist.

Mucus’ thixotropic, chemically adhesive gel structure is generated by mucins. Mucins consist of both hydrophobic and hydrophilic regions and carry a net negative charge.[1,3,4,21-24] Along with the physical mucus barrier, electrostatic and steric repulsion prevents partitioning into the mucus layer while hydrophobic and electrostatic interactions cause adhesion to other penetrating vectors.[25] Understanding physical and hydrodynamic properties of mucin gels as well as interactions between potential drug delivery particles and mucin layers is important for drug delivery and for understanding mucus as a model polymer, gel, and porous media.[17]

Biomacromolecular interactions between mucins and drug delivery particle coatings will help predict drug delivery particle diffusion into mucus and the primary interactions between mucus and DDPs. Mucin gel has a thick, compressible and hydrodynamically permeable architecture[25-27] while the polymers used in this dissertation to coat drug delivery particles form dense, impermeable brush layers.[28-30] Analysis of interactions between mucins and drug delivery particle coatings required the development of a novel theoretical technique for measuring steric interactions for asymmetric polymer brush layers. While this analytical theory was developed specifically for application to mucins and polymers coating drug delivery particles, it will find application in a wide array of polymer interactions.

In order to avoid being shed, mucus-penetrating particles must rapidly diffuse through the top mucosal layer. This dissertation will describe a simple, versatile, and accurate technique for measuring the gradient diffusion of fluorescently labeled proteins and drug delivery particles into a mucus polymer solution. Through analyzing gradient diffusion and long time self diffusion of colloidal dispersions prior to analyzing gradient diffusion of those colloidal dispersions through mucus, the specific interactions between the colloids and the mucin polymers can be extracted. This tool will be widely applicable in other fields of colloid and polymer physics, from fluid dynamics and rheology to the formation of photonic crystals.

1.1.2 Objectives

The objective of this dissertation is to investigate the physical as well as hydrodynamic properties of mucus and the colloidal forces that affect the diffusion of potential drug delivery vectors through mucus. Specifically, the interactions between mucin polymers and virus-mimicking polymers are considered. An analytical model relating physicochemical and hydrodynamic properties of mucus solutions to forces affecting DDP diffusion did not previously exist. This work utilized Brownian colloidal probes functionalized with mucus or virus-mimicking polymers to measure thermodynamic and hydrodynamic properties within the layers as well as conservative and dissipative forces between the polymer-coated colloidal probes and mucin polymers and gels. A comprehensive understanding of these interactions between potential drug delivery particles and mucin layers is essential to the development of effective pulmonary drug delivery vectors.[11,17]

In this work, Total Internal Reflection Microscopy was used to measure kT-scale interactions between polymer-functionalized diffusing colloidal probes and polymer-functionalized surfaces above which the probes were levitated via steric repulsion forces. Diffusing colloidal probes are, to date, the most sensitive technique for dynamically measuring forces between macromolecules. This technique measures interactions between biomacromolecules with high statistical relevance. The interactions described via colloidal probes were analyzed using a novel technique that measures the steric potential between asymmetric brush layers, described in the theory section. These interactions were used to inform experimental measurements of gradient diffusion for proteins and virus-mimicking colloids diffusing into mucin polymer solutions. The experimental section describes TIRM of colloidal probes and the use of novel experimental techniques utilizing microfluidic devices to measure the colloid and polymer gradient diffusion. The results presented in this thesis provide vital insight into mucin gel and polymer solutions and their biomolecular interactions with potential drug delivery vectors.

1.2 Background

Currently, a gap exists between the physical and chemical properties of mucin polymers and the thermodynamic and hydrodynamic properties of mucin gels. While physical, electrostatic, and hydrophobic properties of mucins along with their gel structure contribute to rejection of pathogens, considering these properties along with the thermodynamic and hydrodynamic properties of mucin gels holds the key to identifying the mechanisms behind penetrating pathogens. Understanding and mimicking existing biological interactions creates the most direct path towards engineering vectors that utilize those biomolecular properties for efficient penetration. Novel analytical and experimental techniques were developed towards this goal that will also find wide application in polymer physics and fluid dynamics. This section will present the current body of theoretical and experimental research pertaining to the physicochemical properties of mucus and biomacromolecules capable of rapid mucopenetration and the current analysis techniques for polymer brush interactions and polymer and colloidal diffusion.

1.2.1 Mucin Polymers

Mucus gel is composed of 95% water, along with salts, a number of biomacromolecules resultant from cell secretions and cellular debris, proteins that defend against pathogens, and mucin glycoprotein's.[17,22,31] On the nanoscale, mucus behaves as a Newtonian fluid whose viscosity is close to that of water. At the macroscale, mucus behaves as a thixotropic, non-newtonian fluid.[15] Mucin chains make up 50-90% of the molecular weight and generate the characteristic thixotropic, chemically adhesive structure of mucus gels. Individual mucin monomers are comprised of hydrophobic globular protein regions that a flank protein chain lined with polysaccharide chains. The polysaccharide chains form bottle-brush regions tipped with negatively charged carboxyl groups.[1,3,4,21-24] An average of four monomers connect via disulfide bridges to form a mucin chain. While most studies characterize purified and size-separated mucins, wild-type mucin polymers are difficult to characterize due to their polydispersity and high degree of heterogeneity (Fig 1.1).

Approximately nineteen individual cell-associated and secreted mucins have been identified. With molecular weights between 0.5 and 20 MDa, diameters from 3-10 nm,[15] and contour lengths between 200 and 600 nm for cell-associated mucins and hundreds of nanometers up to 1.5 microns for secreted mucins, mucins are comprised of a large and heterogeneous family of glycoproteins.[2] Light scattering experiments have shown mucins as having a stiffened random coil conformation with a radius of gyration around 100 nm.[2,22]. Size measurements depend largely on extraction, purification, and handling techniques used for individual mucus samples. Mucins have also been described as having a wormlike chain[32] or a freely jointed chain[33] conformation.

1.2.2 Surface Adsorbed Mucins

Extensive studies have been conducted on the surface adsorption kinetics and conformation of surface adsorbed mucins. Measuring the conformation of surface

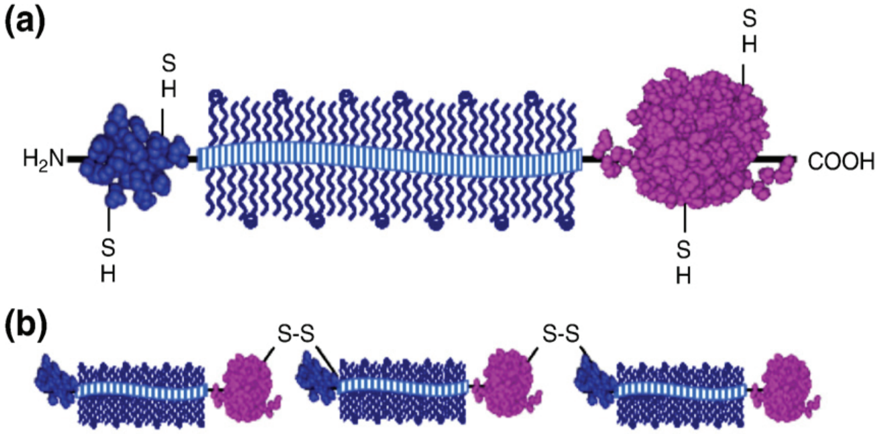

Figure 1.1 Structure of (a) individual mucin monomer with polysaccharide chains forming bottle-brush regions flanked by hydrophobic globular protein regions. Monomers link (b) via disulfide bridges to form mucin chain.[1]

adsorbed mucins is important to interpreting interactions between mucins and other macromolecules on a biomolecular level.[24,25,34] A number of techniques including Field Flow Fractionation,[35] Atomic Force Microscopy,[35,36] Quartz Crystal Microbalance,[34,37,38] Scanning Electron Microscopy and Surface Force Apparatus[25,27,39] have been used to extensively study adsorbed and non-adsorbed mucins. In addition to measuring adsorption/desorption kinetics and conformation, these techniques measure the hydrostatic properties of the mucin layer. Mucus has been found to adsorb in a monolayer conformation with limited desorption.[35] When adsorbed to a hydrophobic surface, the surface density plateaus within three hours[25] and the mucin layer conformation stabilizes with a dense layer creating long-range steric repulsion.[25,27,35,39] Mucins most likely adsorb with hydrophobic regions adsorbing to the hydrophobic slide and bottlebrush hydrophilic regions stretching into the solution.[36] Mucin adsorption to hydrophilic surfaces does not reach density plateau or conformation stabilization within a time scale of hours.[39,40]

Quartz Crystal Microbalance (QCM) and Surface Force Apparatus (SFA) have been used to measure the effect of adsorption conditions on mucin adhesion and on polymer and gel conformation.[34,38] SFA has shown bridging, steric and electrostatic interactions between mucin polymers and each other and between mucin polymer and the opposing surface.[25,27,39] At low density surface coverage, mucins bridge between the opposing surfaces while at high density coverage mucins form sterically repulsive brush layers, consistent with stabilized adsorption conformation exposing bottlebrush polymer regions to the solution.[24,27,37,39] AFM has been used to measure the interaction strength of mucoadhesion.[35,36] SFA, QCM, and AFM rely on the application of external force used to manipulate the system. As a result they alter the polymer system in order to collect data and their sensitivity relies on the spring constant of the apparatus. The techniques currently used to investigate mucus adsorption measure static thermodynamic conditions and cannot measure hydrodynamic or dynamic interactions within the adsorbed mucin layer.[24]

1.2.3 Mucin Polymer Gels

Pulmonary mucus consists of a viscoelastic mucin gel that rests on a dense brush layer comprised of cilia and cell-associated mucins[41] as shown in Figure 1.2a. Concentrated mucin solutions gel through the formation of transient and non-transient associations. Hydrogen bonding, disulfide bridges, and interpenetration of carbohydrate side chains are the primary mechanism for gel formation.[42] Chaotropic agents cause swelling and denaturing in the mucins yet they maintain their gel structure due to the mechanical interactions of the polysaccharide chains.[42,43] At neutral pH the hydrophobic protein regions remain protected in folds stabilized by salt bridges between negatively charged carboxylates and positively charged amino groups. At low pH the hydrophobic regions become exposed and crosslink with other hydrophobic regions.[2] The resultant gel is thixotropic with pores up to 200 nm in diameter[8,15] and carries an overall net-negative charge due to sialic acid and sulfate groups in the mucin glycoproteins. DNA, proteins and lipids also present in the mucus gel increase its viscoelasticity.[23,31]

The periciliary layer, the fluid surrounding the cilia, consists of a dense brush of membrane-spanning mucins and tethered mucopolysaccharides. Steric repulsion generated by the dense macromolecular brush prevents the mucins in the top layer penetrating into the periciliary space, forming two distinct layers, which can be seen in figure 1.2 b, c. The correlation length of the polymer mesh decreases with proximity to the epithelial cells. In one experiment, 40 nm fluorescent dextran probes were excluded from the periciliary layer altogether and 4 nm fluorescent dextran probes diffused to the epithelial cell surface with intermediate sizes penetrating to corresponding intermediate depths.[41]

1.2.4 Mucoadhesive Drug Delivery Vectors

Historically, mucoadhesive biomacromolecules, such as liposomes and chitosan, were developed to deliver pulmonary pharmaceutics. Through mucoadhesion, the drug delivery vectors were predicted to remain in the mucosal layer while slowly released drugs would diffuse into the epithelial cell layer. Atomic Force Microscopy (AFM) has been used to measure interaction strength between mucoadhesive drug delivery vectors and mucus.[44] It was found that the top mucosal layer, along with the drug delivery vectors, were shed before a sufficient amounts of drugs could diffuse into the pericilliary layer and reach the epithelial cell layer.

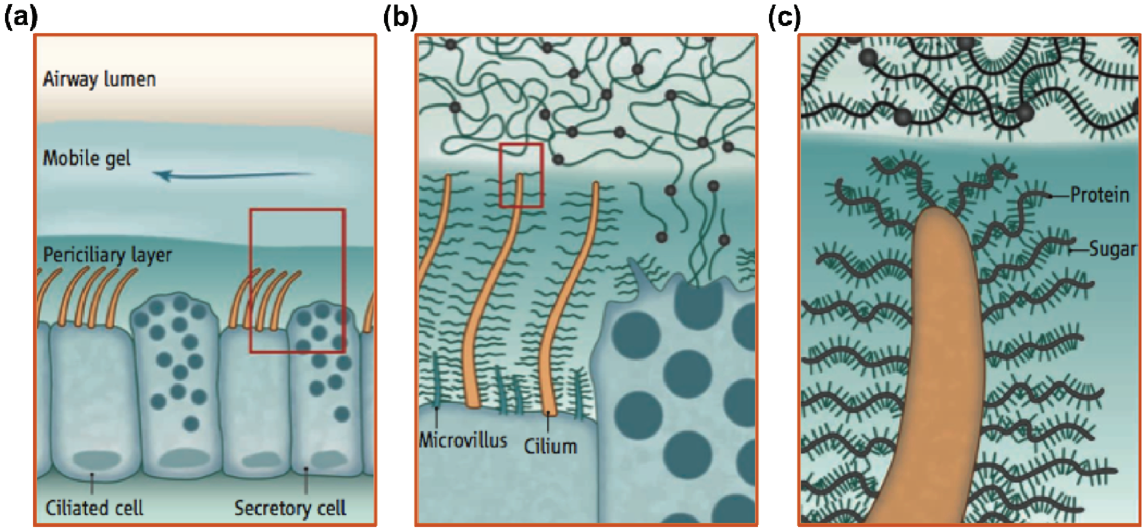

Figure 1.2 Schematic of mucus layer, from macroscopic to microscopic. (a) A layer of secreted, extracellular mucins comprise a mobile gel layer resting atop the dense periciliary layer. (b) The cilia in the periciliary layer are coated by a dense array of cell-associated mucins. The dense array of cell-associated mucins (c) maintain a high degree of steric repulsion due to the bottle brush conformation that results from the polysaccaride coated protein regions.[124]

1.2.5 Mucopenetrating Drug Delivery Vectors

Rapid mucopenetrating vectors are necessary to efficient drug delivery. Pore size and particle-mucus interactions have been widely accepted as the limiting parameters for diffusion through mucus.[11-13,19,20] Mucus has been estimated to have pores up to 200 nm in diameter in particle diffusion experiments and some SEM images[8,15] and between 200 and 500 nm in other SEM images.[12] Some viruses and biomacromolecules rapidly penetrate mucus[3,7-9,45] while other viruses biomacromolecules cannot penetrate the mucosal layer.[3,7,9] A correlation between mucopenetration and size is not direct or ubiquitous. It has been observed that viruses whose outer layer consists solely of proteins tend to penetrate the mucosal barrier while viruses encapsulated in a phospholipid envelope tend not to penetrate.[8,46]

Experimental measurements of nanoparticle diffusion through mucus are limited and highly variable. Particle tracking experiments have shown that nanoparticle size affects diffusion rate. Particles densely coated low molecular-weight polyethelyne glycol (PEG) have been shown to diffuse more rapidly than uncoated particles while particles coated with high molecular weight PEG stick to mucus.[10,11,47] Fluorescence Recovery After Photobleaching (FRAP)[2,3,39] and fluorescence migration have been used to measure bulk diffusion of nanoparticles and macromolecules through mucus.[7-9] In general, previously used diffusion measurement techniques lack the scope to measure a statistically significant number of particles or specificity to elucidate individual interactions.

1.2.6 Physicochemical Properties of Mucus Gel

Mucus is characterized as nonassociated random coil[48] or wormlike chain polymers at low concentrations, an entangled freely jointed chain at intermediate concentrations, and as a cross-linked gel above its sol-gel transition concentration.[6,33,48] Mucus gel behaves on the nanoscale as a Newtonian fluid whose viscosity is close to that of water. On the macroscale mucus behaves as a thixotropic, non-newtonian fluid.[15] The apparent macroviscosity of mucus is inversely related to shear rate. As shear rate increases, the mucus macroviscosity decreases from a viscosity 10^4-10^6 times that of water[7,15] to a value close to the viscosity of water.[49] Beating cilia in the lower, periciliary layer, push the upper mucus layer through the lungs to clear pathogens, creating shear in the upper layer.[49] It has been suggested that mucus flows at 10-20 mm/min in the trachea and more slowly deeper in the lungs,[49,50] though that number is difficult to verify and not extensively reported in literature. Coughing, sneezing, blinking, and copulation all significantly shear and decrease the macroviscosity of mucus.

1.2.7 Current Models for Analyzing Polymer Interactions

Flory's equations stipulate that grafted polymer brushes in a moderate or good solvent will form a polymer brush layer whose thickness is directly proportional to its polymerization index. In this model, polymers are considered to adsorb to the surface on one end and all polymers extend the same length with the other end, leading to a brush layer described by a step function.[51] Milner's theory determines the thermodynamic equilibrium by balancing the elastic energy within a polymer (generated by its tendency to minimize its configurational free energy by adopting a worm-like chain conformation) with the polymeric preference to be wet by the solvent.[52] Milner's equation for the free energy of symmetric brush layers can be used to determine the uncompressed brush layer thickness and energy associated with compression under small compressive force.[53] Milner's equation uses a parabolic model to describe the thermodynamics and steric repulsive forces of interacting compressible brush layers for symmetric brush layers or layers that can be realistically described using a theoretical mean field. The bisection theory[54,55] uses properties determined through symmetric interactions to describe steric interactions between asymmetric polymer brush layers. The bisection theory is based on the stipulation that brush layers maintain their characteristic compressibility and will experience the same proportion of compression in response to a certain force.

1.2.8 Models for Colloidal Diffusion

Measuring diffusion of drug delivery particles through mucus is necessary for efficient pulmonary drug delivery. Nonspecific hydrodynamic interactions along with specific biomacromolecular interactions effect colloidal diffusion. Characterizing colloidal diffusion is paramount to designing efficient drug delivery systems[56,57] as well as effective microfluidic devices.[58-60] Colloids can either diffuse down a concentration gradient (gradient diffusion) or they can diffuse within a self-similar suspension (self-diffusion). The diffusion of colloids within a self similar suspension over a long period of time can be observed by tagging or photobleaching some population of the colloids and watching the evolution of the entire suspension over time. Gradient diffusion is driven by entropy chemical potential differences while self diffusion is driven solely by entropy.

Few techniques exist capable of measuring gradient and self diffusion. Microfluidic devices can measure a wide range of systems. Microfluidics utilizes flow at low Reynolds numbers where flow is laminar and the inertia negligible.[59,61,62,63] Elimination of inertial effects enables flow manipulation and analysis of additional hydrodynamic complexities such as pressure gradients, electrical potentials, magnetic potentials, and capillary forces.[58,64-66] Specific and nonspecific interactions in particle, polymers, and non-newtonian fluids can be measured[59,67,68] and diffusion more easily calculated in stokesian flow.[69]

1.3 Summary and Dissertation Outline

This dissertation is organized as follows: *Chapter 2* describes the theory of conservative and disappative forces that contribute to steric stabilization and diffusion of colloids. This chapter will provide the theoretical basis and concepts for understanding the techniques used in this dissertation. *Chapter 3* describes the experimental procedures used in this dissertation. *Chapters 4 and 5* show the results of the experiments conducted. *Chapter 4* describes thermodyamic and hydrodynamic interactions between virus-mimicking drug delivery particles and mucin polymer layers. A universally applicable exponential equation set to Milner's equation for steric potentials of brush layers captured interactions of symmetric and asymmetric steric potentials and diffusivities. Measured particle trajectories were additionally analyzed using bayesian inference analysis to measure colloidal conservative and dissipative forces from these ensemble colloidal particle probe excursions normal to the underlying substrate. Particle diffusivity profiles followed known hydrodynamic contributions that include the surface separation dependence and the effect of both adsorbed polymer or charge-carrying layers and adsorbed gel layers in solution. *Chapter 5* describes the diffusion of virus mimicking colloidal particles into a mucus suspension. In this chapter, a novel analytical technique was utilized to measure the diffusion of fluorescent material across a microfluidic channel. The experiments utilized a constant pressure microfluidic system to inject one fluorescent and one nonfluorescent solution into a Y-junction microfluidic channel. Gradient and long time self diffusion was observed and modeled for virus mimicking drug delivery particles prior to measuring diffusion through mucus. Using this methodical approach, specific and nonspecific interactions between those DDP's and mucus could be separated. The analytical tool yields unprecedented resolution that facilitates analysis of a wide array of colloidal phenomena. *Chapter 6* summarizes the conclusions drawn based on the research in this dissertation. *Chapter 7* describes ongoing and future work related to the findings of this dissertation.

2. THEORY

2.1 Colloidal and Surface Interactions

2.1.1 Net Potential Energy Interactions

The separation-dependent net potential energy for spherical colloidal particles interacting with each other and an underlying surface depends on the combination of surface and body forces acting on the particles. In this dissertation, a number of these forces are considered, including: gravitational, van der Waals, steric, electrostatic, polymer tethering, and hydrodynamic interactions. The net interaction potential, *u*(*h*), can be computed from superposition of contributing potentials as according to the equation:

$$\begin{aligned} u(z,r,a) = u_G^{pf}(h) + u_E^{pp}(r) + u_S^{pp}(r) + u_S^{pw}(h) + u_V^{pp}(r) \\ + u_V^{pw}(h) + u_T^{pw}(h) + u_H^{ps}(a) + u_H^{pw}(h) \end{aligned} \tag{2.1}$$

where h is surface-to-surface separation of the particle and wall relative to contact between the particle and the underlying wall at $h=0$ and r corresponds to the particle surface-to-surface separation relative to contact at $r=0$. Superscripts designate interactions as between particle and field (pf), particle and particle (pp), particle and wall (pw), and particle and solution (ps). Subscripts refer to individual contributing interactions: gravitational (G), electrostatic (E), steric (S), van der Waals (V), polymer tethering (T), and hydrodynamic interactions (H).

2.1.2 Gravitational Interactions

The gravitational potential energy of each particle levitating over an underlying surface depends on its elevation, *h* and the particle's buoyant weight, *G*. The gravitational potential energy is given as

$$u_G\left(h\right)=Gh=mgh=\frac{4}{3}\pi a^3\left(\rho_p-\rho_f\right)gh \tag{2.2}$$

where a is particle radius, m is the buoyant mass, g is acceleration due to gravity, and ρ_p and ρ_f are the particle and fluid densities.

2.1.3 van der Waals Interactions

The van der Waals attraction between flat plates at a separation, l, is given as,

$$E_V\left(l\right)=-\frac{A\left(l\right)}{12\pi l^2} \tag{2.3}$$

where $A(l)$ is the Hamaker function, which can be computed from Lifshitz theory[70] to include retardation and screening effects.[71] To obtain the particle-wall potential energy, $u_V(h)$, the Derjaguin approximation is then applied as,[72]

$$u_A\left(h\right)=2\pi a\int_h^\infty E_X\left(l\right)dl \tag{2.4}$$

where the subscript "X" indicates this can be used for any potential between flat plates. The resulting theoretical potential from Eqs.(2.3)and(2.4) can be approximated with an inverse power law fit as,[73,74]

$$u_V\left(h\right)=-Aa\left(h+\delta_V\right)^{-p} \tag{2.5}$$

where p is a non-integer power, δ_V is a surface roughness correction factor, and A is an effective Hamaker constant.

2.1.4 Electrostatic Interactions

Glass acquires a negative surface charge when submerged in an aqueous solvent. The layer of ions immediately adjacent to the surface, known as the Stern layer, attracts a second outer layer of counterions to create an electrostatic double layer. The characteristic length scale of the electrostatic double layer, known as the Debye length, depends upon the solvent conditions. When the Debye length, κ^{-1}, is smaller than particle-wall separations ($h/\kappa^{-1}>1$) and significantly smaller than particle radius ($a/\kappa^{-1}>>1$), the Derjaguin approximation accurately models the electrostatic interactions between overlapping double layers. Specifically, for a 1:1 electrolyte solution, the interaction is given by:

$$u_{edl}(h) = B\exp(-\kappa h)$$

$$B = 64\pi\varepsilon a\left(\frac{k_B T}{e}\right)\tanh\left(\frac{e\Psi_p}{4k_B T}\right)\tanh\left(\frac{e\Psi_w}{4k_B T}\right) \tag{2.6}$$

$$\kappa = \left(\frac{2CN_A e^2}{\varepsilon kT}\right)^{\frac{1}{2}}$$

where ε is the media dielectric permittivity, k_B is Boltzmann's constant, T is absolute temperature, e is the elemental charge, Ψ_p and Ψ_w are the Stern potentials for the particle and wall, respectively, C is the bulk electrolyte concentration, and N_A is Avogadro's number. The wall is assumed to be of infinite length. The Derjaguin approximation (Eq. 2.4) can again be applied to determine particle-particle electrostatic interactions and the magnitude of the particle-particle interactions will be exactly half of the magnitude particle-wall electrostatic interactions at the same solvent conditions, independent of particle size.

2.1.5 Symmetric Steric Interactions

The thermodynamics of symmetric parabolic brush interactions can be determined analytically using Milner's brush theory which accounts for the elastic energy within a polymer and solvent quality. Fitting Milner's equation for the free energy of symmetric brush layers, uncompressed brush layer thickness and energy associated with compression under small compressive force can be measured.

To understand the repulsion between adsorbed macromolecular layers with a brush architecture, it is useful to start by considering the free energy change of a single brush layer given by,[75]

$$\frac{f(\delta)}{f_0}=\left(\frac{5}{9}\right)\left[\left(\frac{\delta}{\delta_0}\right)+\left(\frac{\delta}{\delta_0}\right)^2-\left(\frac{1}{5}\right)\left(\frac{\delta}{\delta_0}\right)^5\right] \tag{2.7}$$

where $f(\delta)$ is the free energy per unit area of a brush compressed to a height, $\delta<\delta_0$, δ_0 is the uncompressed brush layer thickness, and f_0 is the free energy of an uncompressed brush, as shown in Fig. 2.1.

Milner's equation for the energy associated with compression of symmetric brushes can be fit with an exponential which simplifies its use and also provides a means to model more complex macromolecular brush interactions. For compressed brushes with $\delta/\delta_0>1/2$ an exponential nearly identical to Eq. (2.7) is given by,

$$\frac{f(\delta)}{f_0}=1+\Gamma\exp\left[-\gamma\left(\frac{\delta}{\delta_0}\right)\right] \tag{2.8}$$

where Γ and γ are dimensionless constants. The values of Γ and γ can be adjusted in Eq. (2.8) to model adsorbed macromolecular layers with different architectures. With Eq. (2.4) and (2.8), the force, F, to compress two non-interpenetrating macromolecular brush layers between a sphere and wall at a separation of h is given for $h<\delta_{1,0}+\delta_{2,0}$ as,

$$F_s(h)=4\pi a\left[f(h_1)-f(\delta_{1,0})+f(h_2)-f(\delta_{2,0})\right] \tag{2.9}$$

where $h=h_1+h_2$, h_1 and h_2 correspond to the compressed layer thicknesses of layers 1 and 2, and $\delta_{1,0}$ and $\delta_{2,0}$ are the uncompressed thicknesses of layers 1 and 2. In the case of symmetric layers, $h_1=h_2=h/2$ which can used to simplify Eq. (2.9) to,

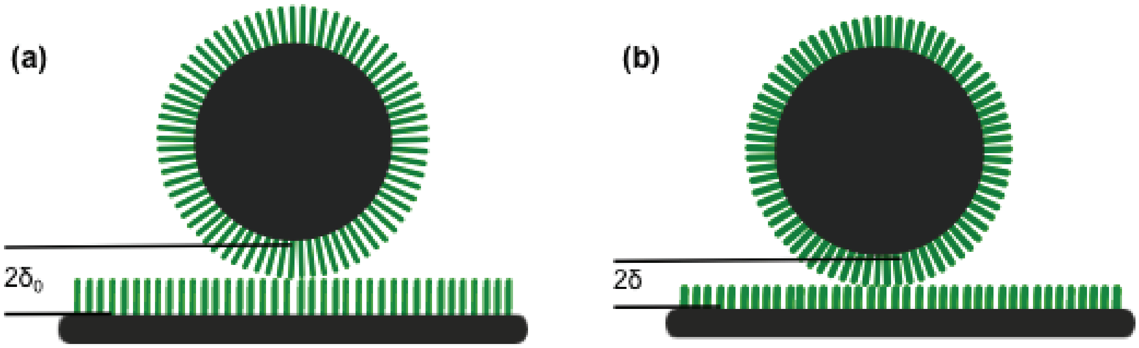

Figure 2.1 Schematic of colloidal particles (grey circle) levitated over polymer brush coated wall (grey rectangle) *via* steric repulsive forces between the physiadsorbed pluronic polymer brushes (green). (a) shows dense, uncompressed pluronic layers. δ_0 corresponds to the uncompressed brush height. (b) shows compressed pluronic layers. δ corresponds to the compressed brush height of the symmetric pluronic layers.

$$F_s(h) = 4\pi a f_0 \delta_0 \Gamma \exp\left[-\left(\frac{\gamma}{2}\right)\left(\frac{h}{\delta_0}\right)\right] \tag{2.10}$$

which can be integrated to give the potential between two symmetric macromolecular layers as,

$$u_s(h) = 16\pi a f_0 \delta_0 \left(\frac{\Gamma}{\gamma}\right) \exp\left[-\left(\frac{\gamma}{2}\right)\left(\frac{h}{\delta_0}\right)\right] \tag{2.11}$$

where, again, Γ and γ can be adjusted to represent different macromolecular architectures.

2.1.6 Overall Net Symmetric Interactions

The overall potential energy will not depend on electrostatic interactions at physiological solvent conditions, at C = 150 mM with $\kappa^{-1} \approx 0.1$ nm, or van der Waals interactions, screened by repulsive steric interactions, and can be written as

$$u(h) = u_s(h) + u_g(h) \tag{2.12}$$

The gravitational and steric potentials from Eqs. (2.2) and (2.11) can then be substituted into Eq. (2.12) which yields,

$$u(h) = 16\pi a f_0 \delta_0 \left(\frac{\Gamma}{\gamma}\right) \exp\left[-\left(\frac{h\gamma}{2\delta_0}\right)\right] + Gh \tag{2.13}$$

The height of minimum potential energy can be solved as analytically as,

$$h_m = \frac{2\delta_0}{\gamma} \ln\left(\frac{16\pi a f_0 \Gamma}{2G}\right) \tag{2.14}$$

with the dimensionless constant, $\Gamma_{m,}$, defined as

$$\Gamma_m = 16\pi a f_0 \Gamma \tag{2.15}$$

and substitute into Eq. (2.14) to get

$$u_s(h) = \Gamma \gamma^{-1} \delta_0 \exp\left(-\frac{h\gamma}{2\delta_0}\right) \tag{2.16}$$

Using the interaction potential at the equilibrium height as a reference state,

$$u(h) - u(h_m) = u_s(h) - u_s(h_m) + u_g(h) - u_g(h_m) \tag{2.17}$$

and solving for the difference of the potentials gives and substituting Eq (2.14) for h_m:

$$u_s(h) - u_s(h_m) = \frac{\Gamma_m}{\gamma} \delta_0 \exp\left[-\left(\frac{h\gamma}{2\delta_0}\right)\right] - \frac{\Gamma_m}{\gamma} \delta_0 \exp\left[-\ln\left(\frac{\Gamma_m}{2G}\right)\right] \tag{2.18}$$

which simplifies to

$$\frac{\Gamma_m}{\gamma} \delta_0 \exp\left[-\left(\frac{h_m \gamma}{2\delta_0}\right)\right] = \frac{2G}{\gamma} \tag{2.19}$$

Now say that

$$\frac{\Gamma_m}{\gamma} \delta_0 \exp\left[-\left(\frac{h_m \gamma}{2\delta_0}\right)\right] = \frac{\Gamma_m}{\gamma} \delta_0 \exp\left[-\left(\frac{h_m \gamma}{2\delta_0}\right)\right] \cdot \left(\frac{2G}{\gamma}\right) \cdot \left(\frac{\gamma}{2G}\right) \tag{2.20}$$

so that substituting Eq. (2.19) gives:

$$\frac{\frac{\Gamma_m}{\gamma}\delta_0 \exp\left[-\left(\frac{h\gamma}{2\delta_0}\right)\right]}{\frac{\Gamma_m}{\gamma}\delta_0 \exp\left[-\left(\frac{h_m\gamma}{2\delta_0}\right)\right]}\left(\frac{2G}{\gamma}\right)=\left(\frac{2G}{\gamma}\right)\exp\left[-\left(\frac{\gamma}{2\delta_0}\right)\left(h-h_m\right)\right] \tag{2.21}$$

Substituting this result into Eq. (2.18) and finally solving for the overall net potential energy for symmetric brush layers interacting under small compression can be simplified as,

$$\frac{u\left(h\right)-u\left(h_m\right)}{k_BT}=\frac{G}{k_BT}\left[\frac{2\exp\left(\frac{-\gamma}{2\delta_0}\right)\left(h-h_m\right)-1}{\gamma}+\left(h-h_m\right)\right] \tag{2.22}$$

2.1.7 Asymmetric Steric Interactions

Asymmetric layer interactions are generally analyzed by considering the layers as a theoretical mean field assuming that each layer has similar architectures. Interactions between asymmetric macromolecular brush layers with contrasting architectures cannot be accurately modeled with Milner's brush theory alone. However in this case, Shim's bisection theory can be used in conjunction with the exponential fit to Milner's equation to model interactions between two distinct macromolecular layers. The main assumption in Shim's bisection theory is that each polymer layer in the asymmetric case compresses in response to a given force in the same manner as that polymer compresses for symmetric macromolecular layers. The generalized exponential fit to Milner's brush theory then enables Shim's bisection theorem to be extended from use on asymmetric Flory brush layers to use for asymmetric parabolic brush layers. Values of δ_0 and f_0 determined by the Milner brush theorem for symmetrical layers could be used to compare interactions of asymmetrical layers.

For two interacting asymmetric macromolecular layers, the bisection rule states that the total thickness of two different layers under compression at a given force is equal to the average thickness of symmetric layers under the same compressive force and can be written as,[55,76]

$$h(F)=\frac{2h_1(F)+2h_2(F)}{2} \tag{2.23}$$

The force generated between asymmetric macromolecular layers can then be calculated by: (1) solving Eq. (2.10) for the heights of each layer, h_1 and h_2, at a given compressive force, F, and inserting them into Eq. (2.23), (2) defining $\lambda_i=\delta_{0,i}/\gamma_i$ and $\Lambda_i=\Gamma_i f_{0,i}$, and (3) performing some algebra to solve for $F(h)$. This gives the force between two asymmetric layers as,

$$F_A(h)=8a\Lambda_1^{\frac{\lambda_1}{\lambda_1+\lambda_2}}\Lambda_2^{\frac{\lambda_2}{\lambda_1+\lambda_2}}\exp\left(-\frac{\lambda_1}{\lambda_1+\lambda_2}\right) \tag{2.24}$$

using Eq. (2.10) to find h_1 and h_2 at a given compressive force, F and the dimensionless constants for each layer are defined as $\lambda_i=\delta_{0,i}/\gamma_i$ and $\Lambda_i=\Gamma_i f_{0,i.}$

This force can be integrated to give the separation-dependent potential between asymmetric layers as,

$$u_s(h)=8a\Lambda_1^{\frac{\lambda_1}{\lambda_1+\lambda_2}}\Lambda_2^{\frac{\lambda_2}{\lambda_1+\lambda_2}}(\lambda_1+\lambda_2)\exp\left(-\frac{\lambda_1}{\lambda_1+\lambda_2}\right) \tag{2.25}$$

which for the case of two asymmetric layers with the same architecture (i.e. $\Gamma=\Gamma_1=\Gamma_2$ and $\gamma=\gamma_1=\gamma_2$) becomes,

$$u_A(h)=8\pi a\frac{\Gamma}{\lambda}f_{0,1}^{\frac{\lambda_1}{\lambda_1+\lambda_2}}f_{0,2}^{\frac{\lambda_2}{\lambda_1+\lambda_2}}(\delta_{0,1}+\delta_{0,2})\exp\left(-\frac{h}{\delta_{0,1}+\delta_{0,2}}\right) \tag{2.26}$$

and reduces to Eq. (2.11) for symmetric layers when $\delta_0 = \delta_{0,1} = \delta_{0,2}$ and $f_0 = f_{0,1} = f_{0,2}$.

2.1.8 Overall Net Asymmetric Interactions

The minimum potential energy and energy at thermodynamic equilibrium are determined in the same fashion as the symmetric case previously described. To begin, the most probable height can be found with Eq. (2.12) as,

$$h_m = \frac{\delta_{0,1} + \delta_{0,2}}{\lambda} \ln\left(\frac{\Gamma_A}{G}\right) \tag{2.27}$$

where $\Gamma_A = 8\pi a f_{0,1}^{\frac{\lambda_1}{\lambda_1+\lambda_2}} f_{0,2}^{\frac{\lambda_2}{\lambda_1+\lambda_2}}$ .Again using the equilibrium height as a reference state, the overall potential energy for asymmetric brush layers interacting under small compression can be written as,

$$\frac{\Gamma_A}{\lambda}\left(\delta_{0,1} + \delta_{0,2}\right)\exp\left(-\frac{h_m \lambda}{\delta_{0,1} + \delta_{0,2}}\right) = G\frac{\delta_{0,1} + \delta_{0,2}}{\lambda} \tag{2.28}$$

If

$$\begin{aligned} &\frac{\Gamma_A}{\lambda}\left(\delta_{0,1} + \delta_{0,2}\right)\exp\left(-\frac{h\lambda}{\delta_{0,1} + \delta_{0,2}}\right) = \\ &\frac{\Gamma_A}{\lambda}\left(\delta_{0,1} + \delta_{0,2}\right)\exp\left(-\frac{h\lambda}{\delta_{0,1} + \delta_{0,2}}\right)\left(G\frac{\delta_{0,1} + \delta_{0,2}}{\lambda}\right)\left(G\frac{\delta_{0,1} + \delta_{0,2}}{\lambda}\right)^{-1} \end{aligned} \tag{2.29}$$

then substituting Eq (2.29) and finally solving, for the overall potential energy for asymmetric brush layers interacting under small compression:

$$\frac{u(h) - u(h_m)}{k_B T} = \frac{G}{k_B T}\left[\frac{\left(\delta_{0,1} + \delta_{0,2}\right)\left[\exp\left(\frac{-\gamma}{\delta_{0,1} + \delta_{0,2}}\right)\right](h - h_m) - 1}{\gamma} + (h - h_m)\right] \tag{2.30}$$

2.1.9 Tethering Interactions

For large and/or highly-charged polymers (*e.g.* mucins, polyelectrolytes, proteins), polymers chains can become physically entangled and/or bound to create tethers between opposing surfaces. Relationships between force, *F*, and extension, *h*, for macromolecular tethers can be modeled as a Hookean spring,

$$F_H\left(h\right) = \frac{3k_BT}{2PL_T}h \tag{2.31}$$

a freely jointed chain,[77]

$$F_F\left(h\right) = \frac{k_BT}{2P}\mathbf{L}^{-1}\frac{h}{L_T} \tag{2.32}$$

or a worm like chain,[78]

$$F_W\left(h\right) = \frac{k_BT}{P}\left[\frac{1}{4}\left(1-\frac{h}{L_T}\right)^{-2} - \frac{1}{4} - \frac{h}{L_T}\right] \tag{2.33}$$

Where *P* is the persistence length where *P*=0.5*b* (*b* is the Kuhn Length), L_T is the tether contour length, and *L* is the Langevin function given as,

$$L\left(x\right) = \coth\left(x\right) - x^{-1} \tag{2.34}$$

For small extensions, all three models converge to the Hookean spring and the potential for a single tether becomes,

$$u_T\left(h\right) = \int_0^h F_T\left(x\right)dx = \left(\frac{3k_BT}{4PL_T}\right)h^2 \tag{2.35}$$

and for *N* tethers acting in parallel thepotential becomes,[29]

$$u_T\left(h\right) = \left(\frac{3k_BT}{4P}\right)h^2\sum_{i=1}^{N}L_{T,i}^{-1} \tag{2.36}$$

2.2 Colloidal Diffusion

2.2.1Colloidal Gradient and Self Diffusion

Colloidal diffusion in a solution can be described by Fick's laws. Fick's first law states,[79]

$$J = -D(\phi)\frac{\partial \phi}{\partial x} \tag{2.37}$$

where J is the flux of Brownian particulates, D is the particulate diffusivity and Φ is the concentration of particulates in the test solution. Using the continuity equation, the change in concentration of the test solution over time, t, can be found as,

$$\frac{\partial \phi}{\partial t} = -\nabla \cdot J \tag{2.38}$$

Fick's second law can then be derived as,[79]

$$\frac{\partial \phi}{\partial t} = \nabla \cdot \left(D\frac{\partial \phi}{\partial x} \right) \tag{2.39}$$

The diffusivity of a Brownian particle in solution can be determined with Einstein's equation as,[80]

$$D_0 = \frac{k_B T}{f} \tag{2.40}$$

where D_0 is the Stokes diffusivity coefficient and is the friction between the Brownian particle and the solution determined from Stoke's law[81] where μ corresponds to the solution viscosity. Combined, the Stokes-Einstein equation gives the diffusivity of a Brownian particle in solution in the absence of any additional conservative or nonconservative forces as,

$$D_0 = \frac{k_B T}{6\pi\mu a} \tag{2.41}$$

In a concentrated particle solution, particle interactions can hinder particle diffusion due to particle-particle hydrodynamic interactions. In this case, Bachelor's equation can be used to determine the diffusivity as,[82]

$$D(\phi) = D_0 K(\phi) \frac{d\left[\phi Z(\phi)\right]}{d\phi} \tag{2.42}$$

where $K(\Phi)$ is the sedimentation coefficient which for hard spheres is defined as,[83]

$$K(\phi) = (1 - 6.55\phi) \tag{2.43}$$

and $Z(\Phi)$ is the compressibility factor given by the equation,[83]

$$Z(\phi) = \frac{\Pi}{nk_B T} = 1 + A_2\phi + \ldots \tag{2.44}$$

where Π is the osmotic pressure, n is number density, and A_2 is the second virial coefficient. In the case of dilute solutions where interparticle interactions are negligible, Eq. (2.43) reduces to,

$$D(\phi) = D_0 \tag{2.45}$$

In this scenario, the solution to Fick's second law for two semi infinite solutions joined at x=0 where $\Phi_1(t = 0) = 1$ and $\Phi_2(t=0) = 0$ is,

$$\phi(x) = \bar{\phi} + \frac{\Delta\phi}{2} erf\left(\frac{x}{\sqrt{4D_0 t}}\right) \tag{2.46}$$

For the case of long time self diffusion in a concentrated suspension where particle interactions must be taken into account, neither $K(\Phi)$ nor $Z(\Phi)$ are constant. However, the overall concentration remains constant. To monitor self diffusion in experiment, one of the solutions must be labeled (e.g. fluorescence) to measure the change in concentration. As such, the governing equations become

$$J_f = -D(\phi_S)\frac{\partial \phi_f}{\partial x} \tag{2.47}$$

where J_f corresponds to the flux of fluorescently tagged particles, is the particulate concentration of the solution, and is the concentration of the fluorescently tagged particles. With the diffusivity constant in this case, the concentration with respect to time can still be described with Fick's second law and solved using the solution

$$D(\phi) = D_0 K(\phi)\frac{d\left[\phi Z(\phi)\right]}{d\phi} = D_1 \tag{2.48}$$

For gradient diffusion in a concentrated suspension where particle interactions must be taken into account, K(Φ), Z(Φ) and Φ all vary as a function of position and time. As such, Bachelor's equation does not give a constant solution and Fick's second law

$$\frac{\partial \phi}{\partial t} = \nabla \cdot \left\{ D\left[\phi(x)\right]\frac{\partial \phi}{\partial x} \right\} \tag{2.49}$$

yields a differential equation which cannot be solved analytically.

2.2.2Diffusivity Perpendicular to a Wall

Measurements of the time-dependent probability, *p*(*h*,*t*), can be used to obtain both *U*(*h*) and the separation dependent diffusivity, *D*(*h*), as described by the Smoluchowski equation,[84]

$$\frac{\partial p(h,t)}{\partial} = \frac{\partial}{\partial h} D(h) \left[\frac{\partial p(h,t)}{\partial h} + \frac{p(h,t)}{k_B T}\frac{U(h)}{dh} \right] \tag{2.50}$$

which reduces to Boltzmann's equation in the long-time limit as the system approaches equilibrium. In previous work, we have reported non-equilibrium analysis of colloidal trajectories to obtain *U*(*h*) and *D*(*h*).[85] Measured *D*(*h*) are modeled using,

$$D(h) = D_0 f(h) \tag{2.51}$$

Where $f(h)$ accounts for particle-wall hydrodynamic interactions from Brenner.[86] Lubrication forces increase as a particle's approaches a wall and slows particle diffusion.Brenner's equation for particle motion perpendicular to a wall takes this into account as a correction factor and for simplicity, this solution has been fit with a rational expression as,[87]

$$f\left(h\right)=\frac{6h^2+2ah}{6h^2+9ah+2a^2} \tag{2.52}$$

2.3Experimental Measurements

2.3.1Total Internal Reflection Microscopy (TIRM)

Total internal reflection uses a laser to create an evanescent wave near a reflective surface and the intensity of evanescent wave scattering from a colloidal particle can be directly related to its height above the surface. The evanescent wave intensity decays exponentially, small height excursions cause large changes in scattering intensity. The height of colloidal particles diffusing over a wall can be calculated using the intensity of the scattered lightwith the equation,

$$h=-\beta^{-1}\ln\left(\frac{I\left(h\right)}{I_0}\right) \tag{2.53}$$

Where I corresponds to the intensity of scattered light, I_0 is the scattering intensity of light from a particle in contact with the wall, and β^{-1} is the evanescent wave decay length given as,

$$\beta^{-1}=\frac{\lambda_1}{4\pi\sqrt{\left(n_1\sin\theta_1\right)^1-n_2^2}} \tag{2.54}$$

where λ_1 is the wavelength of the incident laser light, n_1 and n_2 are the refractive indices of the incident and transmission media, respectively, and θ_1 corresponds to the angle of incidence of the laser at the reflecting surface.

By measuring a statistically significant number of height excursions of a spherical particle above a planar wall surface, a normalized equilibrium height histogram, $p(h)$, can be generated. The net separation dependent interaction potential, $U(h)$, can determined with Boltzmann's equation as,[88]

$$U(h) = -k_B T \ln\left[\frac{p(h)}{A}\right] \tag{2.55}$$

where A is a normalization constant related to the total number of height observations. The resulting net potential can be analyzed and separated into individual components that contribute to the overall potential energy or Brownian colloidal particles levitated over a wall.

3. EXPERIMENTAL

3.1 Materials and Equipment

3.1.1 Generic Chemicals

The following chemicals were used as received without further purification:

- potassium hydroxide (KOH), isopropanol (IPA), methanol, ethanol, acetone, toluene (Fisher Scientific, Pittsburgh, PA)

  1-octadecanol, sodium hydroxide (NaOH), chloroform, 200-proof anhydrous ethanol, ~192,000 Mw polystyrene (PS), Polystyrene-4-sulfonate (PSS), Bovine Serum Albumin (BSA), BSA Fluorecein isothiocyanate (FITC) conjugate, Concanavalin A (ConA), ConA FITC conjugate, Polyallylhydrochloride (PAH), phosphate buffer, sodium azide (NaN_3), lyophilized mucus from bovine submaxillary glands (BSM) (Sigma-Aldrich Company, St. Louis, MO)
- sodium chloride (NaCl) (Acros Organics, Morris Plains, NJ)
- nitrogen (N2, Airgas, Salem, NH)
- poly(ethylene oxide)-poly(propylene oxide)-poly(ethylene oxide) triblock copolymer with segment molecular weights of 5400/3300/5400 g/mol (PEO-PPO-PEO, F108 Pluronic®, BASF, Wyandotte, MI)
- Sylgard polydimethylsiloxane (PDMS) (Dow Corning, Midland, MI)

3.1.2 Wall Surfaces and Particles

- nominal 3.13 μm, 2.34 μm, 0.97 μm and silica (SiO_2) colloids (ρ=1.96 g/ml, Bangs Laboratories, Fishers, IN)
- No 1. 22×22, 18×18, 24×50mm coverslips and 24×75mm microscope slides (Gold Seal, Corning, NY)

- nominal 0.7 μm, 0.5 μm, 0.29 μm, 0.14 μm, 0.047 μm diameter Fluoro-Max green fluorescent polymer microspheres in water, 0.110 μm, 0.05 μm polymer microsphere in water (Thermo Scientific, Waltham, MA)
- 24 mm × 75 mm glass plain microscope slides (Fisher Scientific, Pittsburgh, PA)
- No.1 18mm×18mm (Corning, Corning, NY)
- No 1. 22×22, 18×18, 24×50mm coverslips and 24×75mm microscope slides (Gold Seal, Corning, NY)

3.1.3 Photolithography

- 100 mm diameter, 100 μm thick mechanical grade, round silicon wafer (University Wafer, Boston, MA)
- Photomask (CAD/Art Services, Inc., Bandon, OR)
- negative photoresist SU-8 3010 and developer (MicroChem, Newton, MA)

3.1.4 Constant Pressure Microfluidic System

- 0.5 in 23 G blunt needle (SAI Infusion Technologies, Libertyville, IL)
- Series R-800-10 0-10 PSI Subminiature Regulators (Coast Pneumatics, Anaheim, CA)
- 0.025 in outer diameter, 0.017 in inner diameter, 0.50 in long stainless steel tubes (New England Small Tube Corporation, Linchfield, NH)
- 3.5 mL screw cap Cryovial (VWR, Batavia, IL)
- Digital gauge, plastic case, 5 PSI (McMaster Carr, Princeton, NJ)
- Miniature clear EVA tubing, 0.02 in inner diameter, 0.06 in outer diameter (McMaster Carr, Princeton, NJ)
- Harris Uni-Core hole punch, 0.75mm inner diameter (Ted Pella, Redding, CA)

- Extra wide space 4-outlet aluminum manifold (McMaster Carr, Princeton, NJ)
- Polybutylene and brass push-to-connect fitting (McMaster Carr, Princeton, NJ)
- Colored polyurethane tubing, 0.125 in inner diameter, 0.25 in outer diameter (McMaster Carr, Princeton, NJ)
- Hand-operated miniature air control valve (McMaster Carr, Princeton, NJ)

3.1.5 Equipment and Instruments

- 15 mW 632.8 nm Helium-Neon laser (Melles Griot, Carlsbad, CA)
- 12-bit CCD camera (ORCA-ER, Hamamatsu, Japan)
- Axio Imager A1m optical microscope (Zeiss, Oberkocken, Germany)
- 10x and 40× objective (air N.A.=0.65) (Achroplan, Oberkocken, Germnay)
- ZEN3600 ZetaSizer Nano-ZS (Malvern Instruments, Worcestershire, U.K.)
- Eppendorf Minispin Plus bench-top centrifuge (Eppendorf, Hamburg, Germany),
- XS64 Mettler Toledo lab balance (Mettler Toledo, Columbus, OH)
- Accument® AR20 pH and conductivity probe, Fisher Scientific Rotating Mixers (Fisher Scientific, Pittsburgh, PA)
- Branson 1510 ultrasonicator (Branson Ultrasonics Corporation, Danbury, CT)
- PE-IIA plasma system (Technics West, Inc., Anaheim, CA)
- Best Tools Smart Coater 200 (Weinview, St. Louis, MO)
- WS-400BZ-6NPP/LITE Spin Coater (Laurell Technologies Corporation, North Wales, PA)
- EVG 620 mask aligner (EV Group, Albany, NY)
- Digital Hot Plate 730 Series (Dataplate, UK)
- Sloan Dektak IIA profilometer (Veeco, Somerset, NJ)

- Axiovert 200M with LSM 5 pascal scanner and confocal laser scanning microscope (Zeiss, Germany)
- 10-350mW 488nm (blue) laser (Melles Griot, Carlsbad CA)

3.1.6 Software

- Streampix 3.2.1 (Norpix, Montreal, Quebec, Canada)
- Visual Fortran 6.6 (Compaq, Houston, TX),
- MATLAB 2011 with Image Processing, Image Acquisition, and Instrument Control toolboxes (Mathworks, Natick, MA)
- Videomach (Gromada)
- MathCad (Microsoft, Redmond, WA)
- WCIF ImageJ (Wright Cell Imaging Facility, Toronto, ON, Canada),
- Scion Image (Scion 38 Corporation, Frederick, MD)
- Draftsight (Dassault Systèmes, Velizy Villacoublay, France)
- Comsol Multiphysics (Comsol, Inc., Burlington, MA)
- Irfanview (Irfan Skiljan, Vienna, Austria)
- SigmaPlot (Systat Software Incorporated, San Jose, CA)

3.1.7 Miscellaneous

- index matching oil (n=1.515, Cargille, Cedar Grove, NJ), 68^{o} dovetail prism (Red Optronics, Mountain View, California)
- Nochromix (Godax Labs, Takoma Park, MD)
- 10 mm I.D. Viton o-rings (McMaster Carr, Robbinsville, NJ),
- vacuum grease (Dow Corning, Midland, MI)
- Loctite professional heavy duty epoxy (Henkel Consumer Adhesives, Avon, OH)

- 6” lens paper, Fisherbrand egg-shaped magnetic stir bars, Fisherbrand 100 mm × 15 mm polystyrene petri dishes, Fisherbrand 9” flint glass, non-sterile Pasteur pipettes, 1.5 mL mirocentrifuge tubes, specialty pipette tips, 11 cm x 21 cm Kimwipes, purple nitrile powder-free exam gloves (Fisher Scientific, Pittsburgh, PA)
- 4 in × 125 ft Parafilm (Bemis, Neenah, WI)
- 10 μL, 100 μL, 1000 μL micropipette (Eppendorf Research, Hamburg, Germany)
- 1 and 10 mL syringes (BD, Franklin Lakes, NJ)

3.2 Colloid and Slide Preparation

3.2.1 Microscope Slide for TIRM experiments

In order to ensure uniform surface chemistry, which ensures uniform polymer adsorption, all glass slides were cleaned using the same protocol. Slides were first sonicated in IPA for 30 minutes followed by sonication in acetone for 30 minutes to remove residue and debris from manufacturing and packaging. The slides were then soaked for a minimum of one hour in NOCHROMIX® so that all dangling silane groups fully bonded to hydrogen atoms. Finally, the slides are soaked in potassium hydroxide for 20 min so that all dangling groups were hydroxyl groups. The slides were rinsed thoroughly in deionized water and dried with nitrogen. The clean slides were set on lens paper in a closed petri dish to prevent dust from settling on the slides. The slides were allowed to sit for 30 minutes to ensure that any remaining moisture evaporated.

3.2.2 Microscope Slide Functionalization with Hydrophobic Substrate

All experiments reported in this dissertation utilized polymer adsorption to hydrophobic surfaces. Polystyrene (PS) was used to hydrophobize the clean microscope slides. Approximately 192,000 Mw PS pellets were dissolved in toluene at a 1:100 ratio using sonication for approximately one hour. When the polystyrene was fully dissolved, approximately 1mL of the polystyrene/toluene solution was pipetted onto the slide using a glass Pasteur pipette. The slide was spin-coated for 40 seconds at 1,000 rpm to create a uniform polystyrene/toluene layer. The slides were then allowed to sit on lens paper in a closed petri dish for 30 minutes until the toluene evaporated leaving a uniform, hydrophobic polystyrene layer.

3.2.3 Building Experimental Cells on Microscope Slides

For experiments conducted over Pluronic® or BSA-coated walls, Viton® o-rings coated in vacuum grease were mounted on the center of the slide to create a confined cell. More vacuum grease was spread in a thick, contiguous ring around the o-ring to prevent leaking upon deposition of the polymer solution, and later the colloidal probe solution, into the o-ring. After completion of polymer adsorption to the wall and addition of the colloidal probe dispersion to the cell, the confined cell was sealed using a coverslip, wiped clean with lens paper, that was gently pressed on to the o-ring. The excess vacuum grease on the o-ring caused the coverslip to stick and gently tapping the coverslip with tweezers prevented any gaps that could cause convection or leaks and destroy the experimental sample.

Experiments in which mucus was adsorbed to the wall required floating cells instead of confined cells. To build a floating cell, a black circle was drawn on the underside of the slide to show where the polymer solution would be deposited. If two cells were being made on one microscope slide, a strip of vacuum grease separated the cells. Only surface tension in the polymer solution and repulsion between the aqueous solution and the hydrophobic slide surface served to confine the solution to the area of the slide where it was deposited. After adsorption, the polymer solution was replaced with a colloidal probe dispersion. The sample was covered with a petri dish lid and the probes were allowed to settle to the slide surface for 5 minutes. A clean coverslip was then floated on top of the colloidal dispersion drop. The downward applied force from the coverslip and capillary forces between the aqueous solvent and the coverslip generally caused the drop to spread to the outer edges of the coverslip while surface tension in the aqueous solvent and repulsion between the dispersion and the hydrophobic slide surface prevented spreading of the dispersion beyond the edges of the microscope slide. Applying minimal downward pressure to the microscope slide, epoxy was deposited using a wooden stick applicator around the outer edges of the microscope slide to confine the experimental cell. If the dispersion did not spread to the edges of the microscope slide, the epoxy would be gently pushed under the slide, forcing air bubbles out of experimental cell. Aqueous solution extending beyond the edges of the coverslip frequently prevented epoxy from sticking and sealing the observation cell, rendering the sample unusable. The epoxy was allowed to dry for 10 minutes. The black circle drawn on the bottom of the slide prior to polymer adsorption served as a reference during experiments for where the polymer had been adsorbed for the full adsorption time, since the dispersion spread over a larger area in the process of building the floating cell.

3.2.4 Coverslip Functionalization with Polymer Layer

Robust levitation of colloidal particles requires functionalization with a dense polymer brush layer. Since all polymer functionalization reported in this dissertation was conducted in aqueous colloidal dispersion, hydrophobized silica particles

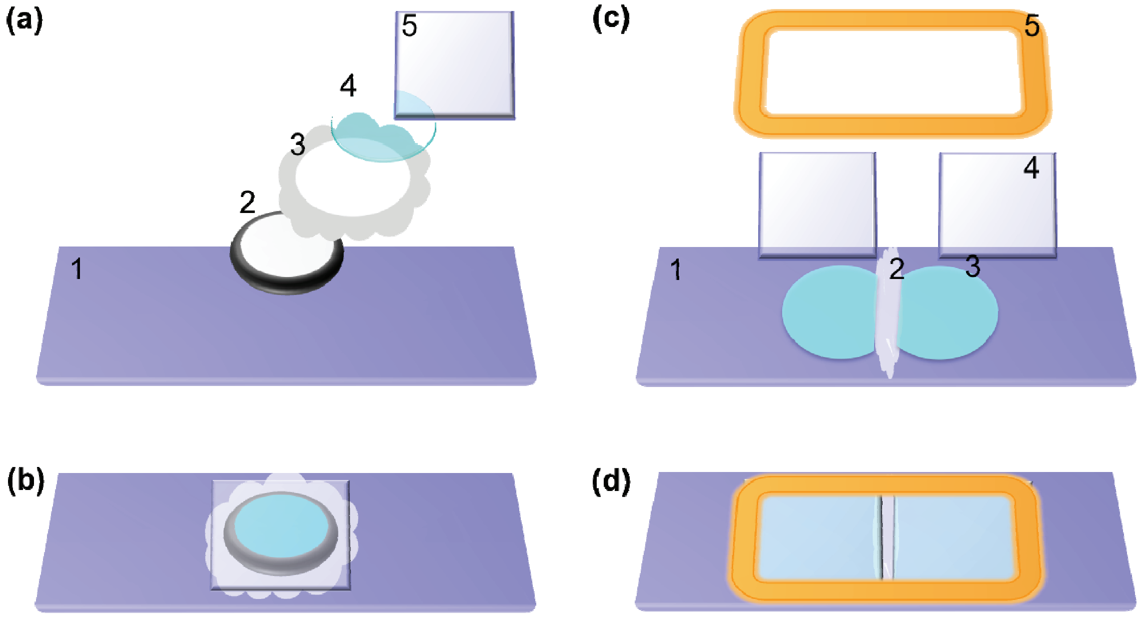

Figure 1.3 Schematic of the step-by-step assembly of an experimental cell and of assembled cells. (a) Confined cells are assembled in five steps. First, (a.1) a glass slide is cleaned and coated with polystyrene. Second, (a.2) an o-ring is coated in vacuum grease and placed in the center of the glass slide. Third, (a.3) the o-ring is surrounded with vacuum grease to prevent leaking. Fourth, (a.4) the o-ring is filled with sample. Fifth (a.5) after adsorbing polymer and depositing sample into the o-ring, the confined cell is sealed with a clean coverslip. (b) Shows a fully assembled confined experimental cell. (c) Floating cells are assembled in five steps. First, (c.1) as with the confined cell, a glass slide is cleaned and coated with polystyrene. Second, (c.2) a strip of vacuum grease is laid down in the middle of the slide. Third, (c.3) sample is deposited on either side of the vacuum grease. Fourth, (a.4) after the polymer is fully adsorbed and the sample has been deposited onto the slide, the cleaned coverslips are floated on top of the liquid with one edge bounded by the vacuum grease. Fifth (a.5) both floating cells are fully sealed with epoxy. (d) Shows 2 fully assembled floating experimental cells.

generally facilitated more rapid and more dense brush growth due to attraction between hydrophobic regions of the polymer or protein and the hydrophobic 1-octadecanol particle coating than hydrophilic particles. For TIRM experiments between a Pluronic®-coated wall and Pluronic®-coated colloidal particles, nominal 2.34 um particles coated with poly(ethylene oxide)-poly(propylene oxide)-poly(ethylene oxide) (PEO-PPO-PEO, F108) were used as colloidal probes. The triblock copolymer with molecular weights of

5400/3300/5400 g/mol adsorbed to the probes *via* the middle, hydrophobic PPO block, leaving the flanking, hydrophilic PEO blocks extending into the aqueous solution. Upon initial adsorption, the PEO blocks extend away from the colloid surface in a random walk configuration, lending to the description of the polymer as having a 'mushroom conformation'. Over time, as the polymer adsorption density increases, the PEO polymers, being extremely soluble in aqueous solution, extend away from the colloid surface so as to be completely coated by the good solvent, lending to its description as having a 'brush conformation'.

Pluronic® dissolved in DI water at 2mg/mL was filtered through a 0.2 um filter and 200 μL was deposited in a mounted o-ring mounted. The sample was covered and allowed to sit for 4 hours, allowing the Pluronic® to adsorb in a uniform, dense layer with bottle-brush conformation. Excess Pluronic® solution was removed from the o-ring, taking care not to scratch or dry out the adsorbed Pluronic® layer. The liquid was immediately replaced with NaCl solution and gently swished with a micropipette. The NaCl solution was removed, replaced and swished three times to make sure that all excess Pluronic® was removed from the solution in the cell.

BSA was adsorbed to hydrophobic slides using nearly the same procedure as for Pluronic®. 200 μL of a 1 mg/mL BSA solution was deposited in the cell and allowed to adsorb overnight to form a uniform, dense layer. Excess BSA was then rinsed from the solution in the experimental cell using the same rinsing procedure as was used for Pluronic®. Intrapolymer interactions between hydrophobic and hydrophilic regions and between positively and negatively charged regions make the exact conformation of the BSA polymer throughout the adsorption more difficult to precisely describe than that of Pluronic®. In some experiments, BSA has been shown to have an ellipsoid conformation while others show it to have a heart shape conformation. BSA is predicted to lay down against the colloid surface in low density adsorption and stand along its major axis in high density adsorption. BSA density plateaus at its maximum density after an adsorption time of approximately 12 hours.

Mucin solutions were prepared by dissolving under sonication 2.5 mg/mL BSM in a sodium azide, phosphate buffer, NaCl solution. This concentration was chosen as it was the maximum solubility for the BSM sample used. Different BSM samples, even purchased from the same supplier, were found to have different solubilities. After the solution was prepared, 200 μL of BSM solution were deposited into the o-ring and the sample was allowed to sit in a closed petri dish for 3 hours. The polymer solution was replaced with NaCl solution and excess BSM eliminated from solution using the same pipette techniques as was used for Pluronic® and BSA.

3.2.5 Hydrophobic Functionalization of Silica Colloidal Probes

TIRM measurements of virus-mimicking colloidal probes utilized nominal 1.59 μm, 2.34 μm and 3.1 μm diameter SiO_2 particles made hydrophobic through functionalization by 1-octadecanol using a literature method.[89] The colloidal particles, suspended in DI water, were centrifuged at 5,000 rpm for 90 s, the supernatant was removed, and the particles were resuspended in 200-proof anhydrous ethanol using sonication. Centrifugation and resuspension was repeated 8-10 times to ensure that all water had been eliminated from the colloidal dispersion and replaced with anhydrous ethanol. Residual water can lead to bridging and/or aggregation during the functionalization process.

The colloidal dispersion was centrifuged once more, the supernatant was removed, and the dispersion was transferred to a round bottom flask. 1 mL of a 1 mg/mL solution of 1-octadecanol and anhydrous ethanol was also added to the flask and the flask was sealed with a rubber stopper. The dispersion was continuously stirred and maintained at 50° C in a nitrogen atmosphere until the 1-octadeconal was fully dissolved. Upon dissolution, the reaction temperature was increased to 100° C. The temperature and nitrogen environment were maintained throughout the three hour reaction.

After three hours the sealed flask was submerged in a cold water bath and cooled to room temperature, at which point the colloidal dispersion crystallized. To recover the 1-octadeconal coated SiO_2 colloids, the reaction mixture was dispersed in chloroform. Excess 1-octadecanol was removed through the same centrifugation/resuspension procedure that was used to remove water from the initial dispersion. The colloidal dispersion was centrifuged at 5,000 rpm for 90 s and resuspended under sonication in chloroform five times. This centrifugation/resuspension procedure was then repeated five times more replacing chloroform with anhydrous ethanol. After completion of the final resuspension, the hydrophobically functionalized SiO_2 can be stored at 2-8° C and used at any time for up to one month.

3.2.6 Polymer Functionalization of Hydrophobic Silica Colloidal Probes for TIRM

As mentioned previously, a dense polymer brush was required on both the wall and on the colloidal particle in order to induce robust levitation. The same solutions used for polymer adsorption to the wall were used for adsorption to the colloidal particles. For Pluronic® adsorption, a 2.5 mg/mL Pluronic® solution prepared. At the same time, a 0.3-1 mL vial of previously prepared 1-octadecanol coated SiO_2 particles were sonicated to form a uniform dispersion. After sonicating for approximately 10 min, the colloidal dispersion was set-aside for approximately five minutes so that irregular SiO_2 particles could separate from the bulk *via* differences in sedimentation rate. 10-20 μL of the colloidal dispersion, depending on its concentration, were extracted from the center of the centrifuge tube and added to the Pluronic® solution. The new colloidal dispersion in Pluronic® solution was parafilmed and sonicated for approximately 10 min to uniformly disperse the colloids. The colloid-Pluronic® dispersion was then set on a rotating mixer for a minimum of 4 hr so that the Pluronic® could fully adsorb to the hydrophobic colloids. The stock colloidal dispersion was parafilmed and returned to the refrigerator for later use.

BSA and BSM coated colloidal particles were prepared using much the same procedure as was used for the Pluronic® coated colloidal particles. For BSA coated particles, a 1 mg/mL BSA solution was prepared. 1-octadecanol coated particles were added to the BSA solution and BSA was allowed to adsorb to the particles for 12 hrs. For mucus coated particles, BSM was dissolved in a phosphate, NaN_3, NaCl solution to make a 2.5 mg/mL stock BSM solution. Hydrophobic colloidal particles were added to 1 mL of the BSM solution, sonicated briefly, and set on a rotating shaker for 3 hr for adsorption.

After polymer-colloid adsorption, the colloidal dispersion was sonicated for approximately 10 min to uniformly suspend the colloids. The dispersion was then allowed to sit for approximately 5 min so that irregular particles would separate from the bulk *via* different rates of sedimentation. 100 μL of the polymer-colloidal dispersion was then extracted from the middle of the centrifuge tube and added to 1 mL of 0.15 M NaCl solution.

Silica colloids did not require a hydrophobic coating in order to adsorb a dense polyelectrolyte layer, since glass carries a negative charge. However, 1-octadecanol coated silica colloids were used for consistency. Large polyelectrolyte polymers that were unlikely to participate on additional chemical reactions were selected. Due to the negative charge of the colloidal particles, positively charged polyelectrolyte, polyallylhydrochloride (PAH), was adsorbed as the first polyelectrolyte layer. For 2-layer experiments, polystyrene sulfonate (PSS), was used as a negative polyelectrolyte and adsorbed over the PAH.

Various adsorption conditions, including time, concentration, ionic strength, and pH, were explored in order to form 1) the thickest single or multi-layer and 2) multi-layers that carried coexisting positive and negative charges in the outer layer. A dense PAH or PSS outer layer would carry a large positive or large negative zeta potential, respectively. PAH adsorption yielding a strongly positive zeta potential followed by an approximately zero zeta potential due to PSS adsorption was presumed to indicate the coexistance of positive and negative charges on the outer polymer layer.

After much exploration, an adsorption environment of 0.5M NaCl and neutral pH was selected. Between 1 and 26 mg PAH was dissolved in 1 mL of 0.5 M NaCl. 1-5 μL of 1-octadecanol colloidal probe dispersion was added to the polyelectrolyte solution. A low colloid concentration was used to prevent aggregation or bridging between particles. The polymer/colloid dispersion was parafilmed, sonicated for 30 s and put on the rotating shaker for 10 or 20 min for adsorption. At the precise time point, the dispersion was removed from the shaker and centrifuged for 5 min at 10,000 rpm. The supernatant was replaced with 0.5M NaCl solution and the pellet was resuspended. Centrifugation and resuspension in NaCl solution was repeated 8 times to eliminate excess PAH from solution. For experiments on colloidal probes with a single, positive polyelectrolyte layer, 0.15 M NaCl was used for the final 3 resuspension. For multilayer polyelectrolyte experiments, 0.5 M NaCl was used for every resuspension. After the final resuspension, the dispersion was centrifuged one final time and the supernatant was replaced with a polyelectrolyte solution of 0.5-2 mg/mL PSS dissolved in 0.5 M NaCl. The colloidal dispersion was parafilmed, sonicated for approximately 30 s and placed on the shaker for adsorption. After precisely 10 min or 20 min, the dispersion was centrifuged and resuspended in NaCl solution as described above to clean excess polyelectrolyte from the dispersion. After 8 centrifugations and resuspensions, particle preparation was complete. Since a low initial concentration was used, the dispersion did not undergo a second dilution.

3.2.7 TIRM Sample Preparation

Particle-colloid dispersion was used within 1 day of adding NaCl, as high salt concentration decreases the Debye length of the solution and can cause particle aggregation. The colloidal dispersion was sonicated and allowed to sediment for approximately 5 minutes. During the final sedimentation, attention was turned back to the sample cells on the microscope slide. Using the technique described above, excess polymer was rinsed from the solution in the experimental cell. Immediately following the final rinse and solution extraction, the liquid in the cell was replaced with 100 μL of the final colloidal dispersion for confined cells and 300 μL of the final colloidal dispersion for floating cells. The microscope slide was kept in a closed petri dish for 5 min while the colloidal particles sedimented to the surface of the slide. A coverslip was then laid overtop the experimental cell and the cell was sealed as described above.

3.2.8 Polymer Functionalization of Polystyrene Colloidal Probes for Microfluidics

Fluorescent and nonfluorescent carboxylated polystyrene colloids of varying diameters were used for measuring diffusion in microfluidic devices. For Pluronic® coated fluorescent polystyrene particles, a 2.5 mg/mL solution of Pluronic® and 0.15 M NaCl was prepared. 2 mL of Pluronic® solution was deposited in a 3.5 mL centrifuge tube and 0.5 mL of polystyrene particles were added. 5 M NaCl was then added to the dispersion to return the ionic strength to 0.15 M. To prevent diffusion effects from gradients in polymer concentration or ionic strength, the same Pluronic® and NaCl stock solutions were used to prepare the solution of nonfluorescent solution or particle dispersion into which the fluorescent particles diffused. For gradient diffusion experiments, the solution included 0.5 mL DI in place of the particle dispersion. For self-diffusion experiments, nonfluorescent particles of equal diameter were used in the place of fluorescent particles. The centrifuge tube was placed on a rotating shaker for 4 hr so that the Pluronic® could fully adsorb to the particles. The dispersion was used in its current state without further dilution or purification.

The above procedure was followed for all polymer or protein coated polystyrene particles, only altering the polymer or protein and the adsorption concentration and time. The BSA stock solution was mixed at 1.5 mg/mL BSA and adsorbed to the particles for 12 hr. The BSM solution was mixed at 2.5 mg/mL BSM in 10 mM phosphate buffer/0.02% NaN_3, 0.15M NaCl solution and adsorbed to the particles for 3 hr. After adsorption all dispersions were used without further dilution or purification.

3.3 Substrate and Polymer Characterization

3.3.1 Dynamic Light Scattering

Dynamic light scattering (DLS) was used to measure the hydrodynamic radius of colloidal particles. While DLS lacks the precision to accurately measure the layer thicknesses or exact polymer hydrodynamic radius, it was used to indicate if particles were coated and stable or if the particles had aggregated. Measurements were limited to polystyrene particles as silica particles sedimented too rapidly to take accurate readings.

All DLS samples were prepared in high-performance liquid chromatography (HPLC) grade water or in DI water filtered twice through a 0.02 μm filter. The water was used to rinse a Pasteur pipette and a cuvette. Approximately 1 mL of water was then transferred, using the Pasteur pipette, into the cuvette. 1-10 μL drop of sample, depending on the concentration, was transferred to the cuvette. Size measurements were then performed by a ZEN3600 ZetaSizer Nano.

3.3.2 Zeta Potential

The ZEN3600 ZetaSizer Nano was also used to measure the electrokinetic potential of the colloidal dispersions. Cuvettes for taking the zeta potential were rinsed with twice filtered DI water or with HPLC grade water. The colloidal sample was suspended in DI water or in a NaCl solution, then injected into the microcuvette, taking care that there was no air in the sample.

3.4 Microfabrication

3.4.1 Silicon Masters

Microfluidic devices were molded using silicon wafers carrying a photoresist pattern. The pattern was designed using Draftsight and printed on a photomask.

Generally, the pattern included 6 channels on each transparency. The pattern was transferred to the silicon wafer in a clean room.

The silicon wafers were first rinsed with acetone and IPA to remove any residue. They were then dried with N_2 and placed on a hotplate at 200° C for 10 min to remove all remaining moisture. The wafers were next plasma etched. They were loaded into a vacuum chamber. After venting the chamber, Oxygen gas was flowed into the chamber to maintain 0.475 Torr of pressure inside the chamber. The oxygen pressure was maintained for 2-3 min to ensure that only oxygen was present in the chamber in any significant concentration. The voltage in the chamber was then switched on and set to 400 mV for precisely 5 min.

After plasma etching, approximately 6 mL of SU-8 3010 photoresist was deposited on the wafer via a Pasteur pipette and a spin coater was used to distribute the photoresist in a uniform layer over the entire wafer. The photoresist was spin coated at 2000 rpm for 30 s with an acceleration of 300 rpm/sec. The wafers with photoresist were then soft baked for 6 min at 95 ° C.

The photoresist was exposed using a mask aligner. The wafers were individually loaded and processed. The transparency was placed over top of the photoresist, which was then exposed at 130 mJ/cm^2. The exposed silicon wafers were then baked again for 3 min at 95 ° C and then developed for approximately 6 minutes, until the developer solution on top of the wafer appeared clear and not milky. Wafers underwent a final hard bake for 30 min at 200 ° C to harden the photoresist against erosion.

3.4.2 Building Microfluidic Devices

All microfluidic experiments were performed in polydimethylsiloxane (PDMS) devices. PDMS was mixed in a 10:1 ratio of elastomer to curing agent. The mixture was stirred vigorously until bubbles were visible throughout to indicate thorough incorporation of the curing agent. The mixture was then completely degassed in a vacuum chamber. When no air bubbles remained, the PDMS solution was gently poured over the silicon master to a depth of just under 0.5 cm. The masters and PDMS solution were baked at 70° C, until the PDMS was completely hardened. Baked PDMS had a stiffness and appearance comparable to clear rubber.

The PDMS was cut and pealed from the master in a clean room to prevent dust from settling on the PDMS surface. Pealing in the direction parallel to the longest lines in the device yielded the cleanest channels and prevented the photoresist from separating from the wafer along with the PDMS. The PDMS slab was laid on a McMaster cutting sheet with the patterned side up. Throughout the cutting and sealing processes, great care was taken never to touch the patterned side of the PDMS. Touching the PDMS could make the channels dirty and/or prevent the device from bonding strongly enough to withstand the pressure of the microfluidic experiments. A razor blade was used to cut out the individual channels from the PDMS slab and to cut the channels to the proper shape and size. Holes were then punched at the inlet and outlet ports using a 0.75 mm inner diameter Harris hole punch.

After cutting the PDMS devices, they were moved to the plasma etch. The plasma etch would be used to bond each PDMS slab to a Gold Seal coverslip by cleaning and functionalizing the bonding surfaces of the glass and PDMS so that they would both be highly reactive. Prior to etching, each cover slip was gently and quickly cleaned with DI water and dried with nitrogen gas. The coverslips and PDMS were immediately loaded into the plasma etcher. Etching at too high a voltage or for too much time turns the PDMS surface to glass. As such, a more precise etching procedure was followed than for etching silicon. Once the devices were in the chamber, the vacuum was switched on until the pressure in the chamber reached 0.002 Torr. Oxygen gas was then allowed to flow into the chamber and adjusted until the pressure inside the chamber reached 0.3 to 0.4 Torr. The oxygen pressure was maintained for 5-10 min to ensure that only oxygen was present in the chamber in any significant concentration. The voltage in the chamber was then switched on and set between 30 and 35 mV for precisely 45 s. The applied voltage ionizes the oxygen so that high-energy oxygen bombards the exposed surfaces. Through this process, the bonding PDMS and coverslip surfaces were uniformly functionalized and rendered highly reactive.

The surfaces were etched for 45 s after which the voltage was turned off and the chamber vented. The etched PDMS surface was gently laid on the etched glass surface. The devices generally bonded rapidly and spontaneously. Where bonding did not take place immediately, the PDMS was gently tapped with tweezers. Bonded devices were then placed in an oven for approximately 10 min at 70° C to ensure complete bonding.

3.5 Constant Pressure Microfluidic Experiments

3.5.1 Constant Pressure Apparatus

Diffusion experiments were conducted by injecting a fluorescent liquid into one inlet port and a nonflorescent liquid into another inlet port so that the two liquids flowed parallel to each other at equal pressure, creating an interface between the liquids at the center of the channel. Injection *via* syringe pump caused fluctuations in the interface due to gear rotation. A constant pressure apparatus was constructed to eliminate fluctuations. To build the constant pressure apparatus, a regulator and pressure gauge were connected to the house air system. Polyurethane tubing directed air from the first regulator into a manifold with one inlet and multiple outlets. Using on/off switches on the manifold, a number of “channels” could be connected to the air-source and turned on or off as needed throughout the experiment. Red polyurethane tubing was used for the fluorescent channel while blue polyurethane tubing was used for the nonfluorescent channel. In this way, when the air pressure for one channel needed to be adjusted or turned off, that channel’s regulator and switch could be easily identified. Red or blue tubing directed air from the manifold to a second, low pressure, high precision regulator and gauge. From the second regulator and pressure gauge, the air was directed through a 0.02 μm filter to remove all particulates and oils present in the house gas. The air then entered a sealed 3.5 mL centrifuge tube whose only outlet was thin tubing. This tubing had one end submerged in the experimental solution and the other end injected directly into the microfluidic device. As air entered the centrifuge tube, liquid was pushed up through the thin tubing to release pressure. Once regulators were set to an experimental pressure, a constant pressure, and as a result, constant flow rate and interface position was maintained throughout the experiment.

3.5.2 Microfluidics and Fluorescence Microscopy

All microfluidic experiments were conducted in the PDMS devices previously described. Prior to experimentation, a 10 mg/mL Pluronic® solution was injected into the channel. The Pluronic® solution was left for 1 hr to coat the PDMS and prevent adsorption of the experimental sample to the PDMS walls. While the 10 mg/mL solution needed to be flushed prior to experimentation to prevent the high concentration of polymer from effecting the experiment, flushing with a solution completely lacking Pluronic® allowed the Pluronic® coating the PDMS to desorb. If the Pluronic® desorbed from the PDMS, the experimental sample could once again adhere to the PDMS channel. The 10 mg/mL solution was flushed from the channel by a 2.5 mg/mL Pluronic® solution; low enough to make experimental effects unlikely and high enough to prevent desorption. The 2.5 mg/mL Pluronic® solution was pumped into the channel at approximately 0.8 psi for approximately 1 hr.

Carefully, to prevent any air from entering the channel, the injection solution was changed from the flushing solution to the two experimental sample suspensions. Each sample was injected into 1 of the 2 entry ports (Fig. 3.2a) at a pressure of approximately 0.5 psi. The pressure of each injection tube was adjusted so that the interface between the fluorescent and the non-fluorescent sample rested in the middle of the channel. The pressures were then slowly decreased so that the interface remained in the middle of the channel until significant diffusion of the fluorescent sample across the channel was clearly visible and gradual over the length of the channel. Final experimental pressures fell between 0.2 psi and 0.4 psi. Tubing was inserted into the outlet port for measuring the experimental flow rate. The flow rate was found by simply marking the outlet tubing at the beginning and end of the experiment. A stopwatch was used to time the experiment. A simple equation was used to calculate the volumetric flow rate.

The first reading was taken with the left side of the viewing window exactly aligned with the point where the two input channels joined (Fig. 3.2c). Readings were

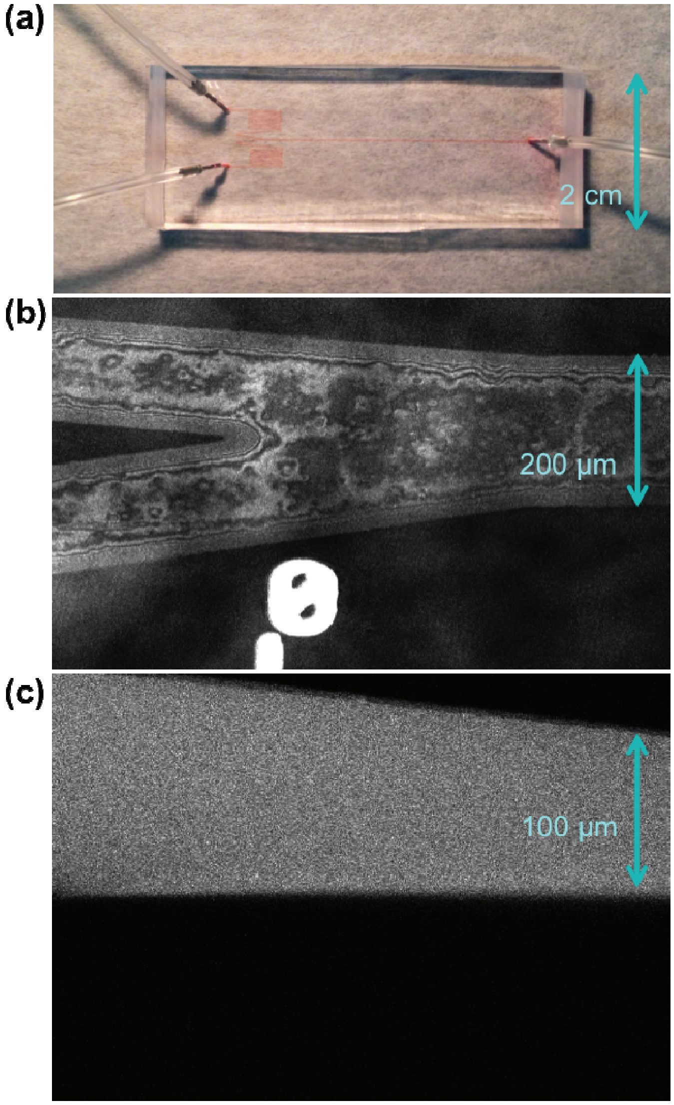

Figure 3.2 Images of the microfluidic device used for gradient and self diffusion experiments. (a) Image of the PDMS device without magnification with tubing inserted into the inlets and the outlet. Red liquid injected into the channel makes the entire channel visible. A series of curves, visible at each inlet, increases the resistance within the channel, facilitating slower flow rates. (b) 10 × image taken *via* confcal microscopy of the Y-junction where the two entrance channels join. A ruler microfabricated into the device, visible below the channel, indicates the distance down the channel in centimeters. (c) 24 × experimental image taken *via* confcal fluorescence microscopy of the Y-junction where the two entrance channels join. The sharp interface where the fluorescent solution initially meets the nonfluorescent solution is clearly visible. A small amount diffusion of fluorescence across the interface is visible farther down the channel, on the right.

then taken every 0.5 cm down the channel beginning at 0 cm (Fig. 3.2b) and ending at 3 cm. Each device had a ruler fabricated into the PDMS just below the channel with a tick mark every 0.1 cm and a tick label every 0.5 cm. The clearly visible ruler made distance measurements easy and precise. Averaging the intensity over a 10 pixel wide box and 250 frames was found to minimize noise without significantly increasingly analysis time.

3.6 Microscopy

3.6.1 Total Internal Reflection Microscopy

Total internal Reflection Microscopy was used to measure the interaction potentials between polymer-coated colloidal probes the polymer-coated wall that the probes interrogated, as shown in Figure 3.3. The sample was optically coupled to a 68° dovetail prism using index matching oil (n=1.518). After leveling the microscope stage using its three point leveling system, the prism and sample were placed on the stage. Using a system of mirrors and a focusing lens, a 15 mW 632.8 nm Helium-Neon laser was directed through the prism so that it hit the glass liquid interface of the sample at the angle of total internal reflection. Total internal reflection causes an evanescent wave to form over the reflecting surface (in this case the liquid in the sample cell). The laser angle was optimized to produce an evanescent wave with maximum intensity. The intensity of the evanescent wave produced in these experiments exponentially decayed as a function of height over the surface with a decay length of β^{-1}=113.67 nm. Colloidal particles diffusing over the wall scattered light in the evanescent wave with an intensity inversely related to the height of the particle over the surface according to the equation: $I(h)=I_0\exp(-\beta h)$. Since the evanescent wave intensity decayed exponentially, small height excursions caused large differences in intensity.

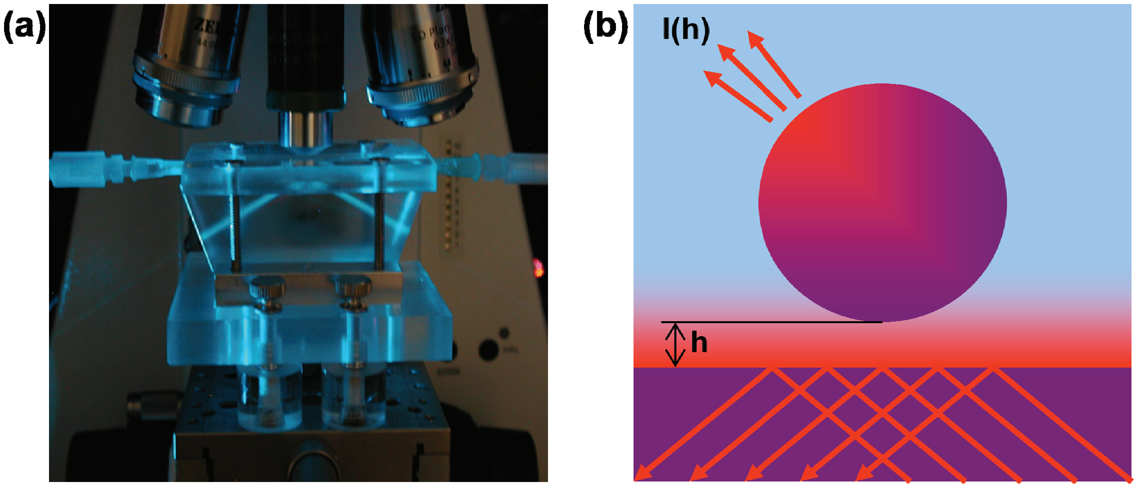

Figure 3.3 Image of (a) an inverted microscope with a mounted prism and experimental cell. The laser can be seen passing through the prism and reflecting when it encounters the experimental sample. The schematic (b) shows the laser hit the wall at the critical angle to totally internally reflect, creating an evanescent wave over the slide. The particle scatters light with intensity dependent on the particle's height in the evanescent wave, as shown in the schematic.

Images were taken using a 12-bit CCD camera (ORCA-ER, Hamamatsu) operated in 4-binning mode on an Axio Imager A1m upright optical microscope with an Achroplan 40× (NA=0.65) objective to yield 27.78 frames/s, 607 nm/pixel, and a 336 pixel × 256 pixel image. For each experimental measurement, 30,000 image frames were collected to ensure adequate statistics using StreamPix software. The resulting multi-page TIFF stack was then analyzed on a PC using a series of image analysis algorithms coded in FORTRAN.

3.6.2 Confocal Fluorescence Microscopy

Confocal scanning laser microscopy (CSLM) was used to collect fluorescence intensity data for diffusion experiments. The confocal uses a pinhole to filter out ambient light, significantly increasing spatial resolution. The confocal settings were adjusted to optimize resolution with fluorescence intensity. For example, increasing the laser intensity increased light so that the images appeared less pixelated, but resolution decreased so that the curves produced analytically were less sharp.

Images were taken using a 12-bit CCD camera on a Axiovert 200M with LSM 5 confocal laser scanning microscope with a 10× objective and 2.4× zoom to yield a frame rate of 0.64 fps and 1.15 μm/pixel. Confocal experiments employed a 10-350 mW 488 nm (blue) laser to excite fluorescent colloids. Image analysis algorithms coded in FORTRAN were used to calculate the average intensity across the channel over 250 frames.

3.7 Computational Analysis

3.7.1 Analysis of Fluorescence Diffusion

The high resolution gained from confocal microscopy yielded diffusion measurements that were precise, yet difficult to interpret and fit to a theoretical model due to large peaks and troughs between bright and dark pixels. For this reason a computer algorithm was written in FORTRAN that averaged the intensity over a 10 pixel slice and over 250 frames. The resulting graphs were significantly smoother and could be better fit to a theoretical model without adding significant complication in data processing.

The fluorescence intensity was measured across the channel at the top, middle, and bottom of every image and averaged over a 10 pixel wide strip. Those three intensities were each averaged over a 250 image sequence. The raw intensity was plotted with respect to pixels across the image and aligned with the channel edges according to guidelines drawn using the original image. The integral of the intensity over the entire curve was taken 20-30 pixels from both walls to eliminate edge affects from the analysis. The maximum and minimum intensities were determined using the intensity plot as a guideline. Since the interface was in the center of the channel, the ratio of the area under the intensity curve to the area in the box bounded by the maximum and minimum intensities and the channel edges was 1:2. This ratio was used to precisely tune the maximum and minimum intensities and the channel edge locations. A target drawn on the graph indicating the interface at the midpoint of the channel and the average intensity was used to indicate alignment of the interface in relation to the center of the channel. The target consistently fell precisely on the curve.

Diffusion of the fluorescent material across the channel means that after the initial channel junction, the concentration was not as high or as low as the maximum or minimum intensities, respectively, at any point across the channel. The difference between the image intensity minimum and maximum farther down the channel and the absolute intensity minimum and maximum was determined using the difference between intensity minimum inside the channel and the intensity minimum outside of the channel. Due to conservation of mass, the same amount of fluorescent material had to be present in the channel at every point down the channel. As a result, the ratio between the overall intensity at any point down the channel, found by taking the integral under the curve, and the overall intensity at the entrance of the channel could be used to calibrate image intensity at every point down the channel, thus eliminating intensity differences due to microscope settings or photobleaching at the edge of the channel. After calibrating the graphs, the curve was replotted as a function of concentration related to the absolute maximum and minimum concentrations.

4. DIRECT MEASUREMENTS OF DRUG PARTICLE-MUCUS INTERACTIONS

Total Internal Reflection Microscopy combined with Bayesian Inference Analysis was used to measure interactions between virus-mimicking drug delivery particles and mucus brush layers. The particles were coated with polyethelyne glycol or with charge-carrying polymer layers. Polyelectrolytes in mono- or multi-layers and bovine serum albumin were used for charged drug delivery particle coatings. Total Internal Reflection Microscopy was used to take measurements on the energetic *kT*-scale. Novel analytical theory was developed to characterize the conformation of the layers and define the steric interactions between polymer brushes. This paper gives new insight into the thermodynamic and hydrodynamic interaction between virus-mimicking drug delivery particles and adsorbed mucus layers. Protein layers with small size-scale charge separation were found to have the most potential as mucoso-penetrating drug delivery particles.

4.1 Introduction

Mucus is widely studied as a model polymer, gel, porous media, and as the primary barrier against pulmonary drug delivery.[2-6] Mucus secretions create a tenacious yet porous gel that protects the intestinal, respiratory, and reproductive tracts. Pore size and particle-mucus interactions have been widely accepted as the limiting parameters for diffusion through mucus.[11-13,19,20] Some proteins and protein-coated viruses rapidly penetrate mucus while other proteins and viruses encapsulated in a phospholipid layer cannot penetrate the mucosal layer. Mucus is primarily composed of mucins, which generate its characteristic thixotropic, chemically adhesive gel structure. Mucins consist of hydrophobic protein regions connected by hydrophilic polysaccharide chains with net negative charge.[1,3,4,21-24] Electrostatic repulsion and the physical mucus barrier prevents many pathogens and drug delivery particles (DDPs) from partitioning into the mucus layer while hydrophobic, electrostatic, and mechanical interactions cause adhesion to other penetrating vectors.[25] A better understanding of physical as well as hydrodynamic interactions between potential drug delivery particles (DDPs) and mucin layers is essential to the development of viable pulmonary drug delivery vectors[11] for treating pulmonary disorders[13,90] as well as the utilizing the lungs as a surface for drug delivery for non-pulmonary disorders.[10,11,91]

Experimental measurements of nanoparticle diffusion through mucus are limited. Particle tracking experiments have shown that nanoparticle size affects diffusion rate. Particles densely coated low molecular-weight polyethelyne glycol (PEG) have been shown to diffuse more rapidly than uncoated particles while particles coated with high molecular weight PEG stick to mucus.[11,47,91] Fluorescence Recovery After Photobleaching (FRAP)[11,13,92] and fluorescence migration have been used to measure bulk diffusion of nanoparticles and macromolecules through mucus. In general, previously used diffusion measurement techniques lack the scope to measure a statistically significant number of particles or specificity to elucidate individual interactions.

Measuring the conformation of surface adsorbed mucins is important for interpreting interactions between mucins and other macromolecules on a molecular level.[24,25,34] Quartz Crystal Microbalance and Surface Force Apparatus (SFA) have been used to measure the effect of adsorption conditions on mucin adhesion and on polymer and gel conformation.[34,38] SFA experiments have shown that at low density surface coverage mucins bridge between the opposing surfaces while at high density coverage mucins form sterically repulsive brush layers.[24,27,37,39] Atomic Force Microscopy (AFM) has been used to measure the interaction strength of mucoadhesive drug delivery vectors.[24] None of the techniques used to investigate mucus adsorption is capable of measuring hydrodynamics or dynamic interactions within the adsorbed mucin layer.[24] Total Internal Reflection Microscopy (TIRM) dynamically measures potentials between colloids and a surface with high statistical relevance.[73,85,93,94] Data collected using TIRM can give a rigorous description of the hydrodynamics and polymer physics of mucin polymer layers that does not yet exist.

In this paper, we report both thermodyamic and hydrodynamic interactions between polyelectrolyte multilayer, bovine serum albumin (BSA), and PEO copolymer physiadsorbed particles and mucin brush layer coated microscope slide surfaces with non-intrusive probes (Fig 1). PEO copolymer polyelectrolyte multilayers, and bovine serum albumin (BSA) coated colloidal probes mimic viruses known to rapidly penetrate mucus. Using TIRM, we directly measure *kT*-scale steric potential energy profiles and dynamic diffusivities of colloidal particles as a function of height levitated over a mucosal layer.[73,93] Standard Boltzmann probability analysis of long trajectories was utilized to obtain particle potential energy profiles and mean squared displacements. A universally applicable exponential equation set to Milner's equation for steric potentials of brush layers captured steric interactionpotentials and diffusivities of symmetric and asymmetric polymer brush layers. Measured particle trajectories were additionally analyzed using bayesian inference to measure colloidal conservative and dissipative

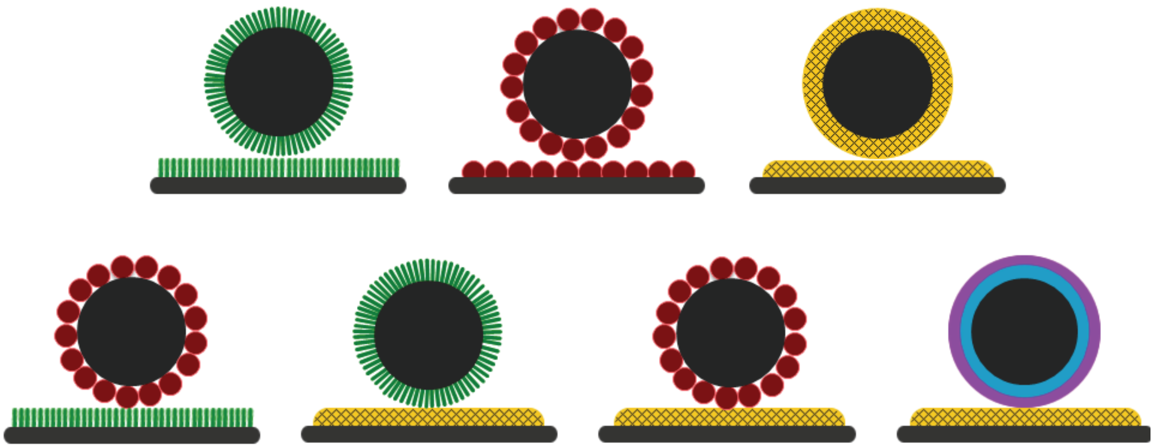

Figure 4.1 Schematics of a 2.34 μm diameter SiO_2 particle (grey circle) interacting with a flat glass microscope slide (grey), each with one of four surface functionalizations: pluronic (green rods), BSA (red circles), mucus (yellow crosshatch), positive (blue ring) and negative (pink ring) polyelectrolyte.

forces from these ensemble colloidal particle probe excursions normal to the underlying substrate. Our results show agreement with our Boltzmann probability analysis using our exponential equation for symmetric and asymmetric steric particle potential energy and diffusivity profiles. Diffusivity profiles followed known hydrodynamic contributions that include the surface separation dependence and the effect of both adsorbed polymer or charge-carrying layers and adsorbed gel layers in solution. Particle potential energy and diffusivity profiles indicated that mucins form thick, highly compressible, hydrodynamically permeable layers. Our results demonstrate that steric, electrostatic, and hydrodynamic effects determine interactions between mucus and charge-carrying proteins used as viral mimics for enhancing drug delivery through mucus.[10,11,13,19]

4.2 Theory

4.2.1 Net Interaction Potential

Theoretical models of the net particle-wall potential energy of particles in physiological ionic strength media, $u(h)$, can be computed from the superposition of contributing potentials as,

$$u(h) = u_G(h) + u_V(h) + u_S(h) + u_H(h) \tag{4.1}$$

Where *h* is surface-surface separation of the particle and wall.

4.2.2Gravitational Potential

The gravitational potential energy of each particle depends on its height, *h*, of the particle above the wall, multiplied by its buoyant weight, *G*, as given by,

$$u_G(h) = Gh = mgh = \frac{4}{3}\pi a^3 \left(\rho_p - \rho_f\right) gh \tag{4.2}$$

where *m* is the buoyant mass, *g* is acceleration due to gravity, and ρ_p and ρ_f are the particle and fluid densities, respectively.

4.2.3 Van der Waals Potential

Van der Waals potentials, which can be represented over the separation and energy ranges of interest by a convenient power law expressions as,[73,74,95]

$$u_V(h) = -Aa\left(h + \delta_V\right)^{-p} \tag{4.3}$$

where *A* and *p* are obtained from fits to the exact results and δ_V is a surface roughness correction factor.

4.2.4 Steric Repulsion

The separation dependent repulsion between asymmetric macromolecular layers is given by,[29]

$$u_s(h) = 8a\Lambda_1^{\frac{\lambda_1}{\lambda_1+\lambda_2}}\Lambda_2^{\frac{\lambda_2}{\lambda_1+\lambda_2}}\left(\lambda_1 + \lambda_2\right)\exp\left(-\frac{\lambda_1}{\lambda_1 + \lambda_2}\right) \tag{4.4}$$

where $\Lambda_i = \Gamma_i f_{0,i}$ and $\lambda_i = \delta_{0,i}/\gamma_i$ (i = 1, 2), $\delta_{0,i}$ is the uncompressed thickness of layer *i,* and Γ_i and γ_i are dimensionless constants that can be adjusted to generalize Eq (4.4) to adsorbed macromolecular architectures with different decaying density profiles at theirperiphery. Balancing steric repulsive forces and gravitational force, the overnet potential is:

$$\frac{u(h)-u(h_m)}{k_BT}=\frac{G}{k_BT}\left[\frac{(\delta_{0,1}+\delta_{0,2})\left[\exp\left(\frac{-\gamma}{\delta_{0,1}+\delta_{0,2}}\right)\right](h-h_m)-1}{\gamma}+(h-h_m)\right] \tag{4.5}$$

4.2.5 Tether Potential

A number of macromolecular tethers, *N*, with small extensions of different lengths acting in parallel can be modeled as Hookean springs, with a potential given as,[29]

$$u_H(h)=\frac{4k_BT}{4P}h^2\sum_{i=1}^{N}L_{T,i}^{-1} \tag{4.6}$$

P is the persistence length (which is half the Kuhn length, *b*; i.e., P=0.5b) and $L_{T,I}$ is the tether contour length, which for multiple tethers of identical length simplifies to,[29]

$$u_H(h)=\left(\frac{3Nk_BT}{4PL_T}\right)h^2 \tag{4.7}$$

4.2.6 Diffusivity Profiles

The separation dependent diffusion of colloids levitated over a flat wall, $D(h)$, can be modeled as,

$$D(h)=D_0 f(h) \tag{4.8}$$

Where D_0 is the Stokes-Einstein coefficient of an unbound spherical particle given by,

$$D_0=\frac{kT}{6\pi\eta a} \tag{4.9}$$

where η is the fluid medium viscosity and $f(h)$ is the hydrodynamic factor to particle diffusivity due to an increased drag of a particle moving close to a wall[96]

$$f(h)=\frac{6h^2+2ah}{6h^2+9ah+2a^2} \tag{4.10}$$

4.2.7 Net Potential Energy and Diffusivity Profiles from Measured Trajectories

The motion of a colloidal particle, normal to a wall, can be modeled by means of a one-dimensional Smoluchowski equation[97] (for fluid and particle negligible inertial forces),

$$\frac{\partial\rho(h,t)}{\partial t}=\frac{\partial}{\partial h}\left\{e^{-\frac{u(h)}{kT}}D(h)\frac{\partial}{\partial h}\left[e^{\frac{u(h)}{kT}}\rho(h,t)\right]\right\} \tag{4.11}$$

where $\rho(h,t)$ is the probability density of finding the particle at height, h, at time, t.

4.3 Materials & Methods

4.3.1 Materials

Nominal 0.97 μm, 2.34 μm, and 3.13 μm and diameter SiO_2 colloids (Bangs Laboratories, Fishers, IN) were modified with 1-octadecanol (Sigma-Aldrich Company, St. Louis, MO) using a literature method.[98] Glass microscope slides (Fisher Scientific, Pittsburgh, PA) were sonicated in ethanol (Fisher Scientific, Pittsburgh, PA) for 30 min, sonicated in acetone (Fisher Scientific, Pittsburgh, PA) for 30 min, immersed in Nochromix (Godax Labs, Takoma Park, MD) for 1 hr, soaked in 0.1 M KOH (Fisher Scientific, Pittsburgh, PA) for 20 min, washed with DI water, dried with nitrogen, and allowed to sit for 30 min to ensure any remaining moisture evaporated. The microscope slides were spin coated (Laurell Technologies Corporation, North Wales, PA) with polystyrene (Sigma-Aldrich Company, St. Louis, MO) prior to each experiment.

PEO-poly(propylene oxide)-PEO triblock copolymer (F108 Pluronic, BASF, Wyandotte, MI) with segment molecular weights of 5400/3300/5400 g/mol, BSA (Sigma Aldrich, St. Louis, MO), or polyelectrolytes were adsorbed to colloid surfaces as steric stabilizers. The copolymer was dissolved in DI water at 1000 ppm[99] and then adsorbed to the colloidal particles for a minimum of 6 hr. BSA was dissolved in 150 mM NaCl at 1 mg/mL and adsorbed to the hydrophobic SiO_2 colloids for a minimum of 12 hr. Positively or negatively charged polyelectrolytes were dissolved in 500 mM NaCl at varying concentrations and adsorbed for 10 min to 20 min.Polyallylhydrochloride (PAH, Sigma Aldrich, St. Louis, MO) was used as the positively charged polyelectrolyte and was adsorbed directly to the hydrophobic SiO_2. Polystyrene-4-sulfonate (Sigma Aldrich, St. Louis, MO) was used as the negatively charged polyelectrolyte and adsorbed over PAH. In each experiment, colloidal dispersions were washed with 50 mM NaCl two times followed by 150 mM NaCl three times to remove excess F108, BSA, or polyelectrolyte. Dispersions of SiO_2 and 150 mM NaCl in deionized water were prepared to yield ~1% SiO_2 interfacial area fractions for TIRM measurements.

Lyophilized mucus from bovine submaxiliary glands (Sigma Aldrich, St. Louis, MO) was dissolved at 1 mg/mL in 150 mM sodium chloride (NaCl, Acros Organics, Morris Plains, NJ), 10 mM phosphate buffer (Sigma Aldrich, St. Louis, MO), and 6 mM solution of sodium azide (NaN_3,Sigma Aldrich, St. Louis, MO). The mucosal solution was prepared at room temperature, stored at 4 °C, and used within 1 day of preparation to insure consistency in the mucus solution and prevent aggregation. Mucus was adsorbed for 2.5 hr to glass hydrophobized microscope slides and washed with one of the four colloidal dispersions.

4.3.2 Microscopy

Experiments were performed in sample cells consisting of 10mm ID Vinton o-rings (McMaster Carr, Robbinsville, NJ) sealed between the microscope slide and a glass coverslip (Corning, Corning, NY) for TIRM. A 12-bit CCD camera (ORCA-ER, Hamamatsu, Japan) operated in 4-binning mode on an upright optical microscope (Axio Imager A1m, Zeiss, Germany) with a 40× objective to yield 28 frame/s and 607 nm/pixel. TIRM experiments employed a 15mW 632.8nm Helium-Neon laser (Melles Griot, Carlsbad, CA) and a 68º dovetail prism (Red Optronics, Mountain View, California) to generate an evanescent wave decay length of β^{-1}=114nm. Image analysis algorithms coded in FORTRAN were used to track colloid lateral motion and to integrate the evanescent wave scattering intensity from each colloid.

4.3.3 Bayesian Inference Analysis

A "jump matrix" is constructed from TIRM measured particle trajectories by counting the number of jumps between height intervals after a jump time, τ. *D(h)* and *u(h)* can be extracted from the jump matrix data by means of a bayesian inference analysis,[100] where the jump matrix from experimental data are compared with the jump matrix obtained from solving the Smoluchowski equation (Eq 4.11) with test values of *D(h)* and *U(h)*. The analysis was performed for 4×10^7 steps with a histogram bin size of 50.

4.3.4 Steric Interaction Potential Analysis

Fig. 4.2 shows how an exponential fit to Milner's equation (Eq. 4.4) was used to analyze polymer brush steric interactions. The uncompressed brush thickness, δ_0, and brush compressibility, f_0, were calculated for symmetric brush layers. Those values were

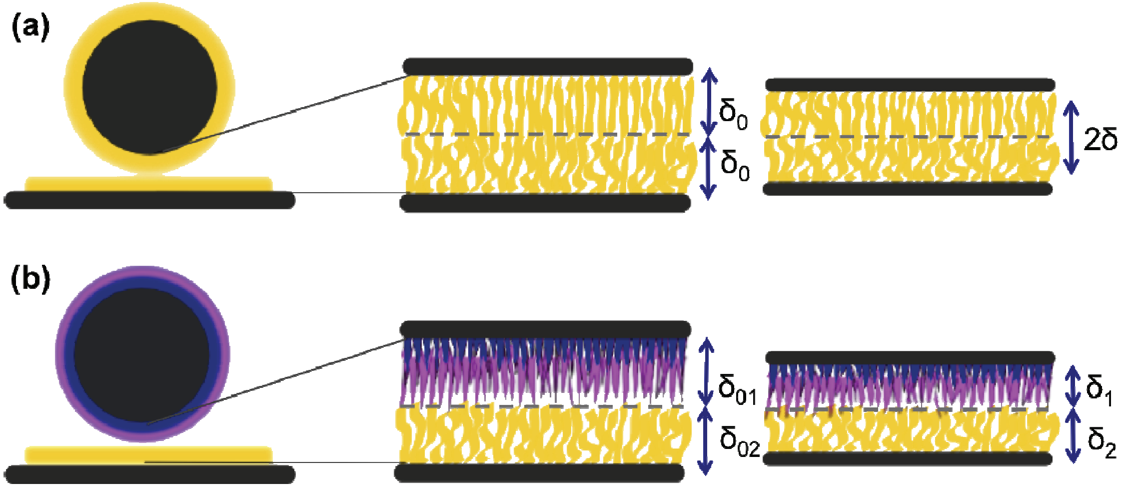

Figure 4.2 Schematic of polymer brush coated particles (grey circle) levitated over polymer brush coated wall (grey rectangle) *via* steric repulsive forces between the polymer brushes. (a) shows interacting symmetric mucin polymer layers (yellow) while (b) shows a particle coated with a PAH (blue)/PSS (pink) polyelectrolyte multilayer interacting with a mucin brush layer. δ_0 corresponds to the uncompressed brush height of the symmetric mucin layers. δ_{01} corresponds to the uncompressed brush height of the polyelectrolyte layer and δ_{02} corresponds to the uncompressed brush height of the mucin layer that interacts with the polyelectrolyte layer. δ corresponds to the compressed brush height of the symmetric mucin layers. δ_1 corresponds to the compressed brush height of the polyelectrolyte layer and δ_2 corresponds to the compressed brush height of the mucin layer that interacts with the polyelectrolyte layer.

used to determine the most probable height, h_m, for interacting layers undergoing small compression. Shim's bisection theory, which stipulates that the characteristic amount that a polymer layer compresses in response to a given force in the case of symmetric layers will remain consistent for asymmetric polymer layers, was applied in order to calculate asymmetric polymer brush steric interactions. The values of δ_0 and f_0 determined by the Milner brush theorem for symmetrical layers were used to compare interactions of asymmetrical layers. Fitting the exponential fit to Milner's equation for the free energy of symmetric brush layers (Eq. 4.4), uncompressed brush layer thickness and energy associated with compression under small compressive force was determined for pluronic, BSA, and mucin brush layers (Fig. 4.3a-c).

4.4 Results and Discussion

4.4.1 Symmetric Brush Layer Interactions

Fig. 4.3a-c reports interaction potentials between 2.34 μm SiO_2 colloids with physiadsorbed PEO copolymer or mucus or 1.59 μm SiO_2 colloids with physiadsorbed BSA and a glass microscope slide with an identical physiadsorbed macromolecular brush layer. Potential energy profiles for interactions between symmetric adsorbed brush layers were measured using TIRM and are shown for each individual colloidal particle, as well as the ensemble average of all levitated particles (red points). The ensemble average potential energy profile matches the profiles of the single particles within the limits of noise and particle polydispersity.

In addition to the directly measured potential energy profiles, Fig. 4.3a-c displays the theoretical separation dependent net particle-wall interaction potential (blue line) predicted using (Eq. (4.12)) with values from Table 4.1. The net particle-wall potential energy is a sum of gravity (Eq. (4.2)), as well as van der Waals attraction (Eq. (4.3)) and steric repulsion due to the interpenetration and compression of the adsorbed PEO copolymer, BSA, or mucus macromolecular layers (Eq (4.4)). At the 150 mM physiological ionic strength salt solution in which these measurements were conducted, electrostatic interactions can be neglected due to screening at distances > 1 nm. The uncompressed brush thickness, δ_0, and energy associated with brush layer compression, f_0, were calculated for each adsorbed macromolecular brush. These values were used to determine our only remaining fit parameter, the most probable height, h_m (dashed line), of the interacting symmetric brush layers which appear in Table 4.2.

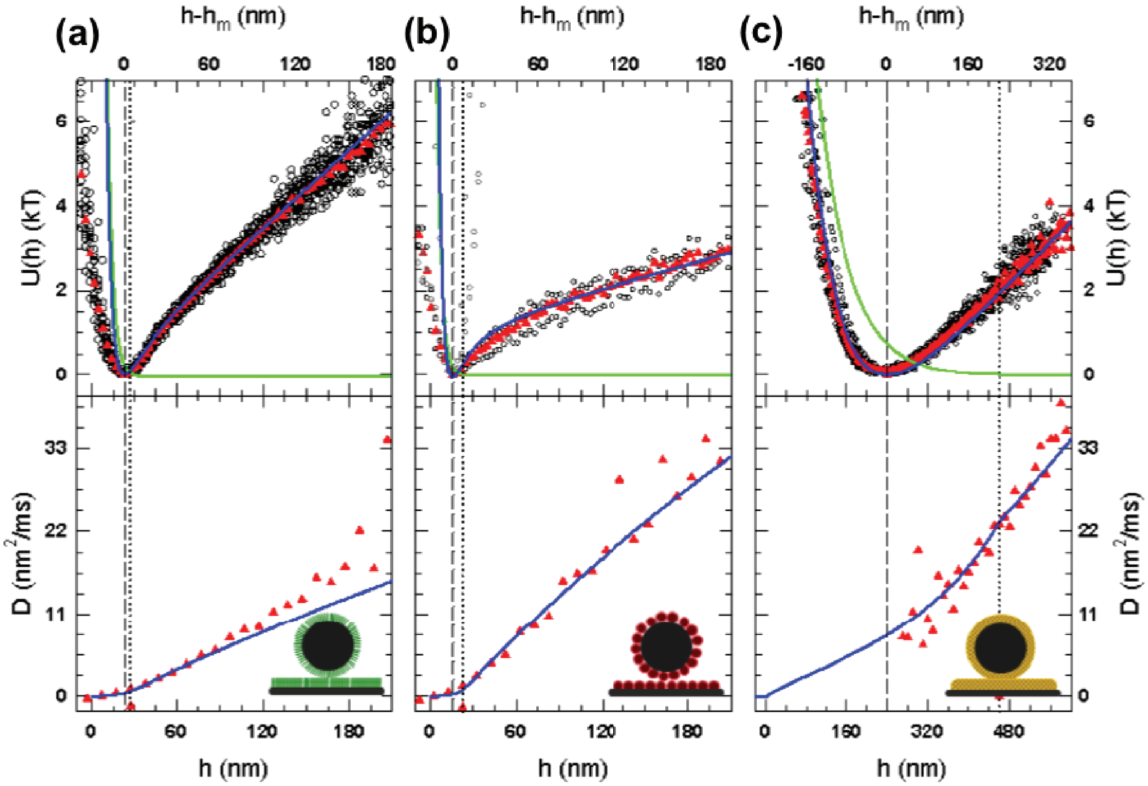

Figure 4.3 Ensemble TIRM measurements of particle-wall (top) potential energy profiles, $U(h)$, and (bottom) dynamic diffusivity profiles, $D(h)$ for particles and walls with the same surface functionalization. (top) Points are measured data from an equilibrium analysis of particle trajectories. Open circles are individual particle potential energy profiles for freely diffusing (black) or tethered (grey) colloids from an equilibrium analysis of particle trajectories. Solid lines are theoretical predictions for the steric repulsion potential from Eq. (4.4) (green) and the net interaction potential from Eq. (4.2) (blue). (bottom) Points are data from a nonequilibrium analysis of particle trajectories using Eq (4.11) and solid blue line is the theoretical prediction for the diffusivity profile from Eq. (4.5). Dashed lines indicate most sampled surface-to-surface separation distance, h_m, and dotted lines indicate $2\delta_{0,1}$ (Table 1). Solid red triangles are the ensemble average for freely diffusing colloidal particles. Insets depict the interacting brush layer types according to the schematics in Fig 4.1.

The theoretical separation dependent net particle-wall interaction potentials (Figs. 4.3a-c) utilize the theoretical prediction (Eq (4.4)) for particle-wall steric repulsion that arises between the adsorbed symmetric macromolecular layers on the colloid and wall surfaces as they approach contact, shown independently by the green line. Steric repulsion disappears when adsorbed symmetric macromolecular brush layers are no

Table 4.1.Parameters used in theoretical fits to calculate steric interaction potentials (Eq. (4.5)) for symmetric macromolecular brush layers in Fig. 4.2 and asymmetrical brush layers in Fig. 4.3 and 4.4.

Variable (units)	**Value**	**Source**	**Equation**
ρ_p (g/cm^3)	1.96	literature	(4.2)
ρ_f (g/cm^3)	1.00	literature	(4.2)
g (m*s^{-1})	9.8	literature	(4.2)
p	2.195	literature	(4.3)
A (k*T*nm$^{(p)}$)	2410	literature	(4.3)
δ_v (nm)	15	measured	(4.3)
Γ	10.6	defined	(4.4)
γ	7.38	defined	(4.4)
T(K)	291.89	measured	(4.6)
P	1.962	literature	(4.7)
η (kg*m*s^{-1})	1	literature	(4.9)

longer in contact (i.e., $h\text{-}h_m \geq 2\delta_0$). As an internal check in the quantitative agreement between the theoretical and measured net potential energy profiles against our ability to directly measure the strong forces in these systems, we verified that the steric repulsion generated by the brush layers decayed to 0 *kT* at a height corresponding to the sum of the uncompressed thickness of each brush layer (dotted line). For all three symmetric brush layers reported in Figs. 4.3a-c, this was the case. Remembering the effects of noise, a comparison of the directly measured ensemble average particle-wall potential energy with the theoretical interaction potential (i.e., red points and blue line, respectively) demonstrates excellent quantitative agreement.

The particle-wall potential energy profiles in Fig. 4.3a-c provide insight into the physical characteristics of the symmetric, interacting brush layers physiadsorbed to each

Table 4.2.Parameters used in theoretical fits to calculate steric interaction potentials (Eq. (4.5)) for symmetric macromolecular brush layers in Fig. 4.2 and asymmetrical brush layers in Fig. 4.3 and 4.4.

particle-wall functionalization	$2a$ (μm)	$\delta_{0,1}$ (nm)	$f_{0,1}$ (kT/μm^2)	$\delta_{0,2}$ (nm)	$f_{0,2}$ (kT/μm^2)	δ_B (nm)	h_m (nm)
Pluronic-Pluronic	2.90	13.2	95	—	—	12	22.8
BSA-BSA	1.97	11.2	40	—	—	5	15.8
Mucus-Mucus	2.15	230	2	—	—	90	240
BSA-Pluronic	2.95	11.2	40	13.2	95	9.6	17.5
Pluronic-Mucus	2.66	13.2	95	230	2	63	120
BSA-Mucus	2.60	11.2	40	230	2	68	120
0.25 mg/mL PSS-Mucus	2.65	15	12	230	2	65	120
1 mg/mL PSS-Mucus	2.60	18	5	230	2	62	120
1.5 mg/mL PSS-Mucus	2.64	22	4	230	2	71	120
2 mg/mL PSS-Mucus	2.65	50	2	230	2	70	130

surface. Fig. 4.3a shows plots of the interaction potentials for SiO_2 colloids and glass microscope slides with PEO copolymer physiadsorbed to both the particle and wall surfaces. Physiadsorbed PEO forms a short, dense brush that generates approximately hard-wall repulsion. The figure shows that all particles were robustly levitated and diffused over the flat wall. Both repulsive steric interactions and van der Waals attraction are experienced between the PEO copolymer functionalized colloids and wall. For this to be possible, the physiadsorbed PEO surface brush layer must be short enough that the particles are able to approach the wall within the small separation distances at which these forces are significant. Because all particles in this system were levitated and diffused over the surface, the repulsive steric interaction must dominate the van der Waals attraction. Finally, the theoretical fits to the ensemble average TIRM potential energy profile indicated a most probable height of h_m = 22.8 nm, only slightly less than the sum of two uncompressed brush layers, $2\delta_0$ = 26.4 nm. The small difference between h_m and $2\delta_0$ supports the stipulation that the PEO copolymer brush layers undergo little compression and interpenetration. A high energy penalty associated with compression, f_0 = 95 $kT/\mu m^2$ further verified the incompressibility of the brush layers.

Analogously, Fig. 4.3b reports particle-wall potentials for SiO_2 colloids and glass microscope slides with BSA physiadsorbed to both the particle and wall surfaces. Physiadsorbed BSA is thought to a form short, dense, globular surface layer. Unlike Fig. 4.3a and c, not all particles shown in Fig. 4.3b were robustly levitated over the flat wall (grey points). However, like Fig. 4.3a, both steric repulsion and van der Waals attraction are experienced between the BSA functionalized particle and wall surfaces. A comparison of Fig. 4.3a with 4.3b shows that more van der Waals attraction present in the BSA system. Greater van der Waals attraction indicates that the BSA macromolecular surface layer is shorter than that created by the physiadsorbed PEO copolymer layer. The most probable height of BSA physiadsorbed colloidal pobes that levitated and diffused, again obtained from fits to the ensemble average TIRM potential energy profile, h_m = 15.8 nm, further supporting a shorter physiadsorbed BSA surface layer (Fig. 4.3b) than physiadsorbed PEO copolymer (Fig. 4.3a). The most probable height for BSA physiadsorbed colloids interacting with a symmetrically coated wall was significantly less than the sum of two uncompressed macromolecular layers, $2\delta_0$ = 22.4 nm. This difference between h_m and $2\delta_0$ was larger difference than was observed in the compression of physiadsorbed PEO layers. Similarly, the energetic penalty associated with compressing a BSA layer, $f_0 = 40\ kT/\mu m^2$, was also less than that of PEO. Shorter layers and smaller energetic penalty associated with compression for physiadsorbed BSA layers (as compared to physiadsorbed PEO layers) combine to induce less colloidal steric stabilization.

Finally, Fig. 4.3c displays particle-wall potentials for SiO_2 colloids and glass microscope slides with mucus physiadsorbed to both the particle and wall surfaces. Physiadsorbed mucus is believed to form a thick, soft, compressible macromolecular surface layer. An analytical fit to the ensemble average potential energy profile from TIRM measurements in Fig. 4.3c showed no van der Waals attraction between the colloids and wall, and that all particles were robustly levitated and diffused over the surface. Negligible van der Waals interactions indicated that the mucus formed a macromolecular surface layer thicker than that of BSA and PEO. The most probable separation between the mucus functionalized colloids and the wall was comparably large at $h_m = 240$ nm. For particles and walls with macromolecular mucus layers that come into contact at $2\delta_0 = 460$ nm to interact with an $h_m = 240$ nm, the mucus layers had to be significantly more compressible than the PEO compolymer or BSA surface layers. The comparably low energetic penalty associated with compression of mucus macromolecular layer, $f_0 = 230\ kT/\mu m^2$, defends the large difference between the most probable height and the sum of two uncompressed brush layers.

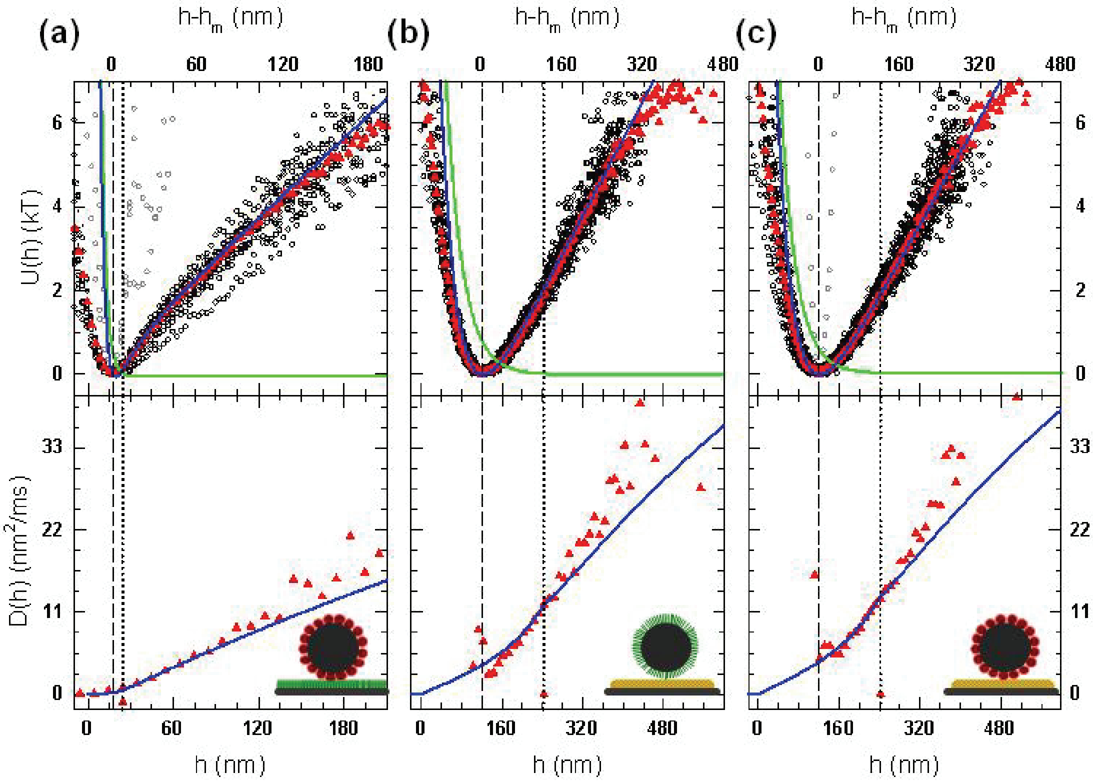

Figure 4.4. Ensemble TIRM measurements of particle-wall (top) potential energy profiles, *U*(*h*), and (bottom) dynamic diffusivity profiles, *D*(*h*) for particles and walls with asymmetric surface functionalizations. Data points and lines are plotted with the same representations as in Fig. 2. Insets depict the interacting brush layer types according to the schematics in Fig 1.

4.4.2 Steric Potential for Asymmetric Brush Layers

Fig. 4.4a-c reports interaction potentials between 3.19 μm SiO_2 colloids with physiadsorbed PEO copolymer or BSA with a glass microscope slide with an asymmetric physiadsorbed mucus or pluronic macromolecular brush layer. Potential energy profiles for interactions between asymmetric adsorbed brush layers were measured using TIRM and are shown for each individual colloidal particle, as well as the ensemble average of all levitated particles (red points). The ensemble average potential energy profile matches the profiles of the single particles within the limits of noise and particle polydispersity.

In addition to the directly measured potential energy profiles, Fig. 4.4a-c display the theoretical separation dependent net particle-wall interaction potential (blue line) predicted using (Eq. (4.5)) with values from Table 4.1. The uncompressed brush thicknesses, δ_{01} and δ_{02}, and energy associated with brush layer compression, $f_{01}$and f_{02}, utilized the values calculated from the corresponding experimental analysis of symmetric adsorbed macromolecular brushes. These values were used to calculate the most probable height, h_m (dashed line), of the interacting asymmetric brush layers, which appear in Table 4.2.

The theoretical separation dependent net particle-wall interaction potentials (Figs. 4.4a-c) utilize the theoretical prediction (Eq (4.4)) for particle-wall steric repulsion that arises between the adsorbed asymmetric macromolecular layers on the colloid and wall surfaces as they approach contact, shown independently by the green line. As was the case for steric repulsion generated by symmetric brush layers, the steric repulsion generated by asymmetric polymer brush layers decayed to 0 *kT* at a height corresponding to the sum of the uncompressed thickness of each brush layer (dotted line). Considering the effects of noise and that all brush parameters were utilized directly from the corresponding experimental results for interacting symmetric brush macromolecular layers, a comparison of the directly measured ensemble average particle-wall potential energy with the theoretical interaction potential (i.e., red points and blue line, respectively) demonstrates excellent quantitative agreement.

The exponential developed to characterize the steric repulsion contribution from each symmetric brush analyzed was used to analyze asymmetric polymer brush interactions between corresponding brushes. Shim's bisection theorem stipulates that each polymer layer in the asymmetric case compresses in response to a given force in the same manner as that polymer compresses for symmetric macromolecular layers. As such, Milner's equation, along with the values of δ_0 and f_0 determined for symmetric layers, could be directly applied to interactions in asymmetric cases (Table 4.1). The theoretical solution (black line, top) for each case shown in Fig. 4.4 shows the theoretical fit calculated from the previously measured δ_0 and f_0 values. For each asymmetric case, the theoretical solution (black line, top) showed excellent correlation to the ensemble average potential energy (red points, top).

Fig 4.4a, top graph, shows a graph of the potential energy measurements for BSA coated particles levitated over a pluronic coated wall. The values for the percentage of particles levitated and the most probable height were between those values for the symmetric pluronic and symmetric BSA cases. The consistent accuracy of this analytical method for two well-characterized cases of symmetric steric interactions between physiadsorbed polymers, pluronic and BSA, along with asymmetric steric interactions between pluronic and BSA indicate the strength of this analytical technique.

Both pluronic and BSA-coated particles were robustly levitated and diffused over mucus layers (Fig. 4.4b,c). As was the case for interacting symmetric mucus brush layers, the overall net potential energy interactions between particles with physiadsorbed pluronic copolymer or BSA polymer and a wall with a physiadsorbed mucus layer showed no van der Waals force. Also consistent with observations made from the symmetric polymer brush interactions, the most probable heights (h_m) calculated from the ensemble average potential energy corresponded to an absolute height significantly less than the sum of the uncompressed layers.

The interactions between the pluronic and mucus macromolecular layers are most probably uniquely repulsive, an assertion supported by all pluronic physiadsorbed particles levitating and diffusing over the mucus layer. Pluronic copolymer layers are uncharged with high steric repulsion due to their dense brush conformation and small compression. BSA, alternately, has the coexistence of positive and negative charges within the polymer brush layer and forms a short, compressible layer. Increased potential for attractive mechanical and electrostatic interactions between BSA and mucus polymer brush layers over interacting pluronic and mucus polymer brush layers likely led to the higher percentage of stuck BSA particles that was observed.

4.4.3 Polyelectrolyte Tethering

Fig. 4.5 reports interaction potentials between 2.34 μm SiO_2 colloids with physiadsorbed polyelectrolyte polymer with a glass microscope slide with an asymmetric physiadsorbed mucus macromolecular brush layer. Potential energy profiles for interactions between asymmetric adsorbed brush layers were measured using TIRM and are shown for each individual colloidal particle, as well as the ensemble average of all levitated particles (red points). The ensemble average potential energy profile matches the profiles of the single particles within the limits of noise and particle polydispersity.

In addition to the directly measured potential energy profiles, Fig. 4.5 displays the theoretical separation dependent net particle-wall interaction potential (blue line) predicted using (Eq. 4.5) with values from Table 4.1. Physiadsorbed polyelectrolyte polymer formed a short, compressible layer.Even with multiple polyelectrolyte layers, polyelectrolyte polymers physiadsorbed symmetrically to colloidal particles and to the wall could not create sufficient steric repulsion for the colloidal probes to be stable and to

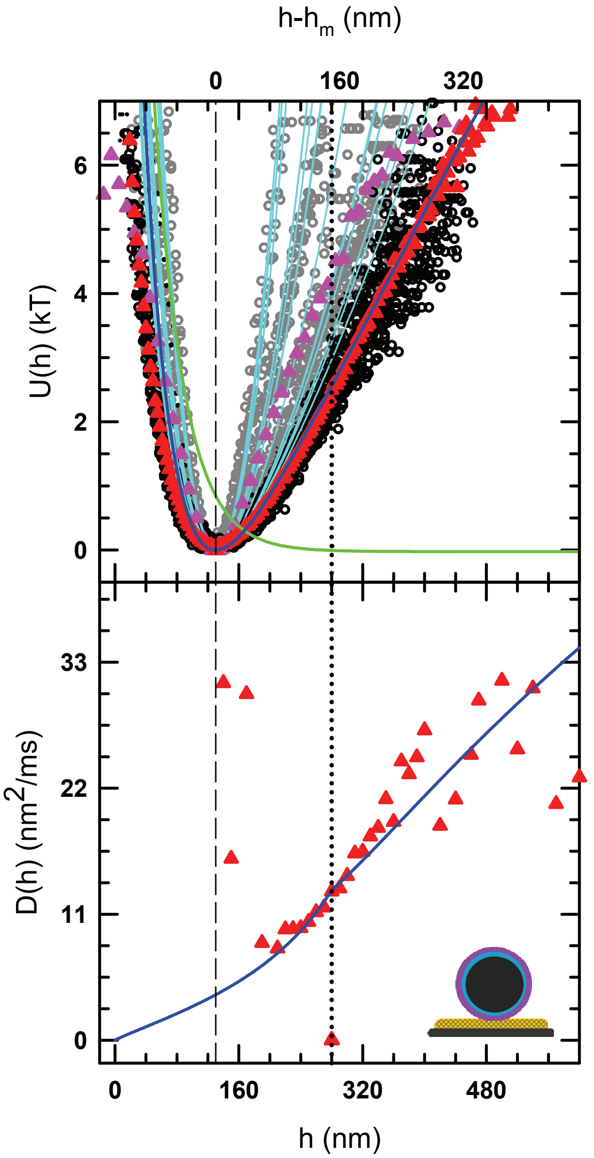

Figure 4.5.Ensemble TIRM measurement of particle-wall (top) potential energy profiles, $U(h)$, and (bottom) dynamic diffusivity profile, $D(h)$ for particles with 2 mg/mL of negatively charged PSS polyelectrolyte adsorbed over positively charged PAH polyelectrolyte and a mucus coated wall.Data points and lines are plotted with the same representations as in Fig. 2 and 3.Inset depicts the interacting brush layer types according to the schematics in Fig. 1.

levitate. Analysis of colloidal probes levitated via asymmetric polymer layers utilized the parameters calculated from symmetric mucus brush interactions (Table 2) while the polyelectrolyte brush parameters were calculated from the theoretical potential energy fit (blue line, top) to the ensemble average for the particle potential energy (red points, top). Analysis of tethered colloidal probes utilized a literature value for the persistence length of a mucin to model each tethered particle as a Hookian spring (light blue line, top). The ensemble average for the particle potential energy for all particles (tethered and particles that diffused) is shown by the pink points, top.

The theoretical separation dependent net particle-wall interaction potentials for levitated particles (Fig. 4.5) utilize the theoretical prediction (Eq (4.5)) for particle-wall steric repulsion that arises between the adsorbed asymmetric macromolecular layers on the colloid and wall surfaces as they approach contact, shown independently by the green line. The steric repulsion generated by asymmetric polymer brush layers decayed to 0 *kT* at a height corresponding to the sum of the uncompressed thickness of each brush layer (dotted line). Considering the effects of noise, a comparison of the directly measured ensemble average particle-wall potential energy of levited colloidal probes that diffused over the surface with the theoretical interaction potential (i.e., red points and blue line, respectively) demonstrates excellent quantitative agreement.

Polyelectrolyte polymers were used to mimic viral vectors *via* layer-by-layer adsorption of positive and negative charges. Particles physiadsorbed with only negative polyelectrolyte polymer, PAH, stuck tightly to the mucus layer, while particles physiadsorbed with a layer of PAH followed by a layer of positive polyelectrolyte polymer, PSS, levitated (black points, top) or tethered (grey points, top). Since the most probable height was 120 nm for both pluronic and BSA coated particles over mucus, the most probable height was set to 120 nm for the polyelectrolyte case to reduce the unknown parameters in the analysis (Table 2). The uncompressed brush thickness, δ_0, and the energetic penalty for compression, f_0, were consistent layers incapable of creating sufficient steric repulsion to stabilize particles over a wall *via* symmetric polyelectrolyte polymer physiadsorption. The relatively large uncompressed brush thickness and high compressibility are consistent with long polymer loops or dangling chains.

A dense PSS layer was expected to carry a large negative charge and lead to 100% levitation of the colloidal particles. The dangling loops and chains in the polyelectrolyte layers lead to tethering between the particles coated with PSS and the mucin layer. Tethering could result from PAH polymers penetrating the PSS layer and binding electrostatically to the mucin layer or from dangling PSS polymer loops forming mechanical entanglements with mucin polymers. The wide and varied parabolic potential energy profiles indicate loosely tethered particles with tethers of varied lengths (light blue lines, top). Both polyelectrolyte polymers and BSA polymers created positive and negative charges on the outer layer of the colloidal probe polymer coatings that interacted with the mucin layers. Particles physiadsorbed with polyelectrolyte polymer likely stuck to mucus layers while colloidal particles physiadsorbed with BSA levitated due to the size scale of the separation of charge within the layers. Since the charges exist within the polymer chain for proteins and on separate polymer chains for polyelectrolytes, the size scale of charge separation within protein layers is significantly smaller than within polyelectrolyte layers. BSA, as a globular protein, would also be unlikely to form mechanical tethers with mucus.

4.4.4 Dynamic Diffusivity and Hydrodynamic Permeability for Symmetric Brush Layers

Fig 4.3a-c, bottom graph, shows the ensemble average dynamic diffusivity profile with respect to absolute particle height for colloidal probes with physiadsorbed PEO copolymer, BSA, and mucus brush layers with diffusing over a wall physiadsorbed with a symmetric polymer brush. The dynamic diffusivity was measured using Bayesian inference analysis, calculated by the Smoluchowski equation (Eq. 4.11), and fit to Russell and Poutanin's equations for parabolic brush layers. For graphical analysis, surface contact was set to an absolute height of 0 nm and contact between uncompressed polymer layers, L, was set to $2\delta_0$ (black dotted line). Diffusivity disappeared at surface contact (*h=0*). The Brinkman permeability coefficient (δ_B) was the sole parameter manipulated to analytically fit the particle diffusivity ensemble average (red points, bottom), and is directly related to the slope of the solution (blue line, bottom). Table 4.2 shows the Brinkman permeability coefficient for symmetric physiadsorbed PEO copolymer, BSA, and mucus brush layers. Dynamic diffusivity profiles for colloidal probes diffusing over a wall with symmetrically adsorbed brush layers were measured using TIRM and are shown for the ensemble average of all levitated particles (red points, bottom). The ensemble average dynamic diffusivity matches the ensemble average profiles within the limits of noise and particle polydispersity.

Fig. 4.3a, bottom graph, shows the dynamic diffusivity of PEO copolymer physiadsorbed particles diffusing over a wall also physiadsorbed with PEO copolymer. The small relative distance between polymer brush contact (dotted line) and the most probable height (dashed line) is consistent with poluronic's dense bottle-brush conformations. The Brinkman permeability coefficient (δ_B) calculated from the analytical fit (blue line, bottom) to the dynamic diffusivity ensemble average (red points, bottom), directly related to the level of hydrodynamic penetration, was higher than would be expected for a dense, non-compressible brush layer (Table 4.2). However, Russell and

Potanin's equation is sensitive to dangling polymer chains, which is consistent with the extended chain conformation of the individual PEO copolymers comprising the polymer brush.

Fig. 4.3b, bottom graph, shows the dynamic diffusivity of BSA physiadsorbed colloidal probes diffusing over a wall also physiadsorbed with BSA. The distance between BSA brush contact (dotted line) and the most probable height (dashed line) is larger than that for pluronic. The Brinkman permeability coefficient used to analytically fit (blue line, bottom) the dynamic diffusivity ensemble average (red points, bottom), was significantly lower than the Brinkman permeability coefficient calculated for symmetric physiadsorbed PEO copolymer layers (Table 4.2). While the slope of the theoretical fit to dynamic diffusivity corresponds to Brinkman permeability, it also relates to the average radius of the colloidal particles. Since the potential energy due to gravity is smaller for the BSA particles than for the pluronic particles (Table 4.1), the overall diffusivity is larger for BSA physiadsorbed colloidal probes than for colloidal probes physiadsorbed with PEO copolymer, despite a smaller Brinkman permeability coefficient. The low hydrodynamic penetration is consistent with the globular conformation of the BSA protein layer.

Fig. 4.3c, bottom graph, shows the dynamic diffusivity of colloidal probes diffusing over a wall with symmetrically physiadsorbed mucus. The most probable height (dashed line) is approximately half the height of initial brush contact (dotted line), a significantly larger relative difference than was observed for pluronic or BSA. Interacting mucus layers had a very large Brinkman permeability coefficient of 90 nm (Table 2), shown by the analytical fit (blue line, bottom) and the dynamic diffusivity ensemble average (red points, bottom). Overall, the difference between the most probable height and the height of two uncompressed layers,along with the large Brinkmann permeability, support the formation of a highly compressible and hydrodynamically permeable layer: a mesh layer.

4.4.5Dynamic Diffusivity and Hydrodynamic Permeability for Asymmetric Brush Layers

Fig 4.4a-c, bottom graph, shows the ensemble average dynamic diffusivity profile with respect to absolute particle height for colloidal probes with physiadsorbed PEO copolymer, BSA, and mucus brush layers with diffusing over a wall physiadsorbed with an asymmetric polymer brush. As in the asymmetric potential energy analysis, the dynamic diffusivity and Boltzmann permeability coefficient were calculated based on fitting parameters found from analysis of symmetric brush layers (Table 4.2). Surface contact was set to an absolute height of 0 nm. In this case, contact between uncompressed polymer layers, L, was set to (δ_{01}+δ_{02}). Diffusion was again set to zero at surface contact (*h=0)*. Diffusivity disappeared at surface contact (*h=0).* Brinkman permeability coefficient (δ_B) was manipulated to analytically fit the particle diffusivity ensemble average (red points, bottom). Table 4.2 shows the Brinkman permeability coefficients for asymmetric physiadsorbed PEO copolymer, BSA, and mucus brush layers. The ensemble average dynamic diffusivity matches the ensemble average profile within the limits of noise and particle polydispersity.

Fig. 4.4a, bottom graph, shows the dynamic diffusivity of BSA physiadsorbed colloidal probes diffusing over a wall with physiadsorbed PEO copolymer. The most probable height (dashed line) fell close to the absolute height of BSA and PEO copolymer brush contact (dotted line). The Brinkmann permeability coefficient was calculated from the analytical fit (blue line, bottom) to the dynamic diffusivity ensemble average (red points, bottom). As with the parameters found from the analysis of asymmetric brush potential energy interactions between pluronic and BSA layers, the dynamic diffusivity parameters also lie between the equivalent numbers found from the analysis of symmetric brush interactions for physiadsorbed PEO copolymer layers and for BSA polymer layers (Table 4.2).

Fig. 4b,c, bottom graphs, show the dynamic diffusivity of colloidal particles physiadsorbed with PEO copolymer and with BSA, respectively, over wall with a physiadsorbed mucus layer. The most probable height is 2nm less than $(\delta_{01}+\delta_{02})/2$ for the pluronic case and equal to $(\delta_{01}+\delta_{02})/2$ for the BSA case, significantly less than the value calculated by averaging the most probable height for symmetric PEO copolymer layers and mucus layers or BSA layers and mucus layers. This deviation from the previously observed trend in the relationship between symmetric and asymmetric parameters demonstrates a different type of interaction between PEO copolymer and mucus and between BSA polymer and mucus. As symmetric PEO copolymer brush interactions supported the presence of dangling polymer chains, those chains likely penetrated into the porous mucus layer. Physiadsorbed BSA polymer was found to be globular without dangling chains. Instead of interacting with mucus mechanically, BSA would interact with the mucus electrostatically; a small attraction that decreased the overall most probable height. For both asymmetric mucus systems, the Brinkman permeability coefficients calculated from the analytical fits (blue line, bottom) to the dynamic diffusivity ensemble averages (red points, bottom) also fell closer to the value measured for symmetric mucus layers than would be expected based on the previously observed trend of parameters for symmetric interactions averaging to give the parameters for asymmetric interactions (Table 4.2). Overall mucus diffusion parameters dominated over PEO copolymer or BSA. The Brinkman permeability coefficient calculated from the analytical fits (Fig. 4.5) (blue line, bottom) to the dynamic diffusivity ensemble averages (red points, bottom) for polyelectrolyte physiadsorbed particles diffusing over a mucus coated wall was comparable to the coefficients for pluronic and BSA-coated particles over mucus.

4.4.6 Electokinetic Potential and Colloidal Stability

Polyelectrolyte adsorption conditions were determined by measuring electrokinetic potential of colloidal particles adsorbed with polyelectrolytes under varying adsorption conditions. Fig. 4.6 (bottom) shows the electrokinetic potential of colloidal particles as a function of PSS adsorption concentration and adsorption time. Symbols correspond to adsorption of PSS (circles) or PAH at an adsorption concentration of 26 mg/mL (blue), 13 mg/mL (red), and 1 mg/mL (cyan) followed by PSS (squares) for either 10 min (open) or 20 min (closed) each. Adsorption times of 10 minutes yielded electrokinetic potentials that varied widely between trials (open symbols) while adsorption times of 20 min (closed symbols) yieled layers with reproducible electrokinetic potential of approximately 0 mV must necessarily have both positive and negative charges in the outer polymer layer. Due to its stability and its electokinetic potential of roughly 0 mV, 20 min adsorption times and 26 mg/mL PAH polyelectrolyte adsorption concentration were found to form polyelectrolyte layers that, after PSS adsorption, most closely mimicked the outer coating of mucopenetrating viruses. Fig. 4.5 (top) shows the stability of sterically stabilized colloids compared to the PSS

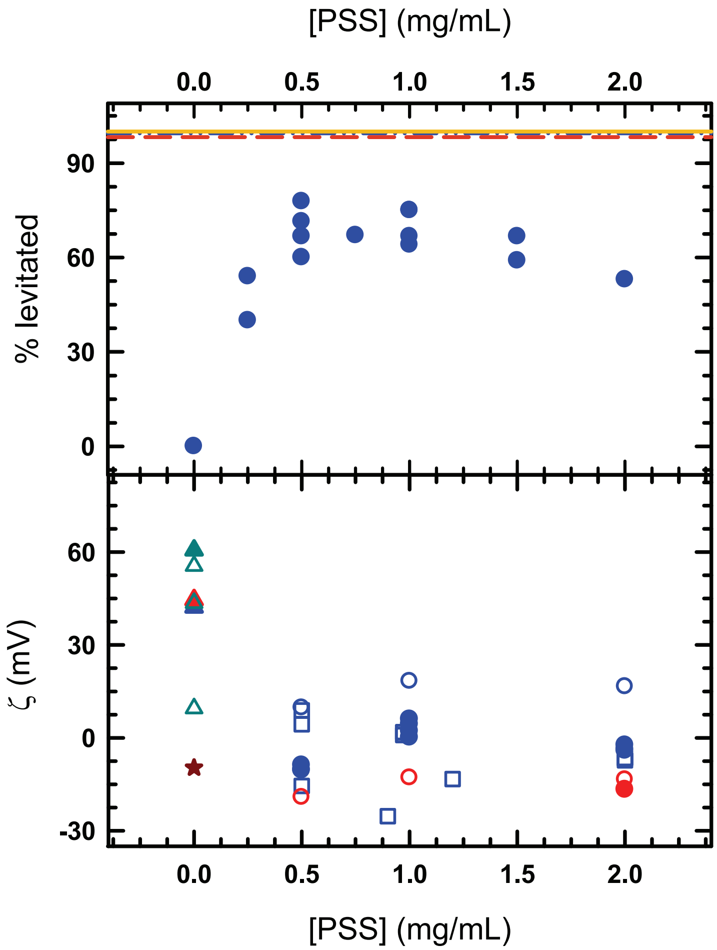

Figure 4.5**.** (top) Percentage of levitated particles over a flat wall with an adsorbed mucus layer as a function PSS adsorption concentration. Lines show the percentage of levitated particles functionalized with mucus (yellow, solid), pluronic (green, dotted), or BSA (dark red, dashed) coatings. (bottom) Zeta potential of colloidal particles as a function of PSS adsorption concentration and adsorption time. Symbols correspond to adsorption of PSS (circles) or PAH at an adsorption concentration of 26 mg/mL (blue), 13 mg/mL (red), and 1 mg/mL (cyan) followed by PSS (squares) for either 10 min (open) or 20 min (closed) each. Dark red star shows the zeta potential for BSA.

polyelectrolye absorption concentration (blue points) along with the colloidal stability of particles physiadsorbed with PEO copolymer (blue dotted, top), BSA (red dashed, top), and mucus (yellow, top). The particles were first physiadsorbed with positively charged polyelectrolyte, PAH, followed by adsorption of negatively charged polyelectrolyte, PSS. The PSS adsorption concentration was increased from 0 mg/mL to 2 mg/mL. Particles with only a physiadsorbed PAH layer were 100% stuck to the wall with physiadsorbed mucus. Adding a layer of PSS polyelectrolyte on top of the PAH layer stabilized the colloidal particles. The percentage of particles that levitated and diffused over the mucus physiadsorbed wall was expected to increase with adsorption concentration. As shown by Fig. 4.5, the percentage of levitated colloids with initially increased with adsorption concentrations up to 1 mg/mL and then decreased as the adsorption concentration was increased.

Initially, negatively charged PSS polyelectrolyte created a negatively charged barrier between the positively charged PAH polyelectrolyte layer and the negatively charged mucus layer that coated the wall. As demonstrated by the theoretical analysis of net potential energy interactions between polyelectrolyte physiadsorbed particles and a mucus coated wall, polyelectrolytes adsorb in a loose conformation of dangling loops and chains (Fig. 4.5). Due to the dangling polymer conformation, polyelectrolyte multilayers do not form distinct layers. At low PSS polyelectrolyte adsorption concentration, PAH polyelectrolyte chains penetrated the outer PSS layer to electrostatically bind the coated colloidal particle to the mucin layer. As adsorption concentration increases, fewer PAH polyelectrolyte chains were able to penetrate the PSS polyelectrolyte layer and bind to the mucus layer, increasing the percentage of particles that levitated and diffused over the surface. At high adsorption concentrations, colloidal stability again decreased. The decrease in the number of particles thatlevitated and diffused over the surface , despite a thick, negatively charged outer layer, indicates mechanical binding between long chains dangling from the thick polyelectrolyte layers and the soft, porous mucus layer. At the PSS adsorption concentration that minimized the destabilizing effects of electrostatics and mechanical entanglement, 1 mg/mL, the colloidal stability reached approximately 80%, a significantly lower concentration of particles physiadsorbed with pluronic, BSA, or mucus that levitated and diffused over a mucus coated wall.

4.5 Conclusion

In summary, various types of virus-mimicing colloidal particles were levitated over a mucus layer and their potential energy and hydrodynamic interactions measured using TIRM in conjunction with BIA. This work utilized novel analysis techniques to describe interactions between polymer brushes to give new insight into the conformation and behavior of adsorbed mucus brush layers and potential DDPs. A universally applicable exponential equation was set to Milner's equation for steric potentials of brush layers to easily obtain symmetric and asymmetric steric potentials. Bayesian Inference analysis used the Smoluchowski equation to simultaneously measure thermodynamic (*i.e.*, free energy) and hydrodynamic properties (*i.e.*, diffusivity) of the interacting polymer brushes. These measurements and subsequent analysis provide insight into potentially effective pulmonary drug delivery vectors. The size scale of charge separation within charged layers was found to be a significant factor in whether particles stuck to or levitated over a mucin layer. The conformation of the layers was also found to be significant in terms of sticking verses levitation of particles. Future work includes the measurement of potential drug delivery particles within mucus layers and acceptance into pulmonary cells.

5. SPECIFIC AND NONSPECIFIC DRUG DELIVERY PARTICLE-MUCUS HYDRONAMIC INTERACTIONS

Fluorescent diffusion across a microfluidic channel was used to measure hydrodynamic interactions between virus-mimicking stealth drug delivery particles and dissolved mucins. Specifically, BSA and ConA proteins along with particles coated with polyethelyne glycol or BSA layers were studied. A constant pressure microfluidic system was used to inject solutions into a Y-junction microfluidic device. A novel analytical theory was developed to measure the rate of gradient diffusion, long time self diffusion, and diffusion into polymer (mucin) suspension. Experimental data was fit to data generated *via* Comsol computational platform using analygous parameters and to theoretical solutions. This paper gives new insight into hydrodynamic interactions as they affect diffusion of virus-mimicking drug delivery particles through a mucin suspension. polyethelyne glycol layers were found to facilitate rapid mucopenetration while ConA and BSA were found to bind to mucins *via* electrostatic and hydrophobic interactions, respectively.

5.1 Introduction

Hydrodynamic and intermolecular interactions in colloidal dispersions contribute to a number of important colloidal phenomena including aggregation, crystallization, filtration, and drug delivery. Characterizing colloidal diffusion is paramount to designing effective filtration, efficient drug delivery systems,[56,57] and effective microfluidic devices.[58-60] Comparing gradient and self diffusion enables a thorough analysis of governing interactions to determining a complete empirical solution for diffusion. Rigorous analytical solutions exist for self and gradient diffusion in concentrated and dilute suspensions. While colloidal diffusion is widely studied, simple and accessible experimental techniques to measure diffusion experimentally are somewhat limited. The experiments in this paper illucidate the specific and nonspecific interactions that affect colloidal diffusion as applied to diffusion of drug delivery particles though mucus.

Current experimental techniques for observing colloidal diffusion have been used to measure short time self diffusion, long time self diffusion, or gradient diffusion individually. Particle tracking is often used to measure the short time self diffusion[66] and has been used to measure diffusion of drug delivery particles (DDPs) through mucus.[1,11,47,62] Particle tracking measures only short correlation time and small observation area. Due to scope limitations, particle tracking fails to give details of particle-mucus specific interactions. Long time self diffusion has been primarily studied *via* computer simulation and tracking fluorescently tagged or radiolabeled tracer particles. The most widely used experimental techniques for measuring self diffusion are Fluorescence Recovery After Photobleaching (FRAP) and Dynamic Light Scattering (DLS), which give broad diffusion information without insight into specific interactions[11,62,92] or a straight-forward means to compare the analytical results with short time diffusivity or gradient diffusion results.[65] Chromatography, polymer gel release and diffusion across a microfluidic channel have been used to experimentally measure gradient diffusion. Of these techniques, diffusion across a channel in a microfluidic device has the widest application across varying systems; easily translated between gradient and self diffusion and a wide array of colloidal systems.

Microfluidic devices measure flow at low Reynolds numbers where flow is laminar and the inertia negligible.[59,61,62,63] Elimination of inertial effects enables flow manipulation and analysis of additional hydrodynamic complexities such as pressure gradients, electrical potentials, magnetic potentials, and capillary forces.[58,64-66] Specific and nonspecific interactions in particle, polymers, and non-newtonian fluids can be measured[59,67,68] and diffusion more easily calculated in stokesian flow.[69] Y-junctions, also known as T-sensors, are microfluidic devices that utilize multiple entry channels merging into one channel to create multiple parallel laminar streams and enable simple hydrodynamic manipulation and measurement.[58,59,68,102] T-sensors have wide breadth of application, including altering surface chemistry to compare cell deposition and migration[60,102-104] laminar flow fabrication,[104] controlled chemical reactions,[59,64,105] and diffusivity measurements.[58,67,103,106] The T-sensor has been used to quantify factors affecting colloidal diffusion and migration such as diffusiophoresis, the effects of non-newtonian dispersant and interdiffusion.[60,107]

Measuring diffusion of drug delivery particles through mucus is necessary for efficient pulmonary drug delivery. Mucin polymers, the primary component of mucus, are characterized as nonassociated random coils[48] or wormlike chain polymers[48,108] at low concentrations, an entangled freely jointed chain at intermediate concentrations, and as a cross-linked gel above its sol-gel transition concentration.[6,33,48,109] Particle tracking has been used to measure DDP diffusion through mucus and correlating fluorescence intensity with macromolecule concentration has been used to measure the diffusion coefficients for different biomacromolecules in mucus as compared to phosphate buffer solution.[9,10,46,47,57] As mentioned above, these experiments fail to identify and measure important specific interactions between DDPs or macromolecules and mucins.Precise control of interactions between DDPs and mucin polymers enables the development of efficiently penetrating vectors.[47,56,57]

The experiments reported in this paper utilize a Y-junction microfluidic device and a constant pressure system to measure the diffusion of fluorescently labeled colloids through mucus. Experimental results for gradient and self diffusion of bovine serum albumin (BSA) and Conconavalin-A (ConA) polymers and colloidal probes coated with BSA and Pluronic colloids and diffusion into mucus polymer studied (Fig. 5.1). Matching the gradient and long time self diffusion of each colloidal system to analytical theory enabled the calculation of nonspecific hydrodynamic diffusive interactions. Calculating nonspecific interactions related to colloidal concentration and hydrodynamic forces within the microfluidic channel enabled separation and calculation of specific interactions between colloids and mucus as they affected the diffusion coefficients. The technique developed is widely applicable to measurement of complex colloidal phenomena and diffusion in microfluidic devices, and also has the potential to significantly aid in the development of efficient pulmonary drug delivery vectors.

5.2 Theory

5.2.1 Colloidal Diffusion

Colloidal diffusion in a solution is described by Fick's laws.Fick's first law states that:[79]

$$J = -D(\phi)\frac{\partial \phi}{\partial x} \tag{5.1}$$

where J equals the flux of Brownian particulates, D equals the particulate diffusivity and Φ corresponds to the concentration of particulates in the test solution. Using the

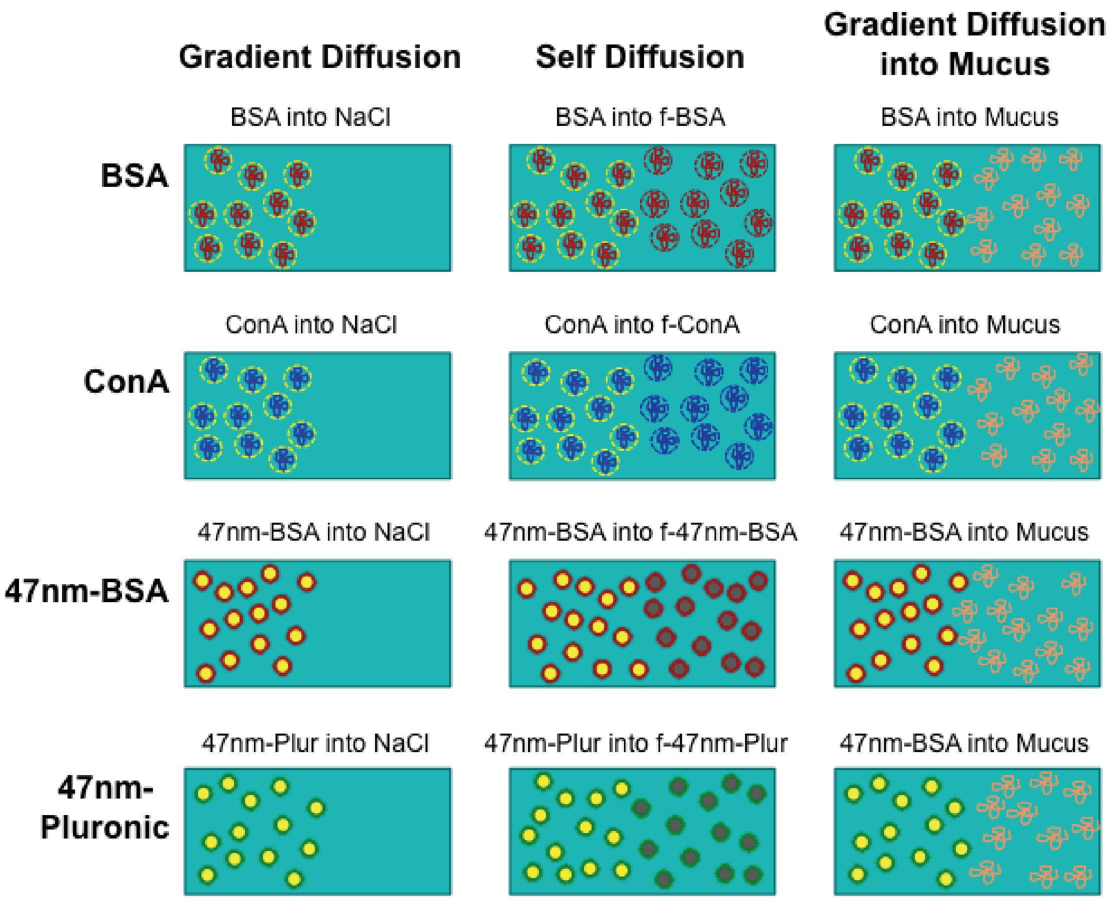

Figure 5.1 Schematic of diffusion experiments. Gradient diffusion of dilute BSA polymer solution, ConA polymer solution, 47 nm BSA coated colloidal particle dispersion, and 47 nm pluronic coated colloidal particle dispersion was measured and fit to analytical theory. Long time self diffusion of dilute BSA polymer solution, ConA polymer solution, 47 nm BSA coated colloidal particle dispersion, and 47 nm pluronic coated colloidal particle dispersion was measured by tracking the diffusion of the fluorescent population into the non-fluorescent population. Last, gradient diffusion of BSA polymer solution, ConA polymer solution, 47 nm BSA coated colloidal particle dispersion, and 47 nm pluronic coated colloidal particle dispersion into a mucus solution was measured and fit to analytical theory.

continuity equation, the change in concentration of the test solution over time, *t*, can be found as,

$$\frac{\partial \phi}{\partial t} = -\nabla \cdot J \tag{5.2}$$

Where t equals time,Fick's second law can be derived as

$$\frac{\partial \phi}{\partial t} = \nabla \cdot \left(D \frac{\partial \phi}{\partial x} \right) \tag{5.3}$$

The diffusivity of a Brownian particle in solution is given by Stokes' equation:[80]

$$D_0 = \frac{k_B T}{f} \tag{5.4}$$

Where D_0 corresponds to the Stokes diffusivity coefficient, k_B equals the Boltzmann constant, T equals temperature, and f corresponds to friction between the Brownian particle and the solution. Einstein defined that friction as

$$f = 6\pi\mu a \tag{5.5}$$

where μ corresponds to the solution viscosity and a is the radius of the Brownian particle. Combined, the Stokes-Einstein equation gives the diffusivity of a Brownian particle in solution in the absence of any additional conservative or nonconservative interactions as

$$D_0 = \frac{k_B T}{6\pi\mu a} \tag{5.6}$$

In a concentrate particle solution, particle interactions can affect the diffusivity of the particles.In this case, the diffusivity is[83]

$$D(\phi) = D_0 K(\phi) \frac{d\left[\phi Z(\phi)\right]}{d\phi} \tag{5.7}$$

where K(Φ) corresponds to the sedimentation coefficient which, for a hard sphere, is given by the equation

$$K(\phi) = (1 - 6.55\phi) \tag{5.8}$$

and Z(Φ) is the compressibility factor given by the equation

$$Z(\phi) = \frac{\Pi}{nk_B T} = 1 + A_2\phi + \ldots \tag{5.9}$$

where Π is the osmotic pressure, *n* corresponds to number density, and *A* corresponds to the second virial coefficient.

In the case of dilute solutions where interparticle interactions are negligible, Z(Φ) and K(Φ) each go to 1 and Bachelor's equation reduces to

$$D(\phi) = D_0 \tag{5.10}$$

In this scenario, the solution to Fick's second law for two semi infinite solutions joined at x=0 where at t=0 the first concentration (Φ_1) equals 1 and the second concentration (Φ_2) equals 0 is

$$\phi(x) = \bar{\phi} + \frac{\Delta\phi}{2} erf\left(\frac{x}{\sqrt{4D_0 t}}\right) \tag{5.11}$$

For the case of long time self diffusion in a concentrated suspension where particle interactions must be taken into account, neither K(Φ) nor Z(Φ) is constant. Still, the overall concentration is constant. As such, the governing equations are

$$J_f = -D(\phi_S)\frac{\partial \phi_f}{\partial x} \tag{5.12}$$

where J_f corresponds to the flux of fluorescently tagged particles, ϕ_S corresponds to the particulate concentration of the solution, and ϕ_f corresponds to the concentration of the fluorescently tagged particles, and

$$D(\phi) = D_0 K(\phi)\frac{d\left[\phi Z(\phi)\right]}{d\phi} = D_1 \tag{5.13}$$

where D_1 corresponds to the diffusion coefficient taking into account interparticle interactions. Since the diffusivity in this scenario is constant, the concentration with respect to time can still be described with Fick's second law and solved using the solution

$$\phi(x) = \overline{\phi} + \frac{\Delta\phi}{2} erf\left(\frac{x}{\sqrt{4D_1 t}}\right) \tag{5.14}$$

For the third case of gradient diffusion in a concentrated suspension where particle interactions must be taken into account, K(Φ), Z(Φ) and Φ all vary as a function of position and time. As such, Bachelor's equation does not give a constant solution and Fick's second law

$$\frac{\partial \phi}{\partial t} = \nabla \cdot \left\{ D\left[\phi(x)\right] \frac{\partial \phi}{\partial x} \right\} \tag{5.15}$$

yields a differential equation without an analytical solution.

5.3 Materials and Methods

5.3.1 Colloidal Dispersions

Nominal 47nm diameter polystyrene colloids fluorescent and nonfluorescent carboxylated polystyrene colloids of varying diameters were used for measuring diffusion in microfluidic devices (Thermo Scientific, Waltham, MA). PEO-poly(propylene oxide)-PEO triblock copolymer (F108 Pluronic®, BASF, Wyandotte, MI) with segment molecular weights of 5400/3300/5400 g/mol was dissolved at 2.5 mg/mL in DI water and Bovine Serum Albumin (BSA, Sigma Aldrich, St. Louis, MO) was dissolved at 1.5 mg/mL in DI solution. These solutions were used to functionalize the colloids. 2 mL of Pluronic® or BSA solution was deposited in a 3.5 mL screw cap Cryovial (VWR, Batavia, IL) and 0.5 mL of polystyrene colloids was added. The particle-polymer dispersion was sonicated for 10 minutes and set on a rotating shaker to allow the polymer to adsorb to the particles. Pluronic® was adsorbed for 4 hrs and BSA was allowed 12 hrs to adsorb. Prior to experimentation, 5 M NaCl was then added to the dispersion to return the ionic strength to 0.15 M. To prevent diffusion effects from gradients in polymer concentration or ionic strength, the same Pluronic® and NaCl stock solutions were used to prepare the solution of nonfluorescent solution or particle dispersion into which the fluorescent particles diffused. For gradient diffusion experiments, the solution included 0.5 mL DI in place of the particle dispersion. For self-diffusion experiments, nonfluorescent particles of equal diameter were used in the place of fluorescent particles.

BSA Fluorecein isothiocyanate (FITC) conjugate (Sigma-Aldrich Company, St. Louis, MO), Concanavalin A (ConA, Sigma-Aldrich Company, St. Louis, MO), ConA FITC conjugate (Sigma-Aldrich Company, St. Louis, MO) and lyophilized mucus from bovine submaxillary glands (BSM, Sigma-Aldrich Company, St. Louis, MO) were used to track the diffusion of fluorescent proteins. BSA was dissolved at a concentration of 2 mg/mL and ConA at a concentration of 3 mg/mL in 0.15 M NaCl solution. For self diffusion experiments, non-fluorescent BSA and ConA were dissolved at concentrations equal to the concentration of the corresponding fluorescent protein. BSM was dissolved in 0.15 M NaCl, 10 mM phosphate buffer (Sigma Aldrich, St. Louis, MO), and 6 mM solution of sodium azide (NaN_3, Sigma Aldrich, St. Louis, MO).

5.3.2 Microfabrication

Microfluidic devices were molded from silicon wafers (University Wafer, Boston, MA) carrying a negative photoresist SU-8 3010 (MicroChem, Newton, MA) pattern. The pattern was designed using Draftsight (Dassault Systèmes, Velizy Villacoublay, France) and printed on a photomask (CAD/Art Services, Inc., Bandon, OR). The silicon wafers were first rinsed with acetone (Fisher Scientific, Pittsburgh, PA) and isopropylalcohol (IPA, Fisher Scientific, Pittsburgh, PA) to remove any residue. They were then dried with N_2 and placed on a hotplate at 200° C for 10 min to remove all remaining moisture. The wafers were next plasma etched (Technics West, Inc., Anaheim, CA) under Oxygen at a pressure of 0.475 Torr and voltage of 400 mV for 5 min. After plasma etching, approximately 6 mL of SU-8 3010 photoresist was spin coated (Weinview, St. Louis, MO) onto the wafer at 2000 rpm for 30 s with an acceleration of 300 rpm/sec. The wafers with photoresist were then soft baked for 6 min at 95 ° C. A mask aligner (EV Group, Albany, NY) was used to expose the photoresist at 130 mJ/cm^2 to transfer the pattern from the transparency to the photoresist coated wafer. The exposed silicon wafers were baked for 3 min at 95 ° C and submerged in developer (Weinview, St. Louis, MO) for approximately 6 minutes. Wafers underwent a final hard bake for 30 min at 200 ° C.

All microfluidic experiments were performed in polydimethylsiloxane (PDMS, Dow Corning, Midland, MI) devices. PDMS was mixed in a 10:1 ratio of elastomer to curing agent, degassed, and poured over the silicon master. The masters and PDMS solution were baked at 70° C, until the PDMS was completely hardened. The PDMS was cut and pealed from the master and cut into individual devices in a clean room to prevent dust from settling on the PDMS surface. Holes were then punched at the inlet and outlet ports using a 0.75 mm inner diameter hole punch (Ted Pella, Redding, CA). The PDMS devices along with coverslips (Gold Seal, Corning, NY) were plasma etched under oxygen at a pressure between 0.3 to 0.4 Torr and voltage between 30 and 35 mV for precisely 45 s. After bonding the PDMS to the glass coverslip, the devices were placed in an oven for approximately 10 min at 70° C.

5.3.3 Microfluidics and Fluorescence Microscopy

Prior to experimentation, a 10 mg/mL Pluronic® solution was injected into the channel. The Pluronic® solution was left for 1 hr to coat the PDMS and prevent adsorption of the experimental sample to the PDMS walls. The 10 mg/mL solution was flushed from the channel by a 2.5 mg/mL Pluronic® solution. The 2.5 mg/mL Pluronic® solution was pumped into the channel at approximately 0.8 psi for approximately 1 hr.

After the high concentration Pluronic® solution was flushed from the microfluid device, each of two experimental samples (one fluorescent, one non-fluorescent) was injected into 1 of the 2 entry ports (Fig. 5.1). The air pressure forcing each sample into the device was adjusted so that the interface between the fluorescent and the non-fluorescent samples rested in the middle of the channel. The pressures were then slowly decreased, the interface kept in the middle of the channel, until significant diffusion of the fluorescent sample across the channel was clearly visible and gradual over the length of the channel (Fig. 5.2). Final experimental pressures fell between 0.2 psi and 0.4 psi. flow rate was found by simply marking the outlet tubing at the beginning and end of the experiment. A stopwatch was used to time the experiment. Readings were taken every 0.5 cm down the channel for 3 cm. 250 frames were taken using a 12-bit CCD camera (ORCA-ER, Hamamatsu, Japan) on a Axiovert 200M with LSM 5 confocal laser scanning microscope (Zeiss, Germany) with a 10× objective and 2.4× zoom to yield a frame rate of 0.64 fps and 1.15 μm/pixel. Confocal experiments employed a 10-350 mW 488nm (blue) laser (Melles Griot, Carlsbad CA) to excite fluorescent colloids. Image

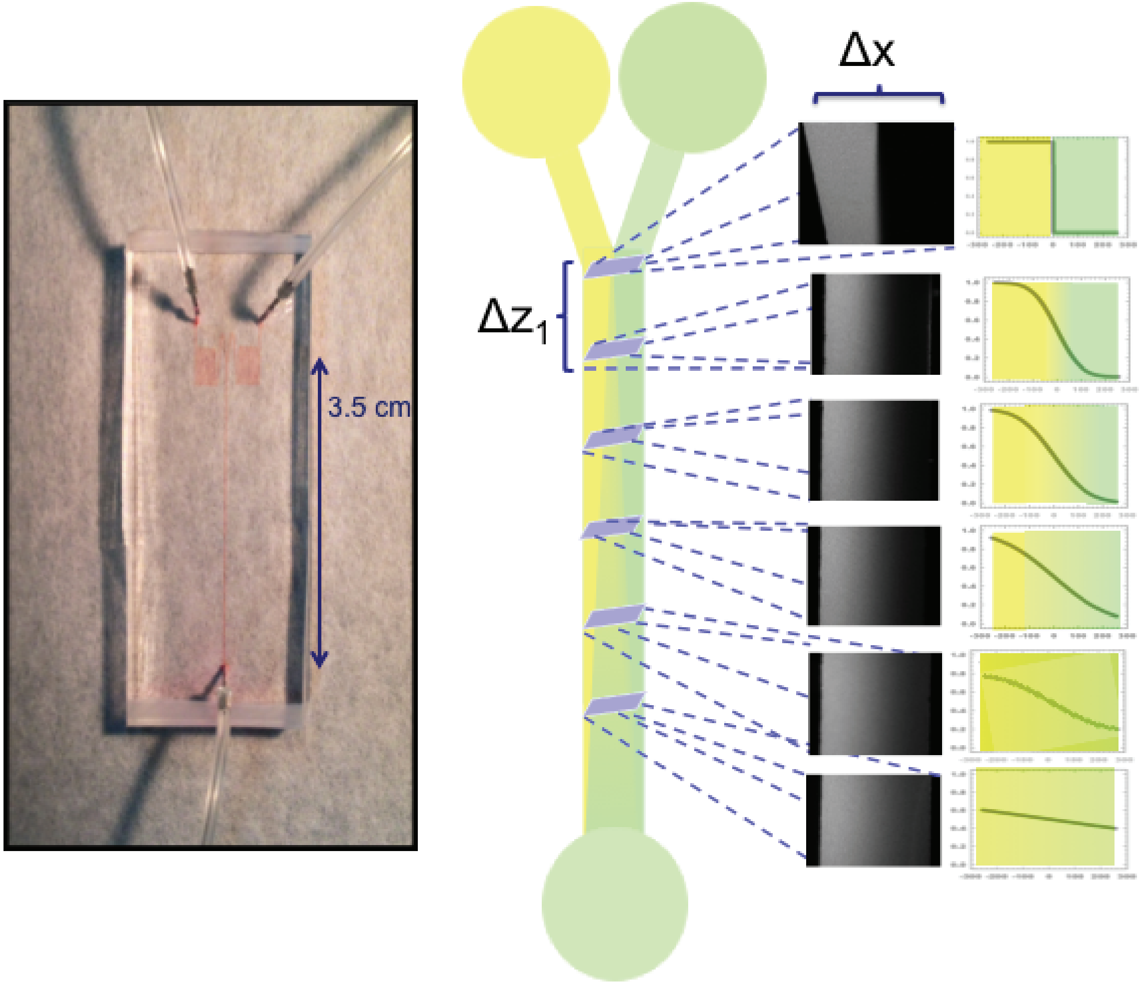

Figure 5.2 Images and diagram of the microfluidic device used to measure fluorescence diffusion. From left to right: Image of the PDMS device without magnification with tubing inserted into the inlets and the outlet. Red liquid injected into the channel makes the entire channel visible. A series of curves, visible at each inlet, increases the resistance within the channel, facilitating slower flow rates. The diagram (middle) shows fluorescence diffusion across the channel with viewing points along the length of the channel. To the right of each viewing window is a corresponding 24 × magnification image taken *via* fluorescence confocal microscopy adjacent to a graph showing the progression of intensity curves along the length of the channel.

analysis algorithms coded in FORTRAN were used to calculate the average intensity across the channel over 250 frames.

5.3.4 Experimental Analysis

Figure 5.3 shows the analysis of fluorescence diffusion across a microfluidic channel. The fluorescence intensity was measured across the channel at the top, middle, and bottom of every image (Fig 5.3a) and averaged over a 10 pixel wide strip. Those three intensities were each averaged over a 250 image sequence. The raw intensity was plotted with respect to pixels across the image (Fig 5.3b) and aligned with the channel edges according to guidelines drawn using the original image. The integral of the intensity over the entire curve was taken 20-30 pixels from both walls to eliminate edge affects from the analysis. The maximum and minimum intensities were determined using the intensity plot as a guideline. Since the interface was in the center of the channel, the ratio of the area under the intensity curve to the area in the box bounded by the maximum and minimum intensities and the channel edges was 1:2. This ratio was used to precisely tune the maximum and minimum intensities and the channel edge locations. A target drawn on the graph indicating the interface at the midpoint of the channel and the midpoint of the maximum and minimum intensities was used to indicate alignment of the interface in relation to the center of the channel. The target consistently fell precisely on the curve.

Diffusion of the fluorescent material across the channel means that after the initial channel junction, the concentration was not as high or as low as the absolutely maximum for minimum intensities, respectively, at any point across the channel.The difference between the image intensity minimum and maximum farther down the channel and the absolute intensity minimum and maximum was determined using the difference between intensity minimum inside the channel and the intensity minimum outside of the channel

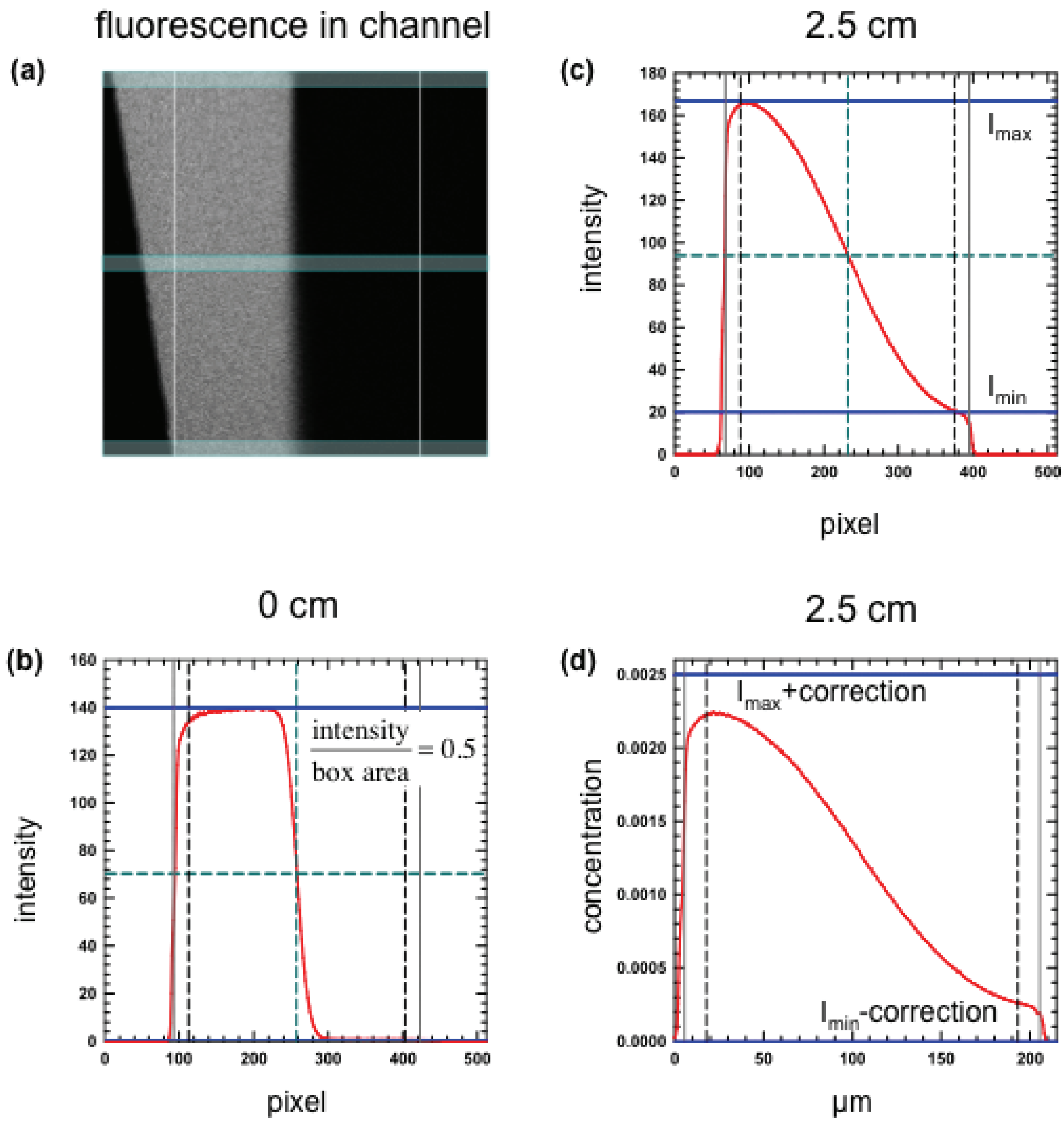

Figure 5.3 Analysis of fluorescence diffusion across a microfluidic channel. (a) shows an experimental image collected *via* confocal fluorescence microscopy. The fluorescence intensity is measured across the channel at the top, middle, and bottom of every image and averaged over a 10 pixel wide strip, as shown by the green rectangles. Those three intensities are each then averaged over a 250 image sequence. (b) the raw intensity is plotted with to respect to pixels across the image, shown by the red line. Guidelines drawn on the original image (white in original image and grey in graphical representation) are used to determine the edges of the channel and align the image. The integral of the intensity over the entire curve was taken 20-30 pixels from both walls, shown by the black dashed lines, to eliminate edge affects from the analysis. The dark blue lines show the maximum and minimum intensities. The ratio of the intensity integral

to the area in the box bounded by the maximum and minimum intensities and the channel edges was used to precisely tune the maximum and minimum intensities and the channel edge locations. The aqua dashed lines indicate the midpoint of the channel and the average intensity and consistently fell precisely on the curve. (c) shows the graph of the image intensity 2.5 cm down the channel. The blue line corresponding to I_{min} shows the difference between the intensity minimum inside the channel and the intensity minimum outside of the channel, used to relate the image intensity minimum and maximum and the absolute intensity minimum and maximum. After calibrating the graphs according the ratio between the integral of the fluorescence intensity curve and the integral of the fluorescence intensity curve at 0 cm, the curve was replotted (d) as a function of concentration, related to the absolute maximum and minimum concentrations, with respect to distance across the channel.

(Fig 5.3c). Due to conservation of mass, the same amount of fluorescent material had to be present in the channel at every point down the channel. As a result, the ratio between the overall intensity at any point down the channel, found by taking the integral under the curve, and the overall intensity at the entrance of the channel could be used to calibrate image intensity at every point down the channel, thus eliminating intensity differences due to microscope settings or photobleaching at the edge of the channel. After calibrating the graphs, the curve was replotted as a function of concentration (Fig 5.3d) related to the absolute maximum and minimum concentrations.

5.4 Results and Discussion

5.4.1 Gradient Diffusion in Colloidal Systems

Fig. 5.4 shows the gradient diffusion of dilute protein and particle colloidal systems. The colloidal systems studied were BSA protein, ConA protein, 47nm polystyrene particles physiadsorbed with BSA protein, and 47nm polystyrene particles physiadsorbed with pluronic polymer. Each graph shows the degree of gradient diffusion of fluorescent polystyrene physiadsorbed with PEO copolymer (5.4c). Data collected experimentally at different locations down the channel is shown using differently colored

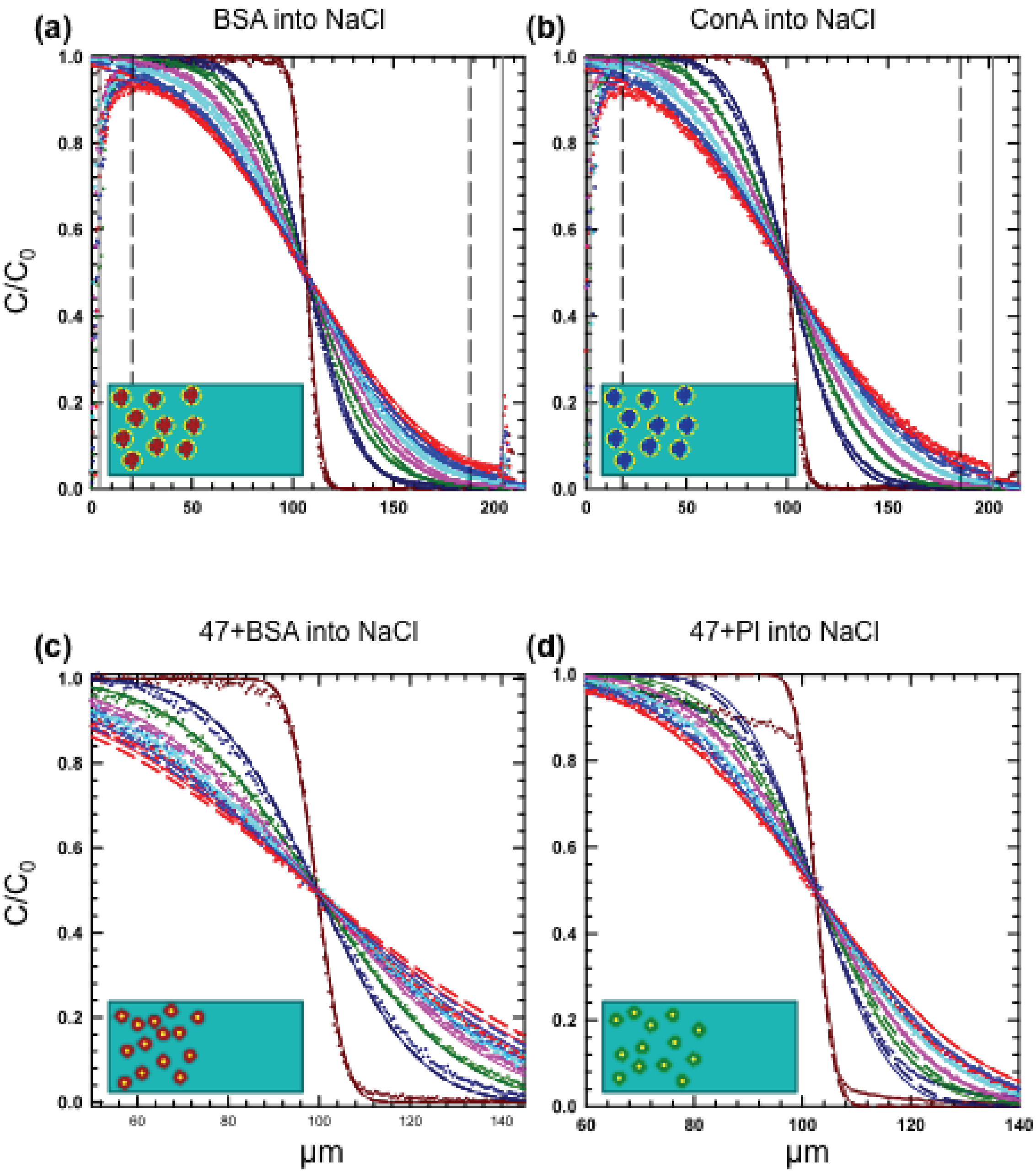

Figure 5.4 Graphs of gradient diffusion of fluorescent colloids. For every graph, the colored points represent experimental data collected at different distances down the channel. Dark red corresponds to experimental data collected at 0 cm, dark blue corresponds to measurements at 0.5 cm, green corresponds to measurements at 1 cm, pink corresponds to measurements at 1.5 cm, cyan corresponds to measurements at 2 cm, blue corresponds to measurements at 2.5 cm, and red corresponds to data collected at 3 cm. The solid colored lines show the diffusion data generated *via* Comsul for parameters equivalent to the parameters used to generate the experimental data with the matching

color. The dashed lines show the fits generated usinganalytical theory for diffusion from one semi-infinite solution into another and parameters equivalent to those used to generate the experimental and Comsol data bearing the same color. (a) shows the diffusion of fluorescent BSA into an NaCl solution.The grey solid lines mark the edges of the channels.The black dashed lines mark the left and right edges of the region analyzed.(b) shows the gradient diffusion of fluorescent ConA into an NaCl solution.The grey solid lines mark the edges of the channels.The black dashed lines mark the left and right edges of the region analyzed. (c) shows the gradient diffusion of fluorescent BSA coated 47 nm colloids into an NaCl solution.Due to slower rate of diffusion, the graph focuses on the interface. (d) shows the gradient diffusion of fluorescent Pluronic coated 47 nm colloids into an NaCl solution. The graph focuses on the interface.Insets depict the gradient colloidal diffusion of each system according to the schematics in Fig 1.

points. Each color corresponds to a different distance at intervals of 0.5 cm. As the distance down the channel and, as a corollary, time increases, more fluorescent material has diffused across the channel and the slope at the interface decreases. Dark red corresponds to experimental data collected at 0 cm. The solid colored lines show the diffusion data generated *via* Comsul for channel and flow parameters equivalent to the parameters used to generate the experimental data with the matching color. The dashed lines show the analytical fits for gradient diffusion generatedfrom solutions to Fick's second law for diffusion from one semi-infinite solution into another and parameters equivalent to the parameters used to generate the experimental and Comsol data with the same color (Table 5.1).

As shown by Fig. 5.3, exceptional agreement was observed between the experimental and Comsol data and the analytical solutions. At long times the experimental results deviate from analytical solutions. The analytical solution assumes that diffusion takes place across an interface between two semi-infinite solutions, while the actual solutions are confined in a channel. In analyzing the data, the colloidal solutions were assumed sufficiently dilute to render interactions between colloids

Table 5.1 Experimental parameters used to calculate the experimental diffusivity (Eq (5.7)) used to calculate the gradient diffusion coefficient (Fig. 5.2), long time self diffusion coefficient (Fig. 5.3), and diffusion into mucus in Fig. 5.4.The hydrodynamic radii calculated from the diffusivity (Eq (5.6) were compared with hydrodynaimc radii from literature, as shown in Fig. 5.5.

Colloidal system	***Q*** **(μL/min)**[1]	***D*** **(m^2/s)**[2]	**a_{SE}(nm)**[3]	**a_M(nm)**[4]	**ϒ***[5]
BSA into NaCl	0.327	6.01×10^{-11}	4[6]	4	1
BSA into BSA	0.281	4.81×10^{-11}	4	5	1.25
ConA into NaCl	0.253	4.81×10^{-11}	5	5	1
ConA into ConA	0.288	5.01×10^{-11}	5	5	1
47nm + BSA into NaCl	0.053	6.49×10^{-12}	35	37	1.06
47nm + BSA into 47nm + BSA	0.089	4.37×10^{-12}	35	55	1.53
47nm + pluronic into NaCl	0.179	5.05×10^{-12}	37	34	0.919
47nm + pluronic into 47nm + pluronic	0.1	5.05×10^{-12}	37	34	0.919
mucus into NaCl	0.008	N.A.	N.A.	N.A.	N.A.
BSA into mucus	0.064	3.00×10^{-11}	4	8	2
ConA into mucus	N.A.	N.A.	5	N.A.	N.A.
47nm + BSA into mucus	0.034	N.A	35	105	3
47nm + pluronic into mucus	0.041	7.07×10^{-12}	37	34	0.919

1. Measured
2. Fit *via* graphical analysis
3. Based on literature value
4. Calculated from diffusivity
5. Ratio of measured radius to Stokes-Einstein radius literature value
6. Calculated from gel chromatography[101]

negligible. Table 5.2 shows the expected relationship between the measured diffusion based on the colloidal dispersion concentration (Eq. (5.7)), and diffusion based on the

Stokes-Einstein equation. Every dispersion used was sufficiently dilute to neglect colloidal interactions between diffusing colloids. Table 5.1 shows the actual relationship between the measured hydrodynamic radius and the expected radius based on literature values. Overall, a high level of correlation between the experimentally generated values and literature based values was observed, verifying the experimental and analytical technique.

5.4.2 Long Time Self Diffusion in Colloidal Systems

Fig. 5.5 shows the long time self diffusion of dilute protein and particle colloidal systems. The colloidal systems studied were BSA protein (5.4a), ConA protein (5.4b), BSA physiadsorbed 47 nm polystyrene (5.4c), and 47 nm polystyrene physiadsorbed with PEO copolymer (5.4c). Each graph shows the degree of long time self diffusion of fluorescent material across the channel into equivalent nonfluorescent material at different distances down the channel. Data collected experimentally at different locations down the channel at 0.5 cm intervals is shown using differently colored points. Dark red corresponds to experimental data collected at 0 cm. The solid colored lines show the diffusion data generated *via* Comsul using the channel and flow parameters equivalent to parameters used to generate the experimental data. The dashed lines show the fits generated using an analytical fit to Fick's second law for diffusion from one semi-infinite solution into another and for the time and stokesian radii used to generate the matching experimental and Comsol data (Table 5.1).

As shown graphically (Fig. 5.5), exceptional agreement was observed between the experimental and Comsol. The colloidal dispersions were again sufficiently dilute to ignore interactions between thethe dispersants (Table 5.2). When fit to equation (5.11),

Table 5.2 Parameters used to calculate relationship between diffusivity based on colloidal concentration and diffusivity based on the Stokes-Einstein equation.

Colloidal system	**Concentration (mg/mL)**[7]	ϕ [8]	**K(Φ)**	**Z(Φ)**	$\frac{D(\phi)}{D_0 \times \partial\phi}$
BSA into NaCl	2	4.86×10^{-3}	0.968	1.02	0.987
BSA into BSA	2	4.86×10^{-3}	0.968	1.02	0.987
ConA into NaCl	3	1.18×10^{-2}	0.923	1.05	0.966
ConA into ConA	3	1.18×10^{-2}	0.923	1.05	0.966
47nm + BSA into NaCl	N.A.	0.001	0.993	1.00	0.997
47nm + BSA into 47nm + BSA	N.A.	0.002	0.987	1.01	0.995
47nm + pluronic into NaCl	N.A.	0.002	0.987	1.01	0.995
47nm + pluronic into 47nm + pluronic	N.A.	0.002	0.987	1.01	0.995
mucus into NaCl	2	NA	NA	NA	NA
BSA into mucus	2	4.86×10^{-3}	0.968	1.02	0.987
ConA into mucus	3	1.18×10^{-2}	0.923	1.05	0.966
47nm + BSA into mucus	N.A.	0.002	0.987	1.01	0.995
47nm + pluronic into mucus	N.A.	0.002	0.987	1.01	0.995

7. Measured
8. Calculated based on measured concentration or manufacturer's estimate

the diffusivity and hydrodynamic radius calculated from the experimental results had excellent consistency with values from the literature (Table 5.1). The high level of

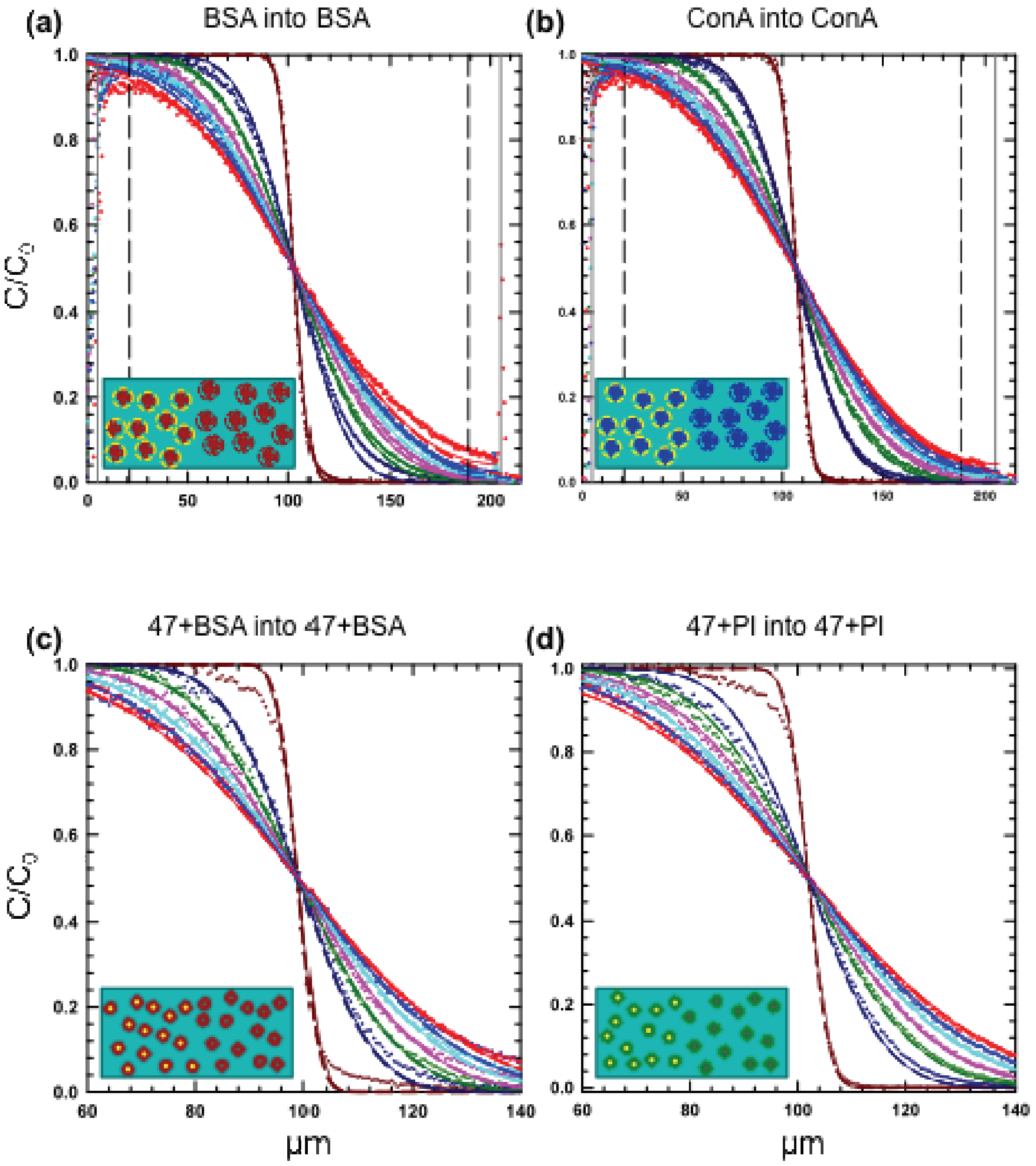

Figure 5.5 Graphs of long time self diffusion of fluorescent colloids. For every graph, the colored points represent experimental data collected at different distances down the channel. Data points and lines are plotted with the same representations as in Fig. 5.4. (a) shows the long time self diffusion of BSA. (b) shows the long time self diffusion of ConA. (c) shows the long time self diffusion of BSA coated 47 nm colloids. Due to slower rate of diffusion, the graph focuses on the interface. (d) shows the long time self diffusion of Pluronic coated 47 nm colloids. The graph focuses on the interface. Data points and lines are plotted with the same representations as in Fig. 5.4. Insets depict the gradient colloidal diffusion of each system according to the schematics in Fig 5.1.

correlation between the experimental and Comsul generated data as well as the theoretical solution to Fick's second law support the analytical solution selected to describe the data.

5.4.3 Colloidal Diffusion into a Mucus Solution

Fig. 5.6 shows the gradient diffusion of dilute protein and particle colloidal systems into a dilute mucus suspension. The colloidal systems studied were BSA protein (5.6a), PEO copolymer physiadsorbed 47 nm polystyrene particles (5.6b), and BSA physiadsorbed 47 nm polystyrene particles (5.6c). Graphs for BSA protein, ConA protein, PEO copolymer physiadsorbed 47 nm polystyrene (5.6c) show the degree of gradient diffusion of fluorescent material across the channel into a dilute mucus dispersion at different distances down the channel. Data collected experimentally at different locations down the channel at 0.5 cm intervals is shown using differentlycolored points, with dark red corresponding to experimental data collected at 0 cm. The solid, colored lines show the diffusion data generated *via* Comsul using the channel and flow parameters equivalent to parameters used to generate the experimental data. The dashed lines show the fits generated using an analytical fit to Fick's second law for diffusion from one semi-infinite solution into another. The time and Stokesian radii used to generate the matching experimental and Comsol data (Table 5.1).

Mucus dilution could not be accurately calculated (Table 5.2) due to heterogeneity in physicochemistry between between mucin samples. Mucus was dissolved at 2.5 mg/mL, which was the maximum solubility for that particular batch of mucin, excluding the use of heat or a sonic horn to increase solubility. Still, this

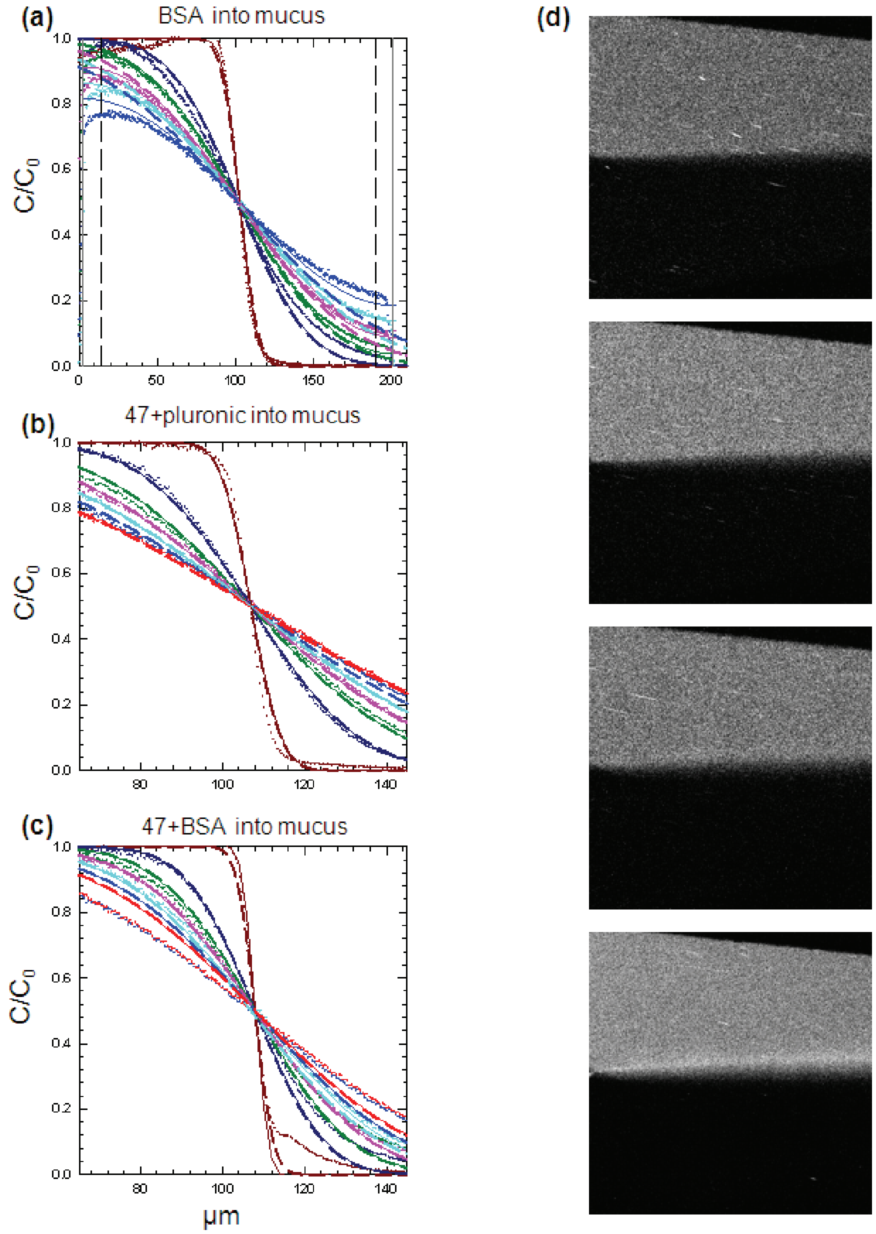

Figure 5.6 Graphs of gradient diffusion into a mucin suspension. For every graph, the colored points represent experimental data collected at different distances down the channel. Data points and lines are plotted with the same representations as in Fig. 5.4. (a) shows the diffusion of BSA protein into mucin suspension. (b) shows the diffusion of PEO physiadsorbed 47 nm polystyrene particles into mucin suspension. (c) shows the diffusion of BSA physiadsorbed 47 nm polystyrene particles into mucin suspension. Data points and lines are plotted with the same representations as in Fig. 5.4. Insets depict the gradient colloidal diffusion into mucus for each system according to the schematics in Fig 5.1. (d) shows time lapse images over 8 min of the ConA-mucus solutions at the channel junction. Fluorescent ConA-mucus aggregation can be seen at the interface.

concentration was slightly less than concentrations found in literature leading to physical entanglement between mucins, and only ¼ of the concentration found to induce gelation. As large variation exists in the solubility of mucins between sample batches, literature-based predictions for mucin behavior related to solutibilty could only be used as guidelines. In experiments testing the gradient diffusing of fluorescently-tagged mucins, virtually no diffusion was observed even at very long times. Since the concentrations used were significantly below concentrations necessary for gelation, the mucin polymers were most likely physically entangled.

As shown by Fig. 5.6a, exceptional agreement was observed between the experimental and Comsol data for BSA diffusion into mucus. At long times, the analytical solution deviated from the Comsol experimental data. As described above, the analytical solution to Fick's second law deviates from experimental data at long times due to the boundary condition that material was diffusing from one semi-infinite solution instead of diffusing within confined spaces. The diffusivity and hydrodynamic radius values calculated from experimental results showed significant deviation from Stokes radii previously calculated for BSA (Table 5.1). Inconsistency between the hydrodynamic radii calculated by fitting an analytical solution to Fick's second law to experimental data and values observed *via* gradient diffusion of BSA into an NaCl solution indicated that a different diffusion model may be required to accurately describe interactions between BSA proteins and mucin polymer.

Fig. 5.6b shows diffusion of PEO copolymer physiadsorbed 47 nm polystyrene particles into mucus. Exceptional agreement was observed between the experimental and Comsol data. The diffusivity and hydrodynamic radius values calculated from experimental results matched the Stokes radii previously calculated for PEO copolymer physiadsorbed 47 nm polystyrene particles (Table 5.1). Excellent correlation was observed between the hydrodynamic radii calculated by fitting an analytical solution to Fick's second law to experimental data and literature-based values. This indicates that the deviation from the analytically-predicted diffusivity for BSA through mucus was likely due to specific interactions between BSA protein and mucins instead of purely osmotic or hydrodynamic effects.

Fig. 5.6c shows diffusion of BSA physiadsorbed 47 nm polystyrene particles into mucus. Experimental data showed significant deviation between experimental data and data collected *via* the Comsol model. The model could be made to fit experimental data collected between 0 - 2 cm and could not be made to fit experimental data collected at 2.5 and 3 cm. In addition, the observed Stokes radius was three times larger than the radius observed from gradient diffusion experiments (Table 5.1). The high degree of deviation between the hydrodynamic radii calculated by fitting an analytical solution to Fick's second law to experimental data and values observed for gradient diffusion of BSA physiadsorbed 47 nm polystyrene particles into an NaCl solution confirm that a different model is required to accurately describe diffusion of BSA into mucus.

Fig. 5.6d shows time-lapse images of the channel junction between a mucin dispersion and a ConA solution. As material flowed into the channel over time, aggregation of fluorescent material could be observed at the interface between the two colloidal dispersions. As ConA carries a large positive electrostatic charge and has been observed in literature to bind tightly to mucins, this aggregation was expected.

Fig. 5.7 shows a direct comparison of measured Stokes radii, diffusivities, and γ^* for BSA protein, ConA protein, PEO copolymer physiadsorbed 47 nm polystyrene particles, and BSA physiadsorbed 47 nm polystyrene through calculations of gradient diffusion into NaCl solution, long time self diffusion, and gradient diffusion into mucus suspension. The graph shows that gradient and self diffusion of BSA protein, ConA protein, PEO copolymer physiadsorbed 47 nm polystyrene particles, and BSA copolymer physiadsorbed 47 nm polystyrene particles consistently agreed with the hydrodynamic radii calculated by fitting an analytical solution to Fick's second law to experimental data and literature-based values. Long time self diffusion of BSA copolymer physiadsorbed 47 nm polystyrene particles were observed to have a slightly larger γ^* of 1.53. As the second virial coefficient of BSA is largly dependent on ionic strength, a small amount of experimental error in mixing the solutions used to measure this particularly diffusivity would have the highest impact on experimental calculations. Large deviation from previously observed Stokes radii were observed only for gradient diffusion of BSA protein and BSA copolymer physiadsorbed 47 nm polystyrene particles, indicating that the deviation from the analytically-predicted diffusivity for BSA through mucus was likely due to specific interactions between BSA protein and mucins instead of purely osmotic or hydrodynamic effects. Consistency in the Stokes radius values observed for gradient diffusion of PEO copolymer physiadsorbed 47 nm polystyrene particles into NaCl and into mucus indicate that deviations observed in BSA diffusion are indeed due to specific interactions between BSA proteins and mucin polymer.

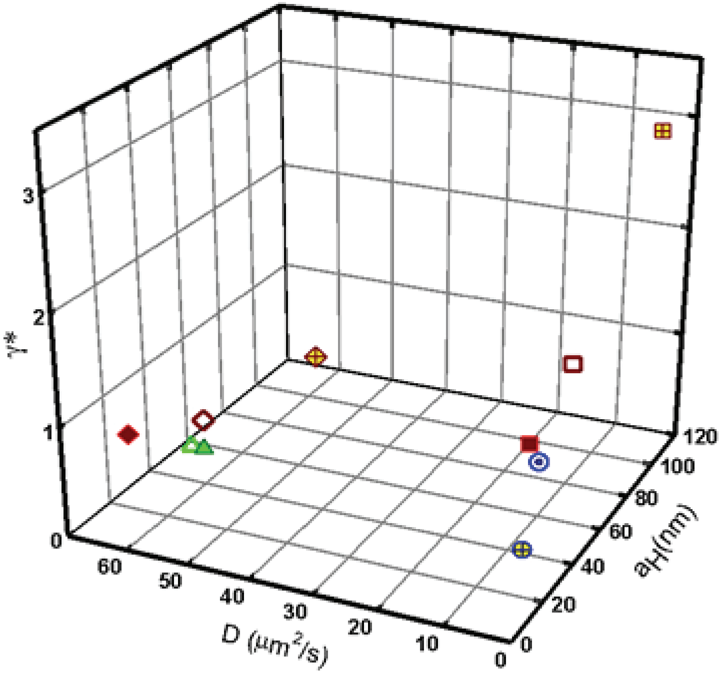

Figure 5.7 shows a direct comparison of measured Stokes radii, diffusivities, and γ* for BSA protein, ConA protein, PEO copolymer physiadsorbed 47 nm polystyrene particles, and BSA physiadsorbed 47 nm polystyrene particles through calculations of gradient diffusion into NaCl solution, long time self diffusion, and gradient diffusion into mucus suspension. Closed symbols correspond to gradient diffusion. Open symbols correspond to long time self diffusion. Crossed symbols with a yellow interior correspond diffusion into mucin suspension. Dark red diamonds correspond to BSA protein, green triangles correspond to ConA protein, dark red squares correspond to BSA physiadsorbed 47 nm polystyrene particles, and blue circles correspond to PEO copolymer physiadsorbed 47 nm polystyrene particles.

Published studies of BSA diffusion through mucus gel showed variation in measured rates of diffusion, but generally found that BSA diffusion was not significantly slowed by the presence of mucus gel. Experiments described in chapter 4 also indicated that BSA should not adsorb to mucus and would be a likely candidate for rapid diffusion through mucus. Diffusion rates of the colloidal probes through mucus were affected by the difference in chemical and physical mucin conformation. In contrast to the entangled mucin suspension used for these experiments, gelled mucus forms large pores and likely "hides" hydrophobic groups more effectively from the highly hydrated pores through which BSA proteins or BSA physiadsorbed particles would pass. BSA contains a hydrophobic binding pocket that would likely interact with any exposed mucin hydrophobic groups, slowing diffusion.

5.5 Conclusion

PEO copolymer physiadsorbed DDPs and BSA physiadsorbed DDPs were identified in previous experiments as potentially capable of rapidly penetrating the pulmonary mucosal layer. It was hypothesized that BSA, BSA physiadsorbed 47nm particles, and PEO coplymer physiadsorbed 47nm particles could act as stealth drug delivery particles, efficiently diffusing through mucus. PEO coplymer physiadsorbed 47nm particles behaved as predicted; maintaining the same diffusion rate for gradient diffusion, long time self diffusion, and diffusion into a mucus suspension. Instead of behaving as stealth vectors, diffusion of BSA and BSA physiadsorbed particles were significantly slowed by the mucin suspension. While it could be inferred from the result that specific interactions between BSA and mucins lead to, sufficient evidence does not exist to support this conclusion.

The chemical and physical mucin conformation is the primary determinant of whether a pathogen or a DDP will penetrate the mucosal layer. While gelled mucus forms large pores and likely "hides" hydrophobic groups, entangled mucins behave as individual polymers. As an entangled polymer network, the mucin suspension would lack pores and would have a higher proportion of naked hydrophobic groups. BSA contains a hydrophobic binding pocket that would likely interact with any exposed mucin hydrophobic groups, slowing diffusion. At the Debye length in these experiments, <1 nm, hydrophobic interactions would mitigate any potential effect of the charge conformation in the BSA polymer or the BSA coating.

In addition to gaining important insight into the diffusion of drug delivery particles through mucus, a novel and powerful technique was developed to conduct these experiments. The consistency between the experimental data, Comsol data, and analytical fits demonstrates that the superior precission attained through using a constant pressure microfluidic system combined with powerful, highly accurate analysis techniques. In these experiments gradient diffusion, long time self diffusion, and interdiffusion were all characterized with unprecedented accuracy. The analysis tools demonstrated in this paper could be easily extended to describe a wide array of colloidal phenomena.

6. CONCLUSION

In preparing this dissertation, the physical as well as hydrodynamic properties of mucus and the colloidal forces that affect the diffusion of potential drug delivery vectors through mucus were investigated. It was hypothesized that specific interactions between mucin polymers and virus-mimicking polymers would increase the rate of diffusion through mucus of the DDP's studied. In particular, DDP outer coatings that had coexistance of positive and negative charges, as is present in the outer coatings of capsid viruses, were investigated. A comprehensive understanding of thermodynamic and hydrodynamic interactions between potential drug delivery particle polymeric coatings and mucus is essential to the development of effective pulmonary drug delivery vectors.[11,17]

In order to identify potentially effect pulmonary DDP coatings, various types of virus-mimicking colloidal particles were levitated over a mucus layer and their potential energy and hydrodynamic interactions measured using TIRM in conjunction with BIA. Total Internal Reflection Microscopy was used to identify DDP's that experienced small scale attraction with a mucus layer without binding. This work utilized Brownian colloidal probes functionalized with mucus or virus-mimicking polymers to measure thermodynamic and hydrodynamic properties within the layers as well as conservative and dissipative forces between the polymer-coated colloidal probes and mucin polymers and gels.

Methodically analyzing various combinations of asymmetric brush interactions gave insight into specific and nonspecific interactions between DDP brush coatings and a mucin brush layer. PEO copolymer physiadsorbed DDPs were found to interact with the mucin layer *via* strong steric repulsion and physical interpenetration into the mucin layer. Stabilizing steric repulsive forces existed between BSA protein physiadsorbed DDPs, though to a lesser extent. The BSA coating on BSA protein physiadsorbed DDPs was observed to interact with a mucin brush layer via small scale, specific, electrostatic interactions.

DDPs physiadsorbed with positively and negatively charged polyelectrolyte polymer multilayers were found also to carry the coexistance of positive and negative charges on the outer polymer layer. Polyelectrolyte polymers were found to physiadsorb to the particle surface in a loose conformation with dangling loops and polymer chains. DDPs physiadsorbed with polyelectrolyte polymer interacted with the mucin layer *via* stabilizing steric interactions in addition to specific electrostatic interactions and penetration of the dangling polyelectrolyte polymer loops and chains into the mucin brush layer. Through the interpenetration between the physiadsorbed polyelectrolyte polymer layer and the physiadsorbed mucin polymer layer, tethers formed and bound the DDPs physically or electrostatically to the mucin layer. A low concentration of negatively charged PSS polymer in the outer polyelectrolyte layer lead to destabilizing electrostatic attraction between mucus and negatively charged PAH polymer in the bottom polyelectrolyte layer. A high concentration of negatively charged PSS in the outer polyelectrolyte layer lead to destabilizing physical polymer bridging between dangling chains in the polyelectrolyte and mucin layers. BSA protein physiadsorbed DDPs were stabilized by specific electrostatic interactions between DDP coating and mucus. While DDPs physiadsorbed with polyelectrolyte polymer were destabilized by electrostatic interactions, BSA physaiadsorbed DDPs remained stable due to the small size scale of separation between the charges in the outer polymer layers. This work gave insight into interactions between polymer brushes, as well as the conformation and behavior of adsorbed mucus brush layers and potential DDPs.

A universally applicable exponential equation was developed that fit Milner's equation for steric interactions for parabolic brush layers in order to obtain symmetric and asymmetric steric potentials. Bayesian Inference analysis used the Smoluchowski equation to simultaneously measure thermodynamic (*i.e.*, free energy) and hydrodynamic properties (*i.e.*, diffusivity) properties of the interacting polymer brushes. In addition to measuring and analyzing interactions between potentially effective pulmonary drug delivery vectors and mucus, these analytical techniques are widely applicable and can be used to give insight into a wide array of polymer brush interactions. An analytical model relating physicochemical and hydrodynamic properties of mucus solutions to DDP diffusion was necessary to analyze the specific and nonspecific interactions between polymeric brushes and did not previously exist.

After identifying PEO copolymer physiadsorbed DDPs and BSA physiadsorbed DDPs as potentially capable of rapidly penetrating the pulmonary mucosal layer, the rate of diffusion through mucus was measured for these virus-mimicking DDPs along with BSA and ConA protein. It was hypothesized that ConA would adsorb to mucus while BSA, BSA physiadsorbed 47nm particles, and PEO coplymer physiadsorbed 47nm particles could act as stealth drug delivery particles, efficiently diffusing through mucus. While ConA and PEO copolymer physiadsorbed particles behaved as predicted, BSA and BSA physiadsorbed particles were significantly slowed by the mucin suspension. This result could indicate that the specific interactions between BSA and mucins lead to binding instead of stabilization along with a small level of attraction. BSA binding to mucus would be contrary to the results of experiments conducted *via* TIRM and analysis of specific polymer brush interactions. A more likely alternative is that the chemical and physical mucin conformation of the mucin suspension was different from the conformation of the mucin polymer brush previously analyzed and from wild type mucus.

Physical and chemical interactions between DDPs and mucus are the primary determinant of whether a pathogen or a DDP will penetrate the mucosal layer. A relatively low concentration of mucins was dissolved in the suspension utilized to measure DDP diffusion through mucus. The mucins were likely entangled instead of gelled. While gelled mucus forms large pores and likely "hides" hydrophobic groups, entangled mucins behave as individual polymers. As an entangled polymer network, the mucin suspension would lack pores and have a higher proportion of naked hydrophobic groups. BSA contains a hydrophobic binding pocket that would likely interact with any exposed mucin hydrophobic groups, slowing diffusion. At the Debye length in these experiments, <1 nm, hydrophobic interactions would mitigate any potential effect of the specific electrostatic interactions between BSA polymer or the BSA physiadsorbed DDP and mucus. Repeating these experiments with a larger group of proteins and with different concentrations of mucus would yield invaluable insight into specific and nonspecific interactions affecting DDP diffusion in mucus.

As with analysis of polymer brush interactions measured *via* TIRM, a novel and powerful technique was developed to measure the thermodynamic and hydrodynamic interactions between the DDP coatings and mucins suspension. A constant pressure microfluidic system was utilized to gather data with great precion. A novel analytical technique was developed to calculate gradient diffusion, long time self diffusion, and diffusion of DDPs into mucus suspension, yielding unprecedented accuracy and precision. In addition to gaining important insight into the diffusion of drug delivery particles through mucus, the powerful techniques developed here could have a huge impact on the understanding of various phenomena in colloidal science. Overall, the experiments described in this dissertation provide invaluable insight into the conservative and dissipative forces between virus-mimicking DDPs and mucus along with developing analytical and experimental techniques that could profoundly impact the understanding of various polymer brush and colloidal phenomena.

7. FUTURE RESEARCH

7.1 Capsid and Envelope Virus Interaction with Mucus

7.1.1 Bilayer Coated Colloidal Probe Interactions with Mucus

In chapter 4, interactions between dense particle brush layers and mucin mesh layers were analyzed. Extending these experiments to particles encapsulated in supported lipid barriers would give incredible insight into viral penetration of the mucosal barrier. Rapid mucosal penetration of capsid viruses compared to impenetrability of mucus to viruses enclosed in a lipid envelope has been widely observed but not explained.[3,8]

TIRM has previously been used to measure interactions between Cadherin protein and polyethylene glycol decorated supported lipid bilayer coated colloidal probes and bilayer or PEG coated walls.[30] Using TIRM and Bayesian inference analysis to study asymmetric interactions between differently decorated supported lipid bilayers and mucus could provide invaluable insight into the mechanism behind rapid mucosal penetration of viruses. Additionally, liposomes are a widely used mechanism for drug delivery. Direct of measurements between supported lipid bilayers and mucus could lead to development of mucopenetrating liposomes.

7.1.2. Virus Like Particles Interacting with Mucus

The study of interactions between virus like particles (VLPs) and mucus would also increase understanding of specific and nonspecific forces behind rapid mucopenetration. VLPs, fragmented viral proteins, are currently of great interest as potential drug delivery vectors. Specifically, fragmented Human Papilloma Virus

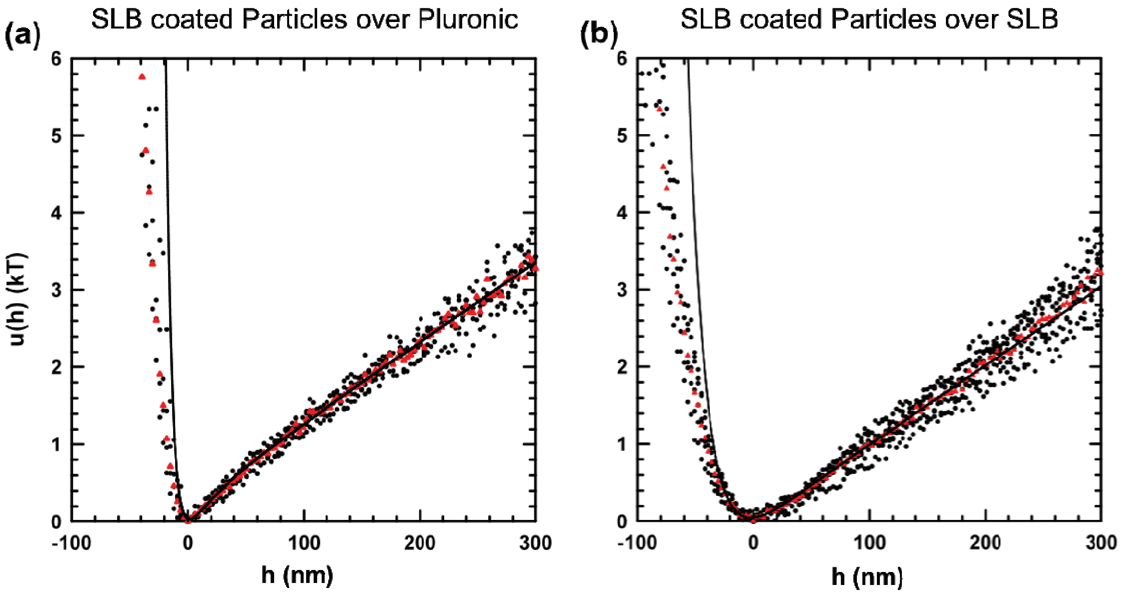

Figure 7.1 TIRM images of (a) 2.34 μm silica colloids encapsulated in supported lipid bilayer diffusing over PEO copolymer physiadsorbed wall. Black points show individual net potential energy with respect to height of individual particles. Red triangles correspond to the ensemble average net potential energy. The black line shows the theoretical fit to the ensemble average net potential energy. (b) 2.34 μm silica colloids encapsulated in supported lipid bilayer diffusing over lipid bilayer supported by a hydrophilic silica wall. Black points show individual net potential energy with respect to height of individual particles. Red triangles correspond to the ensemble average net potential energy. The black line shows the theoretical fit to the ensemble average net potential energy.

(HPV)-like proteins could also provide invaluable insight into the mechanism behind viral mucopenetration. HPVLPs could themselves form a highly effective DDP coating.

7.2 In Vitro and Ex Vivo models

7.2.1 Colloidal Probe Interactions with Gelled Mucus and Lung Epithelial Cells

Chapter 5 measured the diffusion of virus-mimicking DDPs through a mucin suspension. BSA and BSA physiadsorbed particles were found to bind to mucins *via* hydrophobic interractions with the suspension of entangled mucin polymers.

Hydrophobic interactions would likely be reduced by mucus gellation, a more physiologically relevant conformation. Measurement of protein diffusion through gelled mucus would provide insight into changes of mucus chemistry as mucus conformation changes. Additionally, measurement of gradient colloidal diffusion through porous media would be of significant interest colloidal scientists.

The study of BSA and PEO copolymer physiadsorbed DDPs interaction with human mucus-producing pulmonary epithelial cells extends the data collected through this dissertation to a relevant in vitro human model. Calu-3 pulmonary epithelial cells are a widely used cell model (Fig. 7.2) due to their formation of cilia and mucus. Grown at an air-liquid interface, cells secrete mucus after approximately 10 days in culture while cells grown at liquid-liquid interface do not form mucus. Interactions between DDPs and these cells could be studied in 3 phases: 1) cells grown at a liquid-liquid interface without mucus would show whether vectors could be accepted into cells to deliver their cargo, 2) cells grown at air-liquid interface prior to mucus secretion to investigate interactions between DDPs and ciliated cell surfaces under the least complex yet biologically relevant scenario 3) diffusion of DDPs over and into secreted mucus and possible penetration into pulmonary epithelial cells. Particle tracking codes used for TIRM analysis can be applied to analysis of DDPs over pulmonary epithelial cells to identify specific and nonspecific forces between DDPs and mucus or DDPs and cells. The use of dark field microscopy would facilitate individual tracking an analysis of differently coated nanoparticles.

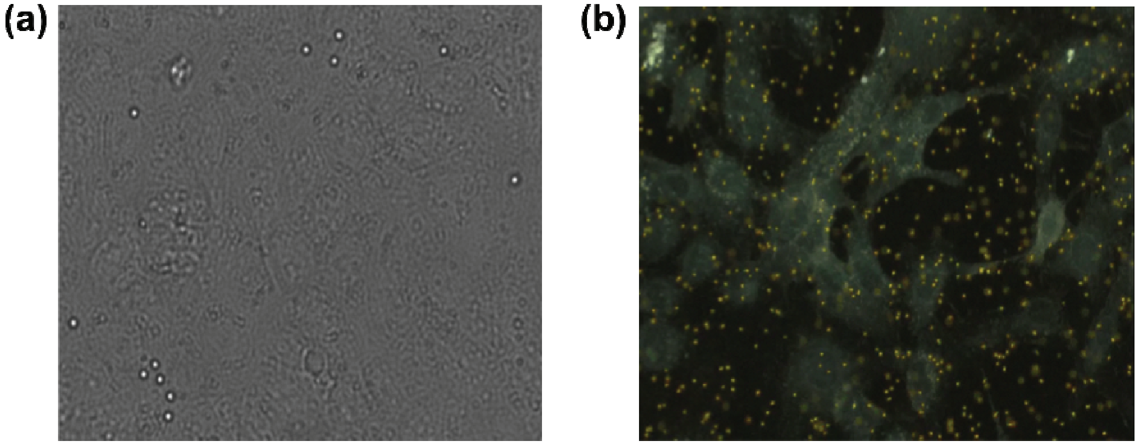

Figure 7.2 (a) 2.34 µm PEO copolymer-stabilized silica collids diffusing over confluent Calu-3 pulmonary epithelial cells grown at an air-liquid interfaces. All colloids were levated and diffused over the surface. Images were collected using an inverted microscope and 40X magnification (b) 400 nm gold nanoparticles diffusing over FKLV-3 carcinoma cells. Images were collected using dark field microscopy.

7.2.2 Diffusion Over and Into Diseased Mucus

Particle tracking and confocal fluorescence microscopy can be used to measurediffusion into excised mucin specimens. This could be used to develop directed drug delivery through diseased mucus. Likewise, by measuring specific interactions between drug delivery particle coatings and mucus, pulmonary drug delivery particles could be individually engineered to rapidly penetrate chemically or physically unique mucus specimens. Diseased mucus has different components not present in healthy mucus, including white blood cells, differing ammouts of cellular material and DNA, and pathogens. Identifying and controlling interactions between DDPs and mucus would lead to individualized medicine.

8. REFERENCES

1 Bansil, R. & Turner, B. S. in *Current Opinion in Colloid & Interface Science* Vol. 11 164-170 (Elsevier, 2006).

2 Cone, R. A. in *Advanced Drug Delivery* Reviews Vol. 61 75-85 (Elsevier, 2009).

3 Svensson, O. & Arnebrant, T. in *Current Opinion in Colloid & Interface Science* Vol. 15 395-405 (Elsevier, 2010).

4 Thornton, D. J., Rousseau, K. & McGuckin, M. A. in *Annual Review of Physiology* Vol. 70 459-486 (Annual Reviews, 2008).

5 Khanvilkar, K., Donovan, M. D. & Flanagan, D. R. in *Advanced Drug Deliver Reviews* Vol. 48 173-193 (Elsevier, 2001).

6 Cone, R. A. Vol. 3 43-64 (Academic Press San Diego, 1999).

7 Lai, S. K., Wang, Y.-Y. & Hanes, J. in *Advanced Drug Deliver Reviews* Vol. 61 158-171 (Elsevier, 2009).

8 Saltzman, W. M., Radomsky, M. L., Whaley, K. J. & Cone, R. A. in *Biophysical Journal* Vol. 66 508-515 (Elsevier, 1994).

9 Radomsky, M. L., Whaley, K. J., Cone, R. A. & Saltzman, W. M. in *Biomaterials* Vol. 11 619-624 (ACS Publications, 1990).

10 Dawson, M., Krauland, E., Wirtz, D. & Hanes, J. in. *Biotechnology Progress* Vol. 20 851-857 (AIChE, 2004).

11 Kirch, J. *et al.* in *PNAS* Vol. 109 18355-18360 (National Academy of Science, 2012).

12 Cu, Y. & Saltzman, W. M. in *Molecular Pharmaceutics* Vol. 6 173-181 (ACS Publications, 2008).

13 Institute, N. H. L. a. B. (NIH, 2012).

14 Lai, S. K., Wang, Y.-Y., Wirtz, D. & Hanes, J. in *Advanced Drug Deliver Rev.* Vol. 61 86-100 (Elsevier, 2009).

15 Peppas, N. A., Hansen, P. J. & Buri, P. A. in *International Journal of Pharmaceutics* Vol. 20 107-118 (Elsevier, 1984).

16 Peppas, N. A., Hansen, P. J. & Buri, P. A. in *International Journal of Pharmaceutics* Vol. 20 107-118 (Elsevier, 1984).

17 Hsu, T.-P., Ma, D. S. & Cohen, C. in *Polymer* 24 1273-1278 (Elsevier, 1983).

18 Lai, S. K., Wang, Y.-Y., Cone, R., Wirtz, D. & Hanes, J. in *Plos One* Vol. 4 e4294 (Public Library of Science, 2009).

19 Cu, Y. & Saltzman, in. *Advanced Drug Delivery Reviews* **61**, 101-114 (Elsevier, 2009).

20 Mura, S. *et al.* in *Biomacromolecules* Vol. 12, 4136-4143 (ACS Publications, 2011).

21 Thornton, D. *et al.* in *Biochem. J.* Vol. 316 967-975 (NCBI, 1996).

22 Harding, S. E. in *Advances in Carbohydrate Chem. and Biochem,* Vol. 47 345-381 (Elsevier, 1989).

23 Carlstedt, I., Lindgren, H., Sheehan, J. K., Ulmsten, U. & Wingerup, L. in *Biochemical Journal* Vol. 211 13-22 (1983).

24 Peppas, N. A. & Huang, Y. in *Advanced Drug Delivery Reviews* Vol. 56 1675-1687 (Elsevier, 2004).

25 Coles, J. M., Chang, D. P. & Zauscher, S. in *Current Opinion in Colloid & Interface Science* Vol. 15 406-416 (Elsevier, 2010).

26 Malmsten, M., Blomberg, E., Claesson, P., Carlstedt, I. & Ljusegren, I. in *Journal of Colloid and Interface Science* in 151 579-590 (Elsevier, 1992).

27 Durrer, C., Irache, J. M., Duchene, D. & Ponchel, G. in *Journal of Colloid and Interface Science* Vol. 170 555-561 (Elsevier, 1995).

28 Perez, E. & Proust, J. E. in *Journal of Colloid and Interface Science* Vol. 118 182-191 (Elsevier, 1987).

29 Bevan, M. A. & Prieve, D. C. in *Langmuir* Vol. 16 9274-9281 (ACS Publications, 2000).

30 Eichmann, S. L. & Bevan, M. A. in *Langmuir Letters* Vol. 26 14409-14413 (ACS Publications, 2010).

31 Everett, W. N., Wu, H.-J., Anekal, S. G., Sue, H.-J. & Bevan, M. A. in *Biophysical Journal* Vol. 92 1005-1013 (Cell Press, 2007).

32 Picot, R., Das, I. & Reid, L. in *Thorax* Vol. 33 235-242 (BMJ Publishing Group Ltd and British Thoracic Society, 1978).

33 Gerken, T. A., Butenhof, K. J. & Shogren, R.in *Biochemistry* Vol. 28 5536-5543 (Amer. Biochemical Society, 1989).

34 Bansil, R., Stanley, E. & Lamont, J. T. Vol. 57 635-657 (Annual Reviews 4139 El Camino Way, PO Box 10139, Palo Alto, CA 94303-0139, USA, 1995).

35 Maheshwari, R. & Dhathathreyan, A. in *Journal of Colloid and Interface Science* Vol. 293 263-269 (Elsevier, 2006).

36 Shi, L. & Caldwell, K. D. in *Journal of Colloid and Interface Science* Vol. 224 372-381 (Elsevier, 2000).

37 Yakubov, G. E., Papagiannopoulos, A., Rat, E. & Waigh, T. A. in *Biomacromolecules* Vol. 8 3791-3799 (ACS Publications, 2007).

38 Lundin, M., Sandberg, T., Caldwell, K. D. & Blomberg, E. in *Journal of Colloid and Interface Science* Vol. 336 30-39 (Elsevier, 2009).

39 Feiler, A. A., Sahlholm, A., Sandberg, T. & Caldwell, K. D. in *Journal of Colloid and Interface Science* Vol. 315 475-481 (Elsevier, 2007).

40 Halthur, T. J., Arnebrant, T., Macakova, L. & Feiler, A. in *Langmuir* Vol. 26 4901-4908 (ACS Publications, 2010).

41 Proust, J. E., Baszkin, A., Perez, E. & Boissonnade, M. M. in *Colloids and Surfaces* Vol. 10 43-52 (Elsevier, 1984).

42 Sandberg, T., Blom, H. & Caldwell, K. D. in *Journal of Biomedical Materials Research* Vol. 91 762-772 (Wiley Online Library, 2009).

43 Button, B. *et al.* in *Science* Vol. 337 937-941 (American Association for the Advancement of Science).

44 Bromberg, L. E. & Barr, D. P. *Biomacromolecules* Vol. 1 325-334 (ACS Publications, 2000).

45 Khan, M. A., Wolf, D. P. & Litt, M. in *Biochimica et Biophysica Acta* Vol. 444 369-373 (Elsevier, 1976).

46 Deacon, M. *et al.* in *Biochemical Journal* Vol. 348 557-563 (Amer. Biochemical Society, 2000).

47 Sriamornsak, P., Wattanakorn, N. & Takeuchi, H. in *Carbohydrate Polymers* Vol. 79 54-59 (Elsevier, 2010).

48 Anitha, A. *et al.* in *Carbohydrate Polymers* Vol. 83 66-73 (Elsevier, 2011).

49 Joergensen, L., Klosgen, B., Simonsen, A. C., Borch, J. & Hagesaether, E. in *international journal of pharmaceutics* Vol. 411 162-168 (Elsevier, 2011).

50 Larhed, A. W., Artursson, P., Gråsjö, J. & Björk, E. *J. Pharm.. Sci.* Vol. 86 660-665 (Wiley Online Library, 1997).

51 Olmsted, S. S. *et al.* in *Biophysical Journal* Vol. 81, 1930-1937 (Elsevier, 2001).

52 Lieleg, O., Vladescu, I. & Ribbeck, K. in *Biophysical Journal* Vol. 98 1782-1789 (Elsevier, 2010).

53 Cao, X. *et al.* in *Biophysical Journal* Vol. 76, 1250-1258 (Elsevier, 1999).

54 Blake, J. in *J. of Biomech.* Vol. 8 179-190 (Elsevier, 1975).

55 Lever, J. D. Vol. 97 131 (Blackwell Publishing, 1963).

56 Hatch, T. F. & Gross, P. (New York London: Academic Press Inc., Berkeley Square House, WI, 1964).

57 Paul, J. F. in *Principles of polymer chemistry*. (Cornell University Press, 1953).

58 Milner, S. T. in *Science* Vol. 251 905-914 (Science, 1991).

59 Milner, S. T. in *Europhysics Letters* Vol. 7 695 (IOP Publishing, 1988).

60 Shim, D. F. K. & Cates, M. E. *J. de Physique* Vol. 51 701-707 (Société française de physique, 1990).

61 Watanabe, H. & Tirrell, M. *Macromolecules* Vol. 26 6455-6466 (ACS Publications, 1993).

62 Vladescu, I., Lieleg, O., Jang, S. & Ribbeck, K. in *Journal of Pharmaceutical Sciences* Vol. 101 436-442 (Wiley Online Library, 2011).

63 Lieleg, O., Lieleg, C., Bloom, J., Buck, C. B. & Ribbeck, K. in *Biomacromolecules* Vol. 13 1724-1732 (ACS Publications, 2012).

64 Kamholz, A. E., Schilling, E. A. & Yager, P. in *Biophys. J.* Vol. 80 1967-1972 (Elsevier, 2001).

65 Waldauer, S. A., Wu, L., Yao, S., Bakajin, O. & Lapidus, L. J. in *Journal of Visualized Experiments* 1-9 (JoVE Corporation, 2012).

66 Nam, J., Lim, H., Kim, D., Jung, H. & Shin, S. in *Lab on a Chip* Vol. 12 1347-1354 (Royal Society of Chemistry, 2012).

67 Reynolds, O. in *Philos. Trans.* Vol. 174, 935-982 (JSTOR, 1883).

68 Reynolds, O. in *Philos. Trans.* Vol. 186, 123-164 (JSTOR, 1895).

69 Squires, T. M. & Quake, S. R. Vol. 77 977 (APS, 2005).

70 Macounova, K., Cabrera, C. R. & Yager, P. in *Anal. Chem.* Vol. 73 1627-1633 (ACS Publications, 2001).

71 Frank, M., Anderson, D., Weeks, E. R. & Morris, J. F. in *Journal of Fluid Mechanics* Vol. 493 363-378 (Cambridge Univ Press, 2003).

72 Eral, H. B., Oh, J. M., Van Den Ende, D., Mugele, F. & Duits, M. H. G. in *Langmuir* Vol. 26 16722-16729 (ACS Publications, 2010).

73 Beard, D. A. in *J. of Applied Phys.* Vol. 89 4667-4669 (AIP, 2001).

74 Hatch, A. *et al.* in *Nature Biotechnology* Vol. 19 461-465 (Nature Publishing Group, 2001).

75 Koo, J. & Kleinstreuer, C. in *J. of Micromech and Microeng.* Vol. 13 568 (IOP Publishing, 2003).

76 Dzyaloshinskii, I. E., Lifshitz, E. M. & Pitaevskii, L. P. in *Adv. Phys.* Vol. 10, 165-209 (1961).

77 Prieve, D. C. & Russel, W. B. in *J. Colloid Interface Sci.* Vol. 125, 1 (Elsevier, 1988).

78 Israelachvili, J. N. in *Intermolecular and Surface Forces*. 2nd edn, (Academic Press, 1992).

79 Bevan, M. A. & Prieve, D. C. in *Langmuir* Vol. 15, 7925-7936 (ACS Publications, 1999).

80 Wu, H.-J., Everett, W. N., Anekal, S. G. & Bevan, M. A. in *Langmuir* Vol. 22 (ACS Publications, 2006).

81 Wu, H. J. & Bevan, M. A. in *Langmuir* Vol. 21 1244-1254 (ACS Publications, 2005).

82 Milner, S. T. in *Europhysics Letters* Vol. 7 695-699 (IOP Science, 1988).

83 Milner, T., Witten, T. A. & Cates, M. E. in *Macromolecules* Vol. 21 2610-2619 (ACS Publications, 1988).

84 Shim, D. F. K. & Cates, M. E. in *J. de Physique* Vol. 51 701- 707 (Société française de physique, 1990).

85 Smith, S. B., Finzi, L. & Bustamante, C. in *Science* Vol. 258 1122-1126 (Science, 1992).

86 Smith, S. B., Finzi, L. & Bustamante, C. in *Science* Vol. 258 1122-1126 (American Association for the Advancement of Science, 1992).

87 Bustamante, C., Marko, J., Siggia, E. & Smith, S. *Science* Vol. 265 1599-1600 (Science, 1994).

88 Fick, A. in *Philosophical Magazine and Journal of Science* Vol. 10 30-39 (Taylor & Francis, 1855).

89 Einstein, A in. *Investigations on the Theory of the Brownian Movement.* (Courier Dover Publications, 1956).

90 Stokes, G. G. in *Transactions of the Cambridge Philosophical Society* Vol. 8 105-165 (1856).

91 Bachelor, G. K. in *Journal of Fluid Mechanics* Vol. 74 1-29 (Cambridge University Press, 1976).

92 Russell, W. B., Saville, S. A. & Schowalter, W. R. in *Colloidal Dispersions*. (Cambridge University Press, 1989).

93 Murphy, T. J. & Aguirre, J. L. in *J. Chem. Phys.* Vol. 57 2098 (AIP, 1972).

94 Beltran-Villegas, D. J., Edwards, T. D. & Bevan, M. A. in *Langmuir* Vol. 29, 12337-12341 (ACS Publications, 2007).

95 Brenner, H. in *Chem. Eng. Sci.* Vol. 16, 242-251 (Elsevier, 1961).

96 Bevan, M. A. & Prieve, D. C. in *J. Chem. Phys.* Vol. 113 1228-1236 (AIP, 2000).

97 Alexander, B. M. & Prieve, D. C. in *Langmuir* Vol. 3 788-795 (ACS Publications, 1987).

98 Prieve, D. C. in *Advances in Colloid and Interface Science* Vol. 82 93-125 (Elsevier, 1999).

99 Van Helden, A. K., Jansen, J. W. & Vrij, A. in *Journal of Colloid and Interface Science* Vol. 81 354-368 (Elsevier, 1981).

100 Sigurdsson, H. H., Kirch, J. & Lehr, C.-M. in *International Journal of Pharmaceutics* Vol. 453, 56-64 (Elsevier, 2013).

101 Dawson, M., Wirtz, D. & Hanes, J. in *Biotech. Prog.* Vol. 278 50393-50401 (AIChE, 2003).

102 Afdhal, N. H. *et al.* in *Biomacromolecules* Vol. 5 269-275 (ACS Publications 2004).

103 Prieve, D. C. in *Adv. Colloid Interface Sci.* Vol. 82 93-125 (Elsevier, 1999).

104 Bike, S. G. in *Current Opinion in Colloid & Interface Science* Vol. 5 144-150 (Elsevier, 2000).

105 Beltran-Villegas, D. J., Sehgal, R. M., Maroudas, D., Ford, D. M. & Bevan, M. A. in *Journal of Chemical Physics* Vol. 135 (AIP, 2011).

106 Eichmann, S. L., Meric, G., Swavola, J. C. & Bevan, M. A. in *Langmuir* Vol. 29, 2299-2310 (ACS, 2013).

107 Goldman, A. J., Cox, R. G. & Brenner, H. in *Chemical Engineering Science* Vol. 21 (Elsevier, 1966).

108 Brenner, H. in *Chemical Engineering Science* Vol. 16 242-251 (Elsevier, 1961).

109 Murphy, T. J. & Aguirre, J. L. in *Journal of Chemical Physics* Vol. 59 (AIP, 1972).

110 van Helden, A. K., Jansen, J. W. & Vrij in *J. Colloid Interface Sci.* Vol. 81 354-368 (Elsevier, 1981).

111 Baker, J. A. & Berg, J. C. in *Langmuir* Vol. 4 1055-1061 (ACS Publications, 1988).

112 Hummer, G. in *New Journal of Physics* Vol. 7 (IOP Science, 2005).

113 Takayama, S. *et al.* in *PNAS* Vol. 96 5545-5548 (National Acad Sciences, 1999).

114 Park, T. H. & Shuler, M. L. in *Biotech. Prog.* Vol. 19 243-253 (Wiley Online Library, 2003).

115 Kenis, P. J. A., Ismagilov, R. F. & Whitesides, G. M. in *Science* Vol. 285 83-85 (American Association for the Advancement of Science, 1999).

116 Kamholz, A. E., Weigl, B. H., Finlayson, B. A. & Yager, P. in *Biophys. J.* Vol. 71 5340-5347 (ACS Publications, 1999).

117 Abecassis, B., Cottin-Bizonne, C., Ybert, C., Ajdari, A. & Bocquet, L. in *Nature* Materials Vol. 7 785-789 (Nature Publishing Group, 2008).

118 Dambrine, J., Géraud, B. & Salmon, J. B. in *New Journal of Physics* Vol. 11 075015 (IOP Publishing, 2009).

119 Toma, A. C., Dootz, R. & Pfohl, T. in *J. Phys. D: Appl. Phys.* Vol. 46 114001 (IOP Publishing, 2013).

120 Nam, J., Lim, H., Kim, D., Jung, H. & Shin, S. Vol. 12 1347-1354 in *Lab on a Chip* (Royal Society of Chemistry, 2012).

121 Larsen, M. U. & Shapley, N. C. in *Analytical Chemistry* Vol. 79 1947-1953 (ACS Publications, 2007).

122 Shogren, R., Gerken, T. A. & Jentoft, N. in *Biochemistry* Vol. 28 5525-5536 (ACS Publications, 1989).

123 Bansil, R., Stanley, E. & LaMont, J. T. in *Annual Review of Physiology* Vol. 57 635-657 (Annual Reviews, 1995).

124 Dickey, B.F. in *Science* Vol. 924 337 (American Association for the Advancement of Science, 2012)

9. CURRICULUM VITAE

EDUCATION

- **Doctorate of Philosophy, Chemical and Biomolecular Engineering,** Johns Hopkins University, September 2014
  -Extracurricular activities: President of Graduate Student Liaison Committee, Head Coach of rugby team
  -Publications: Two publications in notable journals, two in press
  -Fellowship: Institute for NanoBio Technology
- **Bachelor of Science, Physics,** James Madison University, 2008
  -Second major in Spanish; Minor in Mathematics
  -Honors: Cum Laude; Honors College; President's List; ΣΠΣ (physics honor society); ΠΜΕ (math honor society)
  -Extracurricular activities: Vice President of JMU's Women's Rugby Team

---

TEACHING EXPERIENCE

- **Graduate Student**, Johns Hopkins University, 2009 – 2014
  -Trained and mentored 5 undergraduate students in Chemical Engineering laboratory research.
  -Trained junior graduate students in colloidal science and laboratory techniques.
- **Head Coach**, Johns Hopkins Women's Rugby, 2012 - 2014
  -Recruited, trained, coached, and mentored 30 female collegiate athletes; managed 3 assistant coaches.
  -Worked with the university to find field space and funding and taught the athletes to effectively build and manage a successful sports team.
  -Instilled in each young woman a more positive self-image, a healthy relationship with her body, and the confidence stemming from being a part of a supportive, positive team.
- **Graduate Teaching Assistant**, Johns Hopkins University, 2009 – 2010
  -Trained 10 graduate students in sterile cell culture technique and in planning and carrying out experiments.
  -Taught 8 students to synthesize and characterize gold nanoparticles.
- **Assistant Teacher**, Woodland Montessori Nursery School, 2007 – 2008
  -Supervised 20 children and helped implement Spanish lesson plans.
- **Instructor**, Keister Elementary School, Fall 2008
  -Taught young children of immigrants to read and developed strategies for practicing in the home where their parents were unable to help them with English reading material.
  -Worked with students individually or in groups of two to three.
- **Instructor**, Amistad at Thomas Wood Middle School, Fall 2008
  -Provided academic and social mentoring to Hispanic children in after-school program, worked with 25 children.
- **Tutor**, James Madison University, 2006 - 2007

-Developed and delivered lesson plans to college students as a private tutor in Spanish, Physics, and Calculus.
-Managed 5 client relationships.

LEADERSHIP EXPERIENCE

- **President**, Graduate Student Liaison Committee, Johns Hopkins University, 2012-2013
  -Managed student government for Chemical Engineering department, planned and carried out departmental events, allocated student government monetary resources.
  -Coordinated recruiting events and helped new students adjust to graduate school.
  -Coordinated with other departments for interdepartmental social events and fundraiser.
- **Vice President**, James Madison University Women's Rugby**,** 2012 - 2014
  -Recruited, planned fundraisers, planned team bonding events, coordinated with team executive board.
- **Coordinator**, Bethesda Project Homeless Shelter, 2002 – 2003
  -Formed and managed group that provided weekly dinners for 60 men in a Philadelphia homeless shelter.
  -Found funding, food donations, volunteers, and adviser. Prepared meals and coordinated transportation of food and volunteers to homeless shelter.
  -Served food, ate with the homeless men, and socialized to bring happiness to their evenings once a week.

ADDITIONAL ACTIVITIES

- Volunteer at Lazarus House AIDS Hospice; Costa Rica Red Cross operational support; Willow Grove Emergency Response team; lifeguard, swim instructor; JMU snowboard racing team; USA developmental 7's rugby team; avid traveler; play the cello